NuTTS'98

Numerical Towing Tank Symposium

21-23 September 1998, Hamburg, Germany

Sponsored by the ONRIFO-EUR

An unsteady model for free surface flows around hydrofoils

V. Bertram
TU Hamburg-Harburg, Germany

M. Landrini *C. Lugni*
INSEAN, Italian ship model basin, Roma – Italy.

1 Introduction

Foils are employed in ships as control devices for motions and as main sustaining system of the entire vessel. In both cases, ambient waves, vehicle's motions and, generally speaking, out–of–design conditions render the flow unsteady. Further, as a result of small submergences or large amplitude motions, the flowfield about hydrofoils is significantly affected by the air–water interface.

We present a model for the unsteady flow generated by a hydrofoil in arbitrary motion beneath a wavy free surface. If large separation phenomena are ruled out, the flowfield can be accurately described in terms of inviscid–rotational fluid mechanics in which a thin vortical layer mimics the hydrofoil's wake and a suitable unsteady Kutta condition provides the mechanism for vorticity generation. On this physical ground, the initial value problem is recast in term of boundary integral equations for the velocity field coupled to evolution equations for the free surface and the wake.

The properties of the developed algorithm are discussed by comparing present results againts those obtained by different numerical techniques. In particular, previous existing approaches based on BEM are almost exclusively 'steady' models, while grid–based solvers are both (fictitiously) steady and unsteady. In the latter category, either Euler or Navier–Stokes equations have been solved. We have chosen the classical Duncan's experiment as a benchmark and, once steady regime is reached, we compare the present wave profiles with results from Bertram et al. (1998) and Thiart & Bertram (1998). In the following, only the unsteady inviscid–rotational model is described, while full details about the other two models can be found in the referenced literature.

2 Mathematical statement of the problem

The unsteady flow about a hydrofoil $\mathcal{H}$ beneath a free surface $\mathcal{F}$ is considered. The main motion of the hydrofoil is translatory but arbitrary oscillations in heave, surge and pitch are allowed for. If a wave train exists at $x = -\infty$, the problem can be re–formulated as described in Landrini et al. (1998). The full description of general case is here omitted for the sake of brevity.

An unsteady problem for the Euler equations can be written and a possible approach consists in splitting it into a kinematic problem and a dynamic one. The velocity field $\boldsymbol{u}$ satisfies the purely kinematic problem

$$\nabla \cdot \boldsymbol{u} = 0 \qquad \nabla \times \boldsymbol{u} = \gamma_{\mathcal{W}} \tag{1}$$

in which $\gamma_{\mathcal{W}}$ is the generalized vorticity distribution. As a second step, the evolution of the free surface and of the wake is stepped forward by integrating suitable kinematic and dynamic equations.

In the present approach the integral representation

$$\begin{aligned} \boldsymbol{u}(\hat{\boldsymbol{P}}) &= \nabla_{\hat{P}} \int_{\mathcal{F}} \boldsymbol{u} \cdot \boldsymbol{n} G dS_P + \nabla_{\hat{P}} \times \int_{\mathcal{F}} \boldsymbol{u} \times \boldsymbol{n} G dS_P \\ &+ \nabla_{\hat{P}} \int_{\mathcal{H}} \sigma G dS_P + \frac{\Gamma}{\mathcal{L}} \nabla_{\hat{P}} \times \int_{\mathcal{H}} \boldsymbol{k} G dS_P + \nabla_{\hat{P}} \times \int_{\mathcal{W}} \gamma_{\mathcal{W}} G dS_P \end{aligned} \tag{2}$$

is introduced, in which

$$\sigma = [\boldsymbol{u} - \boldsymbol{v}] \cdot \boldsymbol{n} \qquad \frac{\Gamma}{\mathcal{L}} \boldsymbol{k} = -[\boldsymbol{u} - \boldsymbol{v}] \times \boldsymbol{n} \qquad \Gamma = \int_{\mathcal{H}} \boldsymbol{u} \cdot \boldsymbol{\tau} d\ell \tag{3}$$

$\boldsymbol{v}$ is the velocity of a point of the hydrofoil, G is the two dimensional free–space Green function and Γ is the circulation about the hydrofoil. The resulting boundary integral equations can be solved by coupling an iterative solver with a fast summation techniques which allow for obtaining an operation count of order $N \log N$ (Graziani & Landrini 1998).

Once the velocity field is known, free surface and wake equations can be integrated in time, thus providing the new set of boundary data for the next time–step. On the body the standard impermeability constraint is applied.

Free surface evolution equations The free surface equations follows from the kinematic condition that the fluid does not cross it and the dynamic constraint that the pressure there is atmospheric. These requirements are fulfilled if the motion of the free surface points $\boldsymbol{P}$ are described through

$$\frac{D_{\mathcal{F}}\boldsymbol{P}}{D\,t} = \boldsymbol{w} = u_\nu \boldsymbol{\nu} + w_\tau \boldsymbol{\tau} \qquad \frac{D_{\mathcal{F}}\,u_\tau}{D\,t} = \boldsymbol{\tau}\cdot\left\{(\boldsymbol{w}-\boldsymbol{u})\cdot\nabla\boldsymbol{u} + \boldsymbol{g} - \frac{1}{\rho}\nabla p_a\right\} + \boldsymbol{u}\cdot\frac{D_{\mathcal{F}}\,\boldsymbol{\tau}}{D\,t} \tag{4}$$

In these equations $\boldsymbol{\nu}$, $\boldsymbol{\tau}$ are the unit normal and tangent vectors to $\mathcal{F}$ and $\frac{D_{\mathcal{F}}}{D\,t} = \frac{\partial}{\partial t} + \boldsymbol{w}\cdot\nabla$ is the derivative following the motion of a point $\boldsymbol{P}$ belonging to the free surface $\mathcal{F}$. The first equation states that the point $\boldsymbol{P}$ move with a velocity $\boldsymbol{w}$: the normal component $\boldsymbol{w}\cdot\boldsymbol{\nu}$ is fixed by the corresponding component $u_\nu = \boldsymbol{u}\cdot\boldsymbol{\nu}$ of the fluid below, while the tangential one, w_τ, can be arbitraryly chosen. Finally, regardless of the actual value of w_τ, the tangential velocity component u_τ of the fluid evolves according to the second equation, which follows by the tangential projection of the Euler equation.

Wake evolution equations The vorticity is assumed confined in a narrow wake $\mathcal{W}$ downstream of the hydrofoil and, indeed, modeled by means of a zero thickness vortex layer of local strength

$$\gamma_{\mathcal{W}} = \gamma_{\mathcal{W}}\boldsymbol{k} = (\boldsymbol{u}_+ - \boldsymbol{u}_-)\times\boldsymbol{\nu} = [u_\tau]\boldsymbol{k}\,,$$

where $[u_\tau] \equiv [u_\tau]$ is the tangential velocity jump across the vortex sheet itself. The wake pointwise (Lagrangian) behaviour is fully described by the nonlinear differential system of equations

$$\frac{D_{\mathcal{W}}\,\boldsymbol{P}(\xi,t)}{D\,t} = \boldsymbol{w}(\xi,t) \qquad \frac{D_{\mathcal{W}}\,J\gamma_{\mathcal{W}}}{D\,t} = 0 \tag{5}$$

which account for the kinematics and the dynamics of the wake, respectively. In the first equation $\boldsymbol{P}(\xi,t)$ is the position of a wake point, characterized by the material coordinate ξ, which moves with a velocity defined as $\boldsymbol{w}(\xi,t) = \frac{1}{2}(\boldsymbol{u}_+ + \boldsymbol{u}_-)$, and $\frac{D_{\mathcal{W}}=}{D\,t}\frac{\partial}{\partial t} + \boldsymbol{w}\cdot\nabla$ is derivative following $\boldsymbol{P}\in\mathcal{W}$. The second equation, where $J(\xi,t) = \left|\frac{\partial\boldsymbol{P}}{\partial\xi}\right|$, allows for the time evolution of the concentrated vorticity $\gamma_{\mathcal{W}}(\xi,t)$. The initial value problem for the set of equations (5) is defined by the condition that the wake is continously shed from the trailing edge whith a vorticity density γ_{TE} to be determined according to the assumption of zero trailing edge loading.

3 Discussion

We consider the flow generated by a hydrofoil starting from rest. Eventually steady state is reached and the numerically predicted wave pattern can be compared with data measured by Duncan (Duncan, 1983). There a NACA0012 profile with chord length c at an angle of attack $\alpha = 5°$ was placed below the free surface. The depth of submergence D is measured from the mid–chord profile to the undisturbed water level $\eta = 0$ and cases $D/c = 1.2857$, 1.1626 and 1.0345 are discussed in the following. The shallower submergences lead to the formation of a steady breaking wave past the hydrofoil and are not discussed here.

For all the computational methods considered, tests are performed to check the invariance with respect to further refinements of the discrete solution. In particular, for the present method, convergence is checked by halving the time–step Δt and doubling the number of free surface points until convergence is reached. A typical run requires $N_{fs} = 512 - -2048$, $N_b = 60 - -120$, $\Delta t = \frac{1}{50}c/U$. Damping layers are placed at the edges of the computational domain to prevent unphysical reflections and the comparison of solutions obtained by doubling the length L of the discretized free surface rules out possible end effects.

In the RANSE code, the part of the geometry which embeds the free surface was systematically refined using three different Finite-Volume grids, the numerical grid around the hydrofoil was kept unchanged. The numerical tests showed that the grid refinement around the profile is not so important for the formation of the free surface as around the free surface itself where numerical diffusion could quickly damp the generated waves.

In figure 1 the present unsteady solution, solid lines, is compared with Duncan's experiments, $\circ$, for decreasing values D/c. To rule out the uncertainty due to the graphic manipulation, the Lagrangian free surface markers are simply connected with straight segments For all the cases shown, quite reasonable wave patterns can be observed. For the deepest submergence (upper plot) only the present solution is contrasted with the Duncan data: the first hollow just above the profile is well predicted as well as the to following peaks.

For $D/c = 1.1626$ differences appear. In particular, the trough induced above the suction side is underpredicted by all the methods. Steady BEM, $\diamond$, and RANSE, $\bullet$, solutions roughly give the same values while a deeper depression is predicted by the unsteady solver which is placed half–way from the actual data. This feature is repeated for the throughs more downstream. The two inviscid rotational models capture the first and second experimental wave humps well, while the third crest is rather underestimated. Also a sort of 'shift' of the wave forms can be detected which may require an analysis of the discrete dispersion relation. As the RANSE code prediction is concerned, wave height is significantly underpredicted although the wavelength is

correctly captured. The reasons for this disagreement has to be investigated, but recent results of Tzabiras (1997) indicate that the assumption of turbulent flow over the whole foil may be one contributing factor.

This behaviour is, in some sense, magnified, for the shallowest submergence (bottom plot). In particular the free surface deformation above the hydrofoil is by far more pronounced in the experiments. Actually, following the Duncan suggestion, in the present unsteady computations the bottom of the basin is not taken into account because of the deep water regime of the generated waves. In spite of this, the 'ground–effect' on the hydrofoil should increase the actual circulation about it which may explain the reduced depression predicted. But, although RANSE computation takes the bottom effect, the same disagreement is observed.

The last point to mention is the experimental uncertainty. No error bars are reported in Duncan's papers and he generally claimed 'distances were measured to an accuracy of about ±0.3 cm', which can explain the differences between the experiments and the reported numerical results only partly.

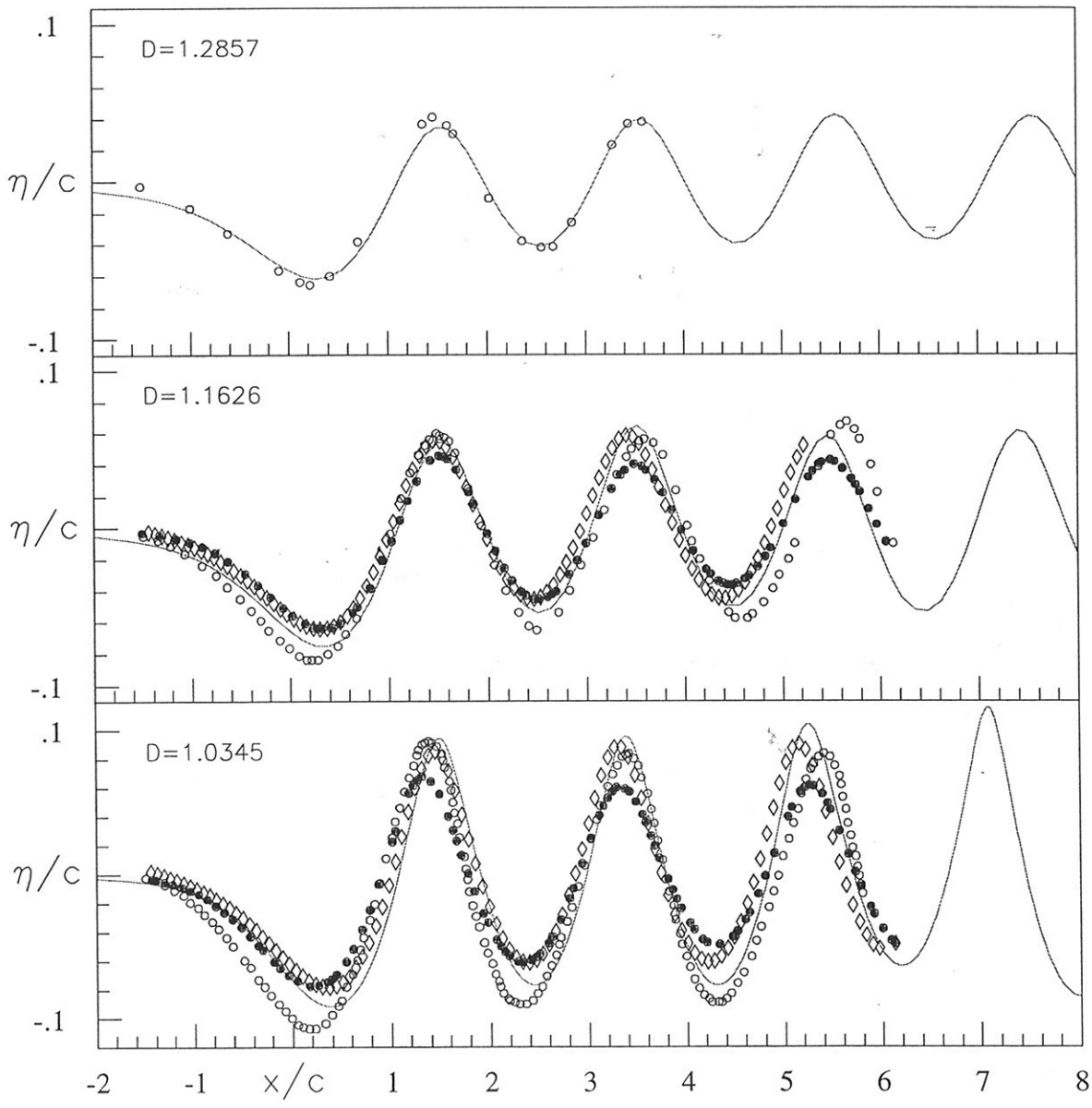

Figure 1: Wave height η/c past a NACA 0012 ($F_n = U/\sqrt{gc}$ =0.567). The mid–chord point is located at $(x = 0., y = -D/c)$ and the incidence is 5 degrees. Solid lines: present unsteady results, ∘ measurements, • FVM, ⋄ Steady BEM.

As a simple example of more general unsteady flows, a case is considered in which the same hydrofoil is forced to oscillate in pitch about the trailing edge. The mean submergence is $D/c = 1.2857$, the amplitude of the sinusoidal oscillations is 5 degrees and two values of the period T have been considered. The resulting wave

patterns for the corresponding reduced frequencies $\tau = 2\pi U/gT = 2.$ ($\tau = 1.$) are reported in the top (bottom) plots of figure 2. Clearly, a lee wave system due to the mean forward motion is expected and can be actually detected just downstream the foil for $0 \leq x/c \leq 4.5$. The mean amplitude is smaller than the corresponding one in the top plot of figure 1 because of the zero mean angle of attack and, most important, in both cases it is not uniform because of the waves radiated downstream ($\tau > 0.25$) as well as because of the local displacement due to the body motion. Past the tail of the lee wave, the genuine oscillatory part of the solution can be clearly seen. In both cases, only the longer wavelengths ($\lambda/c \simeq 2$ for $\tau = 2$ and $\lambda/c \simeq 5$ for $\tau = 1$) are well resolved while the shorter ones are too small for being graphically detected.

An extended set of results will be discussed at the symposium.

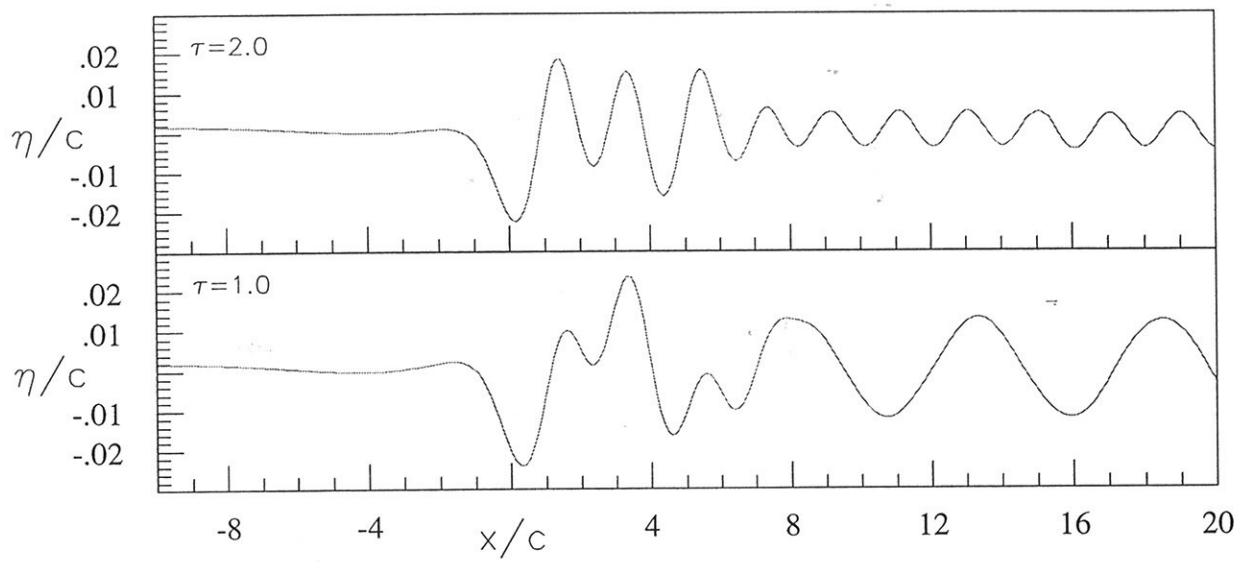

Figure 2: Wave height η/c past a NACA 0012 ($F_n = U/\sqrt{gc}$ =0.567, $D/c = 1.2857$) in pitching motion about the trailing edge. The oscillation amplitude is 5 degrees. The oscillation periods are $TU/c = 0.996$ (top plot) and $TU/c = 2.12$.

BERTRAM, V., MUZAFERIJA, S.; PERIĆ, THIART, G. (1998), *A comparison of free surface viscous and inviscid methods to compute the flow about a submerged hydrofoil.* SACAM '98, Capetown.

DUNCAN, J.H. (1983), *The breaking and non-breaking wave resistance of a two-dimensional hydrofoil*, J. Fluid Mech., Vol. 126, pp. 507-520

GRAZIANI, G., RANUCCI, M., CASCIOLA,C.M. AND GRAZIANI, G. *Viscous effects in wave–body interaction* . Int. J. Off. and Polar Eng., March 1998.

GRAZIANI, G., LANDRINI, M. (1998). *Application of multipoles expansion technique to two–dimensional nonlinear free surface flows*, submitted to J. of Ship Res.

MUZAFERIJA, S.; PERIĆ (1997), *Interface-tracking and interface-capturing methods for viscous free-surface flows*, 5th Symp. on Nonlinear and Free-Surface Flows, Hiroshima

THIART, G.; BERTRAM, V. (1998), *Staggered-grid panel method for hydrofoils with fully nonlinear free-surface effect*, submitted to International Shipbuilding Progress.

TZABIRAS, G.D. (1997), *A numerical investigation of 2d, steady free surface flows*, Int. J. Num. Methods in Fluids 25, pp. 567-598

Influence of the Kutta condition on 3-d Ship Seakeeping Computations

Volker Bertram (TU Hamburg-Harburg)

Gerhard Thiart (Univ. Stellenbosch)

We present an indirect 3-d Rankine singularity method (RSM) in the frequency domain which captures all forward-speed effects. As both steady and unsteady flow contributions are captured three-dimensionally, the method is called 'fully 3-d'. The method is described in detail in Bertram (1998).

We consider a ship moving with mean speed U in a harmonic wave of small amplitude h. We assume an ideal fluid, using a perturbation formulation for the potential:

$$\phi^t = \phi^{(0)} + \phi^{(1)} + h.o.t. \tag{1}$$

$\phi^{(0)}$ is the part of the potential which is independent of the wave amplitude h. It is the solution of the steady wave-resistance problem. $\phi^{(1)} = Re(\hat{\phi}^{(1)} e^{i\omega_e t}$ is proportional to h. ω_e is the encounter frequency. Quantities with a hat denote a complex amplitude.

All motions u_i $(i = 1...6)$ are assumed to be small of order $O(h)$ where h is the wave amplitude.

The harmonic potential $\phi^{(1)}$ is divided into the potential of the incident wave ϕ^w, the diffraction potential ϕ^d, and 6 radiation potentials, where ϕ^w and ϕ^d are divided into symmetric and antisymmetric contributions:

$$\phi^{(1)} = \phi^{d,s} + \phi^{d,a} + \phi^{w,s} + \phi^{w,a} + \sum_{i=1}^{6} \phi^i u_i \tag{2}$$

The steady flow contributions are determined in a 'fully nonlinear' wave-resistance code employing higher-order panels. This yields the steady dynamic trim and sinkage, the steady wave elevation and the first and second derivatives of $\phi^{(0)}$. The seakeeping (time-harmonic) problem to determine the $\phi^{(1)}$ is linearized around the steady solution, including fulfilling the boundary conditions on the steady (wavy) surface, using the actually wetted surface of the ship with trim and the steady wave profile.

The Kutta condition requires that at the trailing edge the pressures are equal on both sides. The Kutta condition is usually omitted in 3-d methods. It is unclear if this is due to some physical insight about the negligible effects or oversight. Our formulation for the Kutta condition requires zero complex amplitudes for the antisymmetric pressure:

$$-\rho(i\omega_e \hat{\phi}^{i,a} + \nabla\phi^{(0)} \nabla\hat{\phi}^{i,a}) = 0 \tag{3}$$

$i = 2, 4, 6$ for the antisymmetric radiation modes and $i = d$ for the antisymmetric diffraction part.

The unknown diffraction and unit motion radiation potentials can be determined independently. Rankine elements are located on the hull and above the free surface (desingularized). Collocation points are located only on starboard. Mirror images of all Rankine elements account for the port side.

For the diffraction problem, all motions u_i are set to zero. For a radiation problem, the relevant motion amplitude is set to 1 and all other motion amplitudes, the diffraction and incident wave potentials to zero. Then the free-surface condition and the hull condition are fulfilled in a collocation scheme. For the antisymmetric problems, also the Kutta condition is fulfilled at

the last column of collocation points at the ship stern. A corresponding number of Thiart elements (semi-infinite dipole strips on the plane $y = 0$), Bertram and Thiart (1998), are used. The dipole strips start amidships and have the same height as the corresponding last panel on the stern. Radiation and open-boundary condition (waves propagate only downstream and are not reflected at the outer boundary of the computational domain) are enforced by 'staggering' the Rankine sources for the free surface relative to the collocation points by one typical grid spacing downstream. The collocation scheme forms eight systems of linear equations in the unknown element strengths. The four symmetrical (likewise the four antisymmetrical) systems of equations share the same coefficient matrix with only the r.h.s. being different. All four cases are solved simultaneously using Gauss elimination. After solving the systems of equations, only the motions u_i remain to be determined.

The expressions to determine the motions are derived in principle from 'force = mass · acceleration'. This yields a system of linear equations for u_i $(i = 1, ..., 6)$ which is quickly solved by Gauss elimination.

The S-175 containership was computed for the design condition with $F_n = 0.275$. The hull was discretized by 631 elements. Grids on the free surface had then in each case about 1300 elements.

Figs.1 and 2 compare results for oblique waves to experiments for $\mu = 150°$ and $\mu = 120°$. Results for heave and pitch agree well with experiments. The Kutta condition has only significant effects for yaw and sway at low frequencies and for roll near resonance. Here the Kutta condition simulates to some extent the effect of viscous damping and reduces drastically (by factors between 2 and 4) the motions. However, additional viscous effects (those that would be apparent also at zero speed) reduce for roll in reality the motions even more. For yaw and sway, no experimental data are available, but we expect that autopilots in experiments will prevent the large predicted motion amplitudes of the computations.

For low angles of encounter, the Kutta condition failed to improve consistently results. Improvements here are subject to further research.

BERTRAM, V. (1998), *Numerical investigation of steady flow effects in 3-d seakeeping computations*, 22. Symp. Naval Hydrodynamics, Washington

BERTRAM, V.; THIART, G. (1998), *A Kutta condition fo ship seakeeping computations with a Rankine panel method*, Ship Techn. Res. 45, pp.54-63

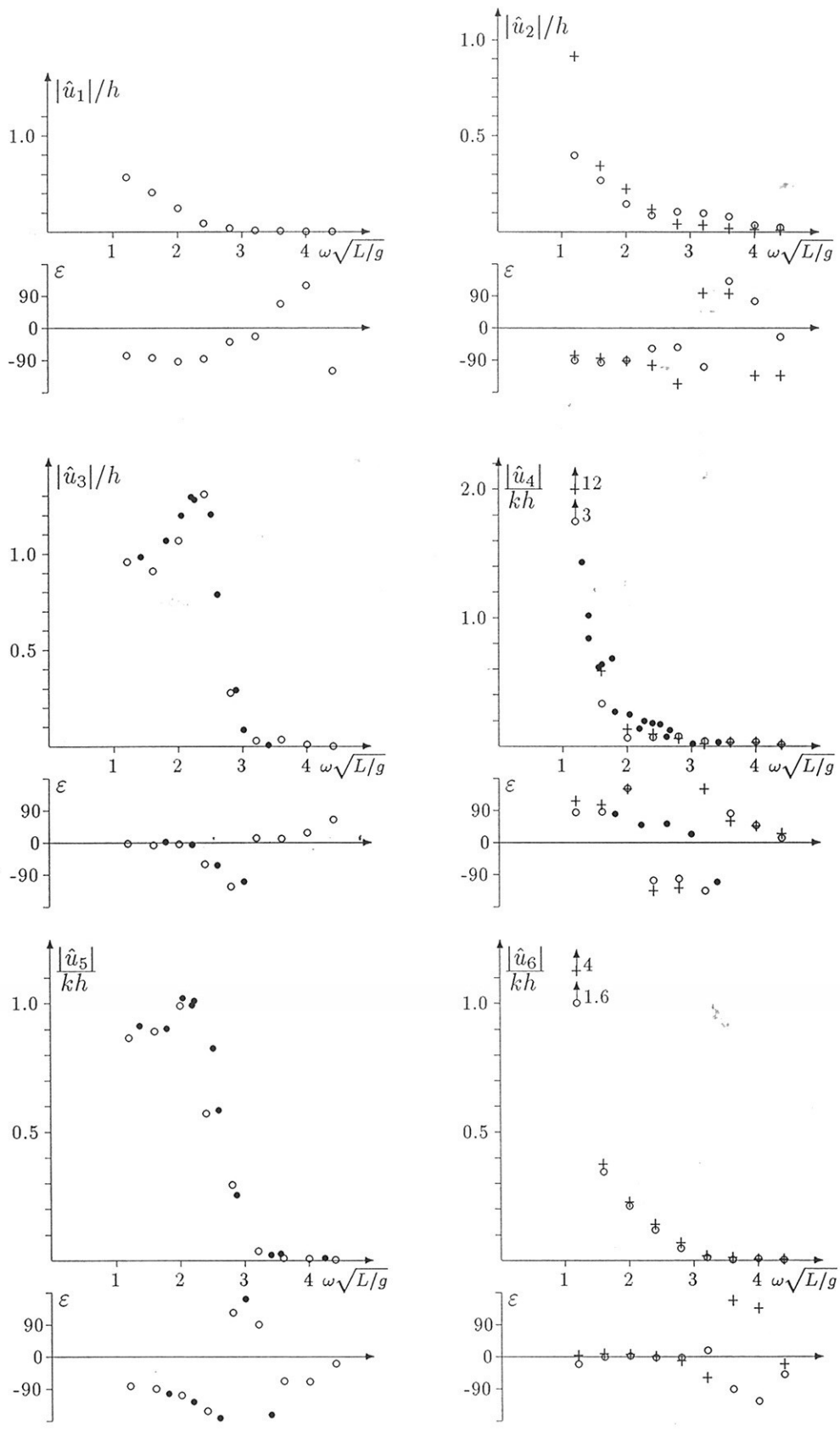

Fig.1: RAOs for S-175, $\mu = 150°$, $F_n = 0.275$; • experiment, + RPM without Kutta condition, ○ RPM with Kutta condition

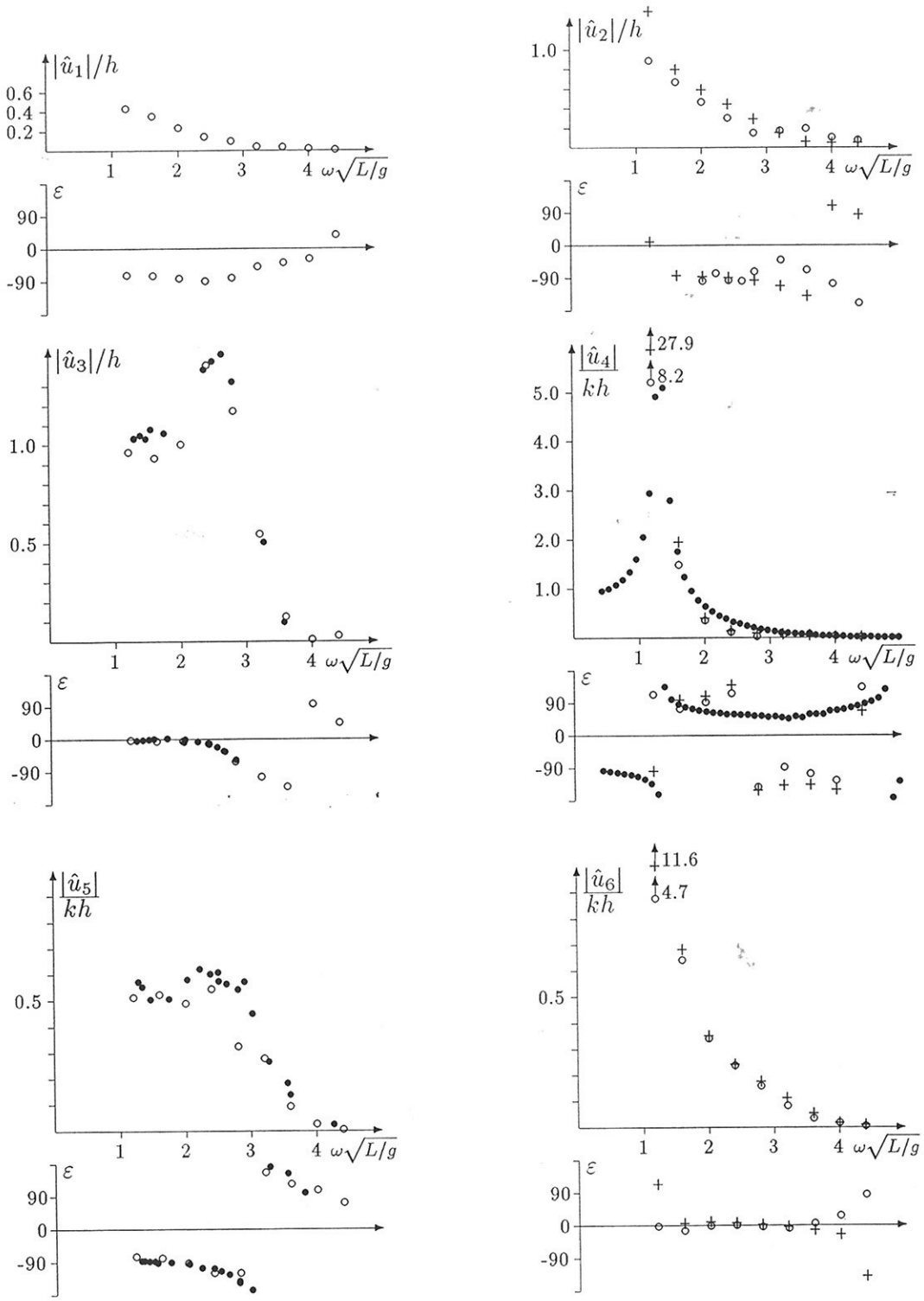

Fig.2: RAOs for S-175, $\mu = 120°$, $F_n = 0.275$; • experiment, + RSM w/o Kutta, ∘ RSM with Kutta

Time domain analysis of ship motions by a Rankine panel method

A. Colagrossi *M. Greco*
INSEAN, Italian ship model basin, Roma – Italy.

Seakeeping analysis in frequency domain by 3D Rankine panel codes are continously improved and presently available results (see e.g. Bertram 1998) are closer and closer to the limits of the underlying theory (small time–harmonic perturbations of the steady base–flow).

Physical insight and finer experimental reference data are necessary as a guidance for further enhancements of codes which in the future will include nonlinear inviscid effects and, eventually, viscous effects. In both cases a time domain approach to the problem is required and here we present some linear computations aimed to develop the basic tools for future steps in time-domain analysis.

We are trying to take advantage from the theory of dynamical systems. By analysing the response of a fluid dynamic system excited by a suitable input some general properties of the system itself can be evaluated even if the phenomenon is nonlinear. In the linear framework, the Fourier analysis of the ship response to transient captive forced motions leads to the classical added and damping coefficients in a broad frequency range. The advantage in performing a transient test is a shorter simulation time with respect to the one required for a set of (time domain) harmonic forced test. Additionally, we experienced reduced difficulties in damping the signals outgoing the truncated physical domain. In the following some linear results for a Wigley hull are obtained by a numerical transient test technique and frequency domain results are recovered together with experimental confirmation. The interaction of an advancing ship with a wave–packet for evaluating the exciting forces and/or the response amplitude operator is under development and will be presented at the Symposium.

Basic formulation

The ship motion problem is formulated in Newman (1978) and only a few details are here recalled. It is assumed that the unsteady disturbance are small with respect to the flowfield generated by the steady forward motion of the ship. Therefore, the velocity potential can be written as $\Phi_T = -U_0\, x + \Phi_0(x,y,z) + \varphi(x,y,z,t)$ where the first two terms are the potential due to the steady flowfield around the vessel advancing with velocity U_0 and the perturbation $\varphi(x,y,z,t)$ contains all the unsteady effects. In the linear framework, the perturbation potential can be further split in a set of potentials proportional to the instantaneous value of the corresponding degree of freedom (three translations and three rotations). Each of the potentials satisfies the Laplace equation, the free surface and the body boundary conditions as well as an appropriate asymptotic behaviour.

In principle the unsteady problems are coupled to the steady flowfield through the velocity and the wave height which, in turn, is the solution of a nonlinear problem. Bertram (1998) solved the general linearized problem in frequency domain but most of the authors further simplify the problem by using the unperturbed free stream, or the double body flow as a basis flow.

Here we solve the problem in time domain by using either the free stream or the double body flow as a basis flow. The initial boundary value problem is recast in the form of integral equation. Namely the perturbation potentials are represented by Rankine sources distributed on the free surface and on the hull. At each time step, the potential on the free surface and the normal derivative on the ship are prescribed and a set of integral equations can be written for the unknown source strenght.

Once this is evaluated by a low order panel method, the wave elevation and the potential on the free surface are stepped forward in time by a second order Runge–Kutta scheme which provides a new

set of boundary data. Clearly, the computational domain is of finite extent and for avoinding spurious reflections damping layers are added along the edges of the discretized free surface.

An auxiliary boundary integral problem for the time derivative of the potential is also solved at each time step. This is used i) for evaluating the tangential derivative of the wave height which is expressed in terms of derivatives of φ and of $\dot{\varphi}$ and ii) for computing the pressure on the hull by the Bernoulli equation. The force acting on the hull is finally computed by direct pressure integration.

Some preliminary results

As a simple and well assessed test case we have considered a Wigley hull which is forced to move in the prescribed degree of freedom with a given time–law. Two different inputs have been adopted and they are shown in figure 1 with the corresponding loading response for the case of forced heave motion. In the top plot, the vertical velocity of the hull follows a single–pulse law. At the beginning the corresponding hydrodynamic force is dominated by the inertia of the fluid with a minor role of the free surface. After the vertical velocity becomes zero, the oscillatory behaviour related to the wave–motion clearly appears. Actually a single–pulse input corresponds to a finite change of the draft. A zero mean input for the draft is obtained by the double pulse shown in the lower plot of figure 1. Also in this case the hydrodynamic force follows the body acceleration at the beginning and eventually exhibits a wavy nature but now with a smaller amplitude. Regardless the actual form of the adopted forcing functions, the Fourier transform of the generalized hydrodynamic force $\boldsymbol{F}(i\omega)$ is related to the Fourier transform of the generalized motions $\boldsymbol{q}(i\omega)$ through $\boldsymbol{F}(i\omega) = [\, \omega^2 \boldsymbol{a}^*(\omega) - i\,\omega\, \boldsymbol{b}^*(\omega) - \boldsymbol{c}\,]\, \boldsymbol{q}(i\omega)$ which is used to determine the added and damping coefficients once the restoring terms $\boldsymbol{c}$ have been evaluated. For the considered heave test the coefficients obtained by adopting the two different forcings are shown in figure 2. The results for the single pulse input (solid lines) closely reproduce the double pulse input results (dashed lines). Differences appear for smaller frequencies, may be due to different energy leakages both in the numerical simulation and in the Fourier treatment of the results.

The present results are compared to frequency domain computations and to experimental data in the next figure 3 (heave:top plot, pitch: bottom plot). Both the time domain results and the frequency ones are obtained by using the uniform stream as a basis flow: an approximation which is still good for the relatively simple hull considered, at least for the heave motion. The time domain analysis reproduce the frequency domain results and both agree satisfactorily with the heave experimental results. Results for pitch motion are less good, in particular the damping is underestimated.

The same kind of agreement between time and frequency computations are obtained for the S175 hull (figure 4). In this case experimental data are available only for the response amplitude operator. This in turn requires the numerical evaluation of the exciting force which will be discussed at the Symposium.

V. Bertram (1998). Numerical investigation of steady flow effects in 3D seakeeping computations. 22^{nd} Symp. on Naval Hydrodynamics. Washington.

J.M.J. Journée (1992). *Experiments and Calculations on Four Wigley Hullforms.* Report No. 909, Ship Hydromechanics Laboratory, Delft University of Technology, Delft, The Netherlands.

J. N. Newman, 1978. *The Theory of Ship Motions*, Advances In Applied Mechanics, 18.

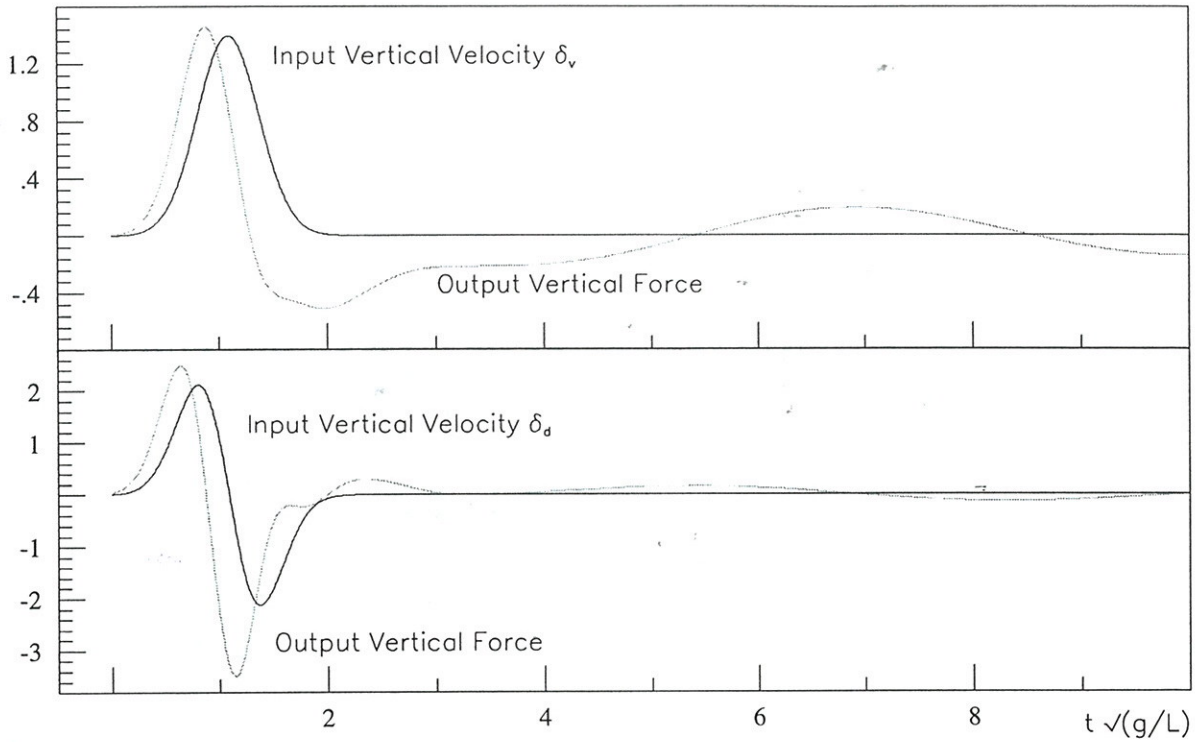

Figure 1: Transient heave-test of a Wigley hull ($F_n = 0.3$). Time histories of input vertical velocity and response vertical force. Top plot: single pulse input. Bottom plot: double pulse input.

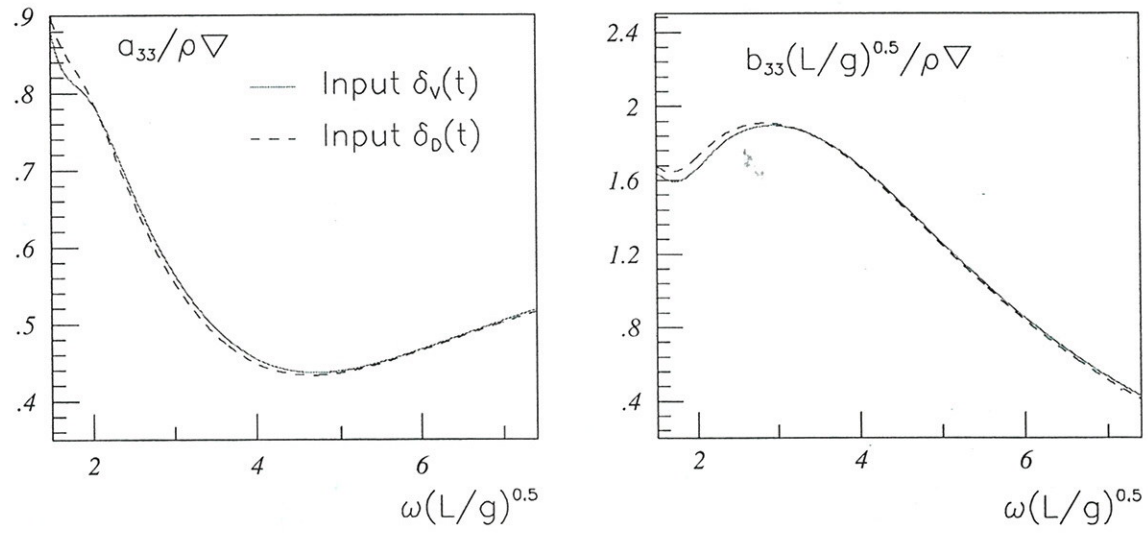

Figure 2: Transient heave-test of a Wigley hull ($F_n = 0.3$). Added mass (left plot) and damping (right plot) coefficients obtained by Fourier analysing the response vertical force (cfr. fig. 1). Solid lines: single pulse input δ_v. Dashed lines: double pulse input δ_d.

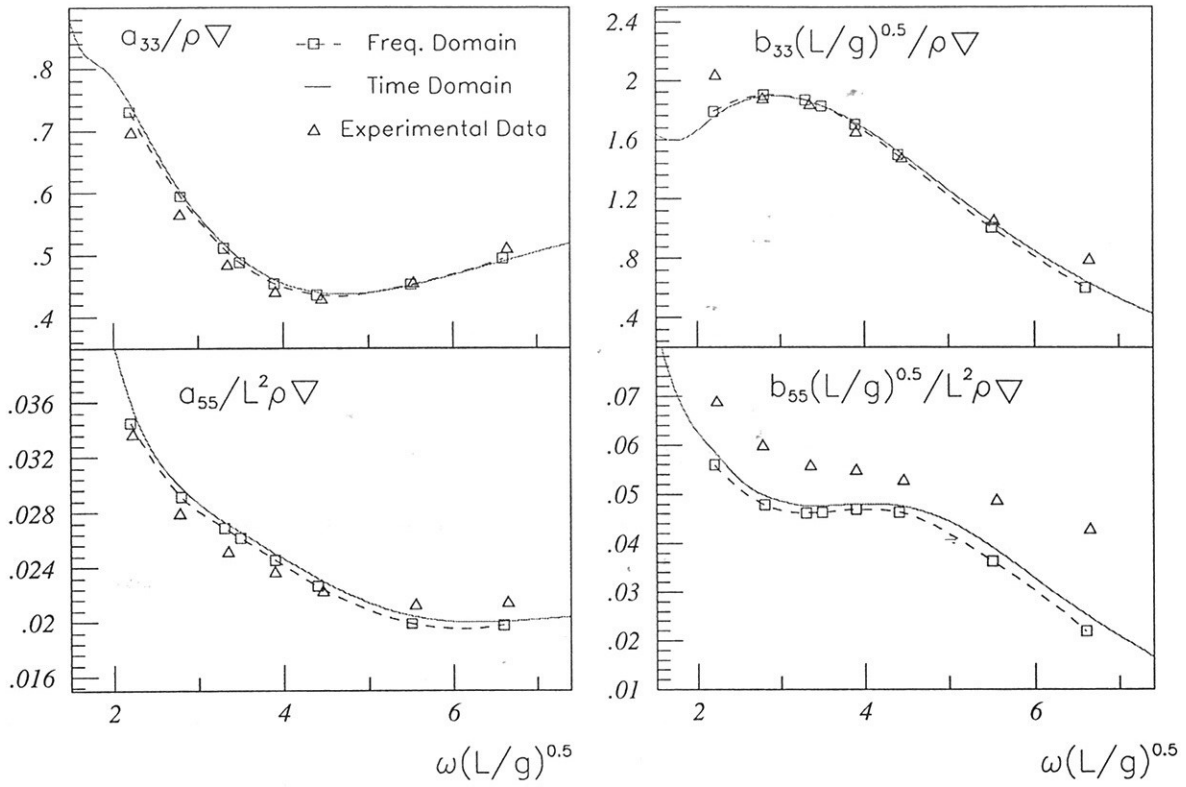

Figure 3: Added mass (left plot) and damping (right plot) coefficients for a Wigley hull ($F_n = 0.3$). Frequency domain, □, and time domain (solid lines) numerical results are contrasted with experimental data, △, from Journée (1992).

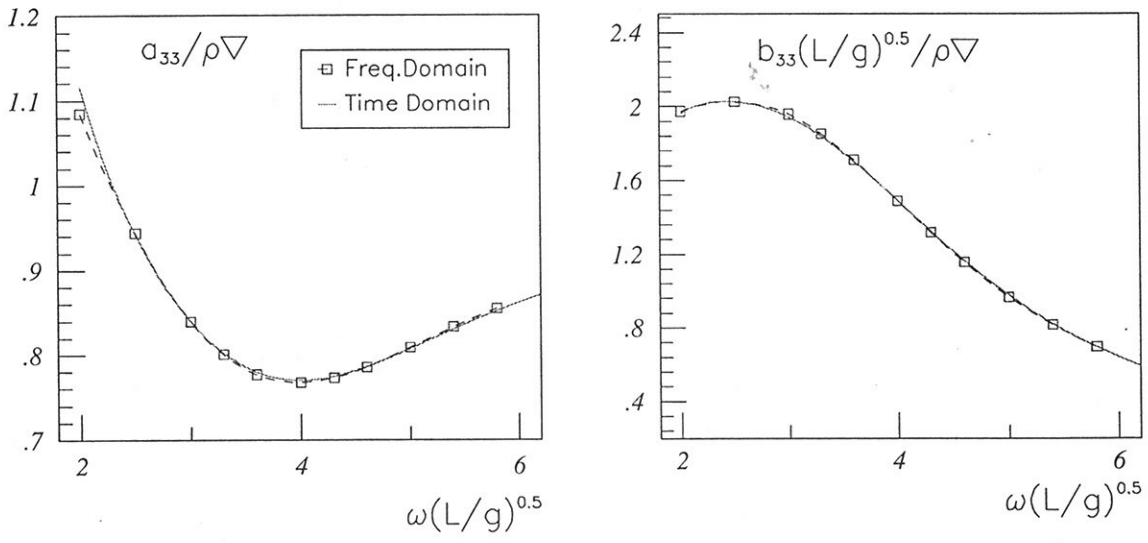

Figure 4: Added mass (left plot) and damping (right plot) coefficients for a heaving S175 hull ($F_n = 0.275$). Present time domain results (solid lines) are compared with frequency domain computations, □.

Comparison of eddy-viscosity and second-moment turbulence closures for a Wing-Body Junction Flow

G.B. Deng & M. Visonneau
Ecole Centrale de Nantes, France

1 Introduction

The turbulent flow around a wing-body junction is a very complex three-dimensional flow despite a simple geometric configuration. It is encountered in many flows of engineering interest such as in aircraft wing and body junction flows, ship appendage and hull junction flows or bridge-pier flows. A wing-body junction flow is characterized by the so-called horseshoe vortex system shed around the obstacle. This vortical structure is composed by two streamwise legs of vorticity, each leg having vorticity of the opposite sense. For practical applications, the behaviour of this vortical structure may be of great interest since many problems like damage to support foundations, excessive level of noise or vibration have their origins in the generation of additional turbulence in the core of the horseshoe vortex.

Recently, many experimental studies emanated from the Virginia Polytechnic Institute (Dickinson [1], Devenport & Simpson [2], Fleming & al. [3], Ölçmen & Simpson [4]). All these authors examined the flow around the same geometry, e.g. a 3:2 elliptical-nosed NACA-0020-tailed cylindrical wing mounted normal to a flat plate and provided many detailed experimental measurements on the mean and fluctuating flows at many different locations. Actually, the wing-body junction flow is an archetypal flow of great interest because of:

- the occurrence of a large region of separated flow ahead of the wing,
- the strong three-dimensionality of the flow field due to two distinct rates of strain generated independently by two different walls,
- the strong turbulence anisotropy associated with the development of the horseshoe vortex.

Therefore, the purpose of this paper is to confront the measurements with computations based on a classical isotropic eddy-viscosity turbulence closure and a new Reynolds-stress transport closure recently developed by the authors.

2 Reynolds-stress closure

The limitations of eddy-viscosity turbulence closures are principally rooted in the fact that the eddy-viscosity models have been designed to provide the correct level of shear stress for flows in which only this stress has a predominant influence. Therefore, the essential inability of eddy-viscosity closures to simulate anisotropic turbulence can explain their bad performances on flows containing recirculating regions or intense vortices, since the turbulence anisotropy strongly influences the magnitude of longitudinal vorticity [5]. With the need to resolve anisotropy taken for granted, the main choice for new statistical turbulence closures is between non-linear eddy-viscosity models and second-moment closures. On complex three-dimensional flows, second-moment closures will have great potentialities because of the exact representation of stress production and transport which enables realistic interactions between normal stress anisotropy and shear-stress components, even if the other physical mechanisms (diffusion, dissipation, redistribution,...) are crudely modeled, especially near the wall. Consequently, modeling of turbulence anisotropy is mandatory and then,

second-moment closures are optimal candidates when high-Reynolds number flows on complex geometries are considered.

2.1 The $R_{ij} - \omega$ model

If one wants to evaluate the true potentialities of second-moment closures on three-dimensional flows, the eviction of wall-function boundary conditions is a prerequisite, because of the frequent strong three-dimensionality of the velocity field near the wall. In this paper, we will use a new near-wall low Reynolds-number model $R_{ij} - \omega$ model which was proposed recently by the authors [6]. The reader is refered to this paper for a extensive presentation of this second-moment turbulence closure.

3 Results and discussion

3.1 Grid sensitivity studies and convergence

The calculations were performed at the experimental Reynolds number of $5.0\,10^5$ on a grid composed of $89 \times 81 \times 81$ nodes, in the streamwise, normal to the wing, and vertical directions. The first coordinate surfaces off the solid walls were located at $y^+ \approx 1.0$ (where $y^+ = u_\tau y_n/\nu$, u_τ is the wall friction velocity and y_n is the normal distance to the wall) with about 15 points within the sublayer and the buffer layer. The solution domain was defined by $-2.0 < X/C < 28.$, $0. < Y/C < 2.0$ and $0. < Z/C < 0.8$ where C is the chord length of the wing and the external boundary conditions are provided by previous infinite flat plate computations.

3.2 Topology of the flow

To explore the structure of the horseshoe vortex predicted by both turbulence models, plots of particle traces in the plane of symmetry and on the flat plate are shown in Figs. 1 and 2. The $R_{ij} - \omega$ solution is characterised by a spiral vortex which is not present in the $k - \varepsilon$ solution.

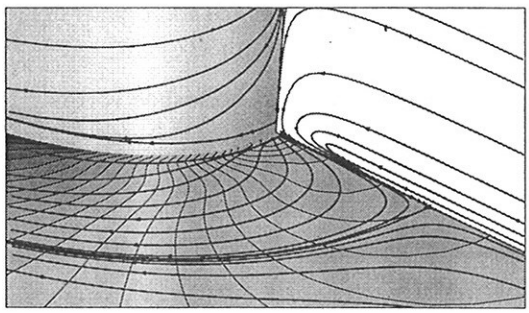

FIG. 1: *$k - \varepsilon$ model- Particle traces in the symmetry plane and on the flat plate (the pressure contours are visible on the flat plate)*

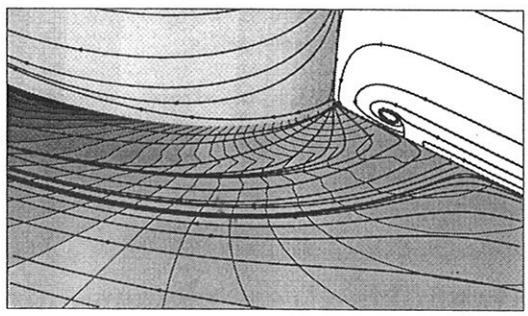

FIG. 2: *$R_{ij} - \omega$ model- Particle traces in the symmetry plane and on the flat plate (the pressure contours are visible on the flat plate)*

Both models predict a primary line of separation located at the intersection between the three-dimensional surface and the flat plate. However, the low-shear stress line which was observed in the experiments between the wing and the primary line of separation is only visible in the second-moment solution, indicating that the secondary motion predicted by the anisotropic turbulence closure is far more intense.

3.3 Results on X=cst. planes

Extensive mean and fluctuating velocity measurements were also conducted by Fleming & al. [3] at several $X/C = cst.$ planes adjacent to the wing and in the wake. These measurements made it possible to characterise the horseshoe vortex development. For the sake of brevity, only one station $X/C = 0.64$ is chosen to compare the respective performances of $k-\varepsilon$ and $R_{ij}-\omega$ models. Figures 3 and 4 show the near-wing contours of U/U_{ref} with both turbulence models at $X/C = 0.64$.

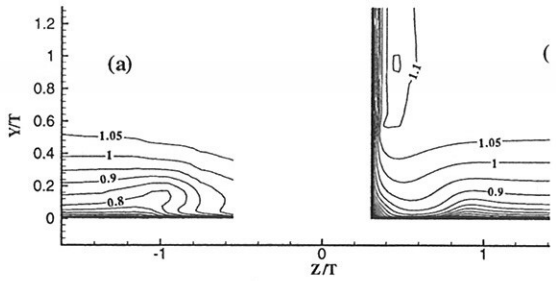

FIG. 3: *Contours of U/U_{ref} at $X/C = 0.64$, (a) Experiments; (b) $k-\varepsilon$ model*

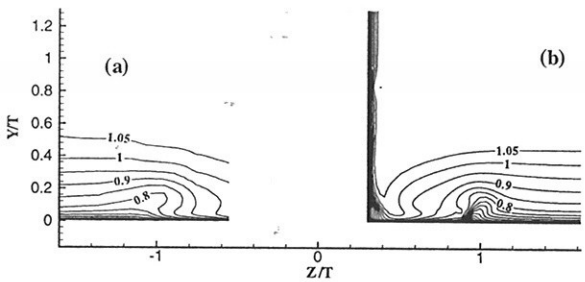

FIG. 4: *Contours of U/U_{ref} at $X/C = 0.64$, (a) Experiments; (b) $R_{ij}-\omega$ model*

The distortion of the iso-velocity contours observed in the measurements are due to the secondary motion which transports higher momentum fluid from the edge of the boundary layer to the near-wall region. This trend is severely underestimated by the $k-\varepsilon$ solution and accurately reproduced by the anisotropic $R_{ij}-\omega$ model which yields a more intense vortical crossflow. Figures 5 and 6 show the contours of the rms Reynolds normal stress u'/U_{ref} at the same station. A local maximum is located in the region where the distorsion of U/U_{ref} contours occurs, indicating that this local peak of turbulence is probably due to the increased mixing of the boundary layer fluid by the horseshoe vortex. The $k-\varepsilon$ solution exhibits a large zone of high normal stress located in the corner between the wing and the flat plate. This high turbulence intensity generates an excessive level of turbulent viscosity which absorbs the secondary motion in the core of the horseshoe vortex. On the contrary, the anisotropic second-moment closures provides a much more physical solution since the local peak of u' is accurately positionned, even if its maximum level is somewhat underestimated.

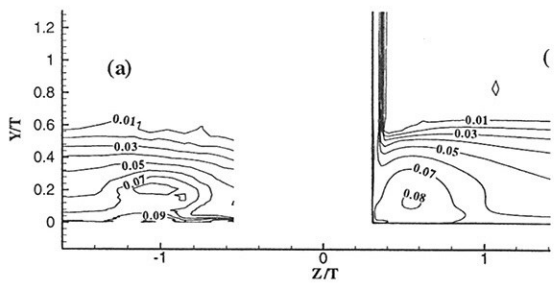

FIG. 5: *Contours of u'/U_{ref} at $X/C = 0.64$, (a) Experiments; (b) $k-\varepsilon$ model*

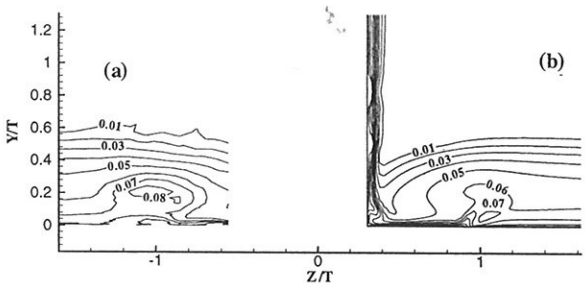

FIG. 6: *Contours of u'/U_{ref} at $X/C = 0.64$, (a) Experiments; (b) $R_{ij}-\omega$ model*

4 Summary and conclusion

A systematic evaluation of a new $R_{ij} - \omega$ model with classical eddy-viscosity closures for a wing-body junction flow has been provided in this paper. Comparisons with global and local quantities, ranging from the velocity components to the Reynolds-stress tensor components have established the clear superiority of the second-moment closure. The new second-moment closure accurately reproduced the anisotropic behaviour of the normal Reynolds stress components, which led to a clear amplification of the longitudinal vorticity. This result clearly demonstrated that second-moment calculations were particularly well suited to three-dimensional vortical flows involving several predominant flow gradients.

5 Acknowledgments

Tabulated experimental data and flow visualization photographs were kindly provided by Prof. R.L. Simpson. Thanks are due to the Scientific Committee of IDRIS and the DS/SPI for attributions of Cpu on the T3E on which most of the calculations were performed.

Références

[1] S.C. Dickinson. An experimental investigation of appendage-flat plate junction flow. *ÐTNSRDC Report 86/052*, 1-2, 1986.

[2] W.J. Devenport and R.L. Simpson. Time-dependent and time-averaged turbulence structure near the nose of a wing-body junction. *Journal of Fluid Mechanics*, 210:23–55, 1990.

[3] R.L. Simpson J.L. Fleming and W.J. Devenport. An experimental study of a turbulent wing-body junction and wake flow. *Experiments in Fluids*, 14:366–378, 1993.

[4] S.M. Ölçmen and R.L. Simpson. An experimental study of a three-dimensional pressure-driven turbulent boundary layer. *Journal of Fluid Mechanics*, 290:225–262, 1995.

[5] C.G. Speziale. On turbulent secondary flows in pipes of non circular sections. *Int. J. Eng. Sci.*, 20:863–872, 1982.

[6] G.B. Deng and M. Visonneau. Computation of a wing-body junction flow with a new reynolds-stress transport model. In *Proc. 22nd Symposium on Naval Hydrodynamics*, 1998.

Yaw flow simulation for the Series 60

A. Di Mascio, E.F. Campana

INSEAN - via di Vallerano, 139 - 00128 Roma - Italy

The question of the behaviour of the flow past a ship advancing with a yaw angle arise in the study of the maneuvering characteristics of marine vehicles.

Previous computations of the viscous free surface flow around a yawed Wigley model was attempted in [1] by using a Domain Decomposition approach and linearized free surface conditions. More recently in [2], [3] the Series 60 has been used and large domain solution have been attempted for the fully non linear problem.

For the present study, numerical simulations have been carried out in the whole domain of the steady yaw flow past a Series 60 $C_B = 0.6$, using a RANS solver and a Full Multi Grid–Full Approximation Storage (FMG-FAS) algorithm to accelerate the convergence. The solution of the free surface viscous steady flow past a ship hull has been obtained as the asymptotic solution of the unsteady pseudo-compressible Navier-Stokes equations [4]. The mathematical model has been approximated by a discrete finite volume model. The computation of the viscous terms at the cell interfaces is made by means of a finite volume approximation of the derivatives of the velocity vector while velocity and pressure at the interface, needed for the computation of the Eulerian fluxes, are evaluated by means of a second order E.N.O.-type scheme [5]. A complete description of these scheme for the simulation of pseudo-compressible flow may be found in [6].

Accurate model-scale experiments [7], have been used to validate computations. The steady motion with a yaw angle $\alpha = 0°, 2.5°, 5°, 10°$ and for $Fr = 0.316$, $Re = 5.27 \times 10^6$ has been computed. In the simulation, as well in the experiments, port region is the pressure side, whereas starboard is the suction side.

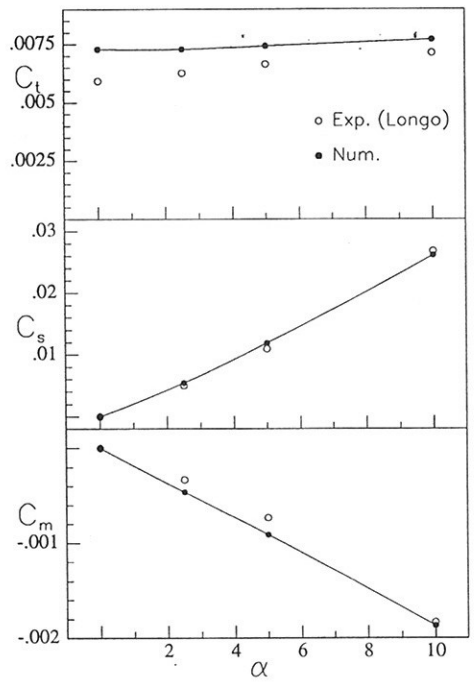

Figure 1: *Comparison between experimental and numerical hydrodynamic coefficients as a function of the yaw angle:* $Fr = 0.316, Re = 5.27 \times 10^6$.

In the numerical computation the fluid domain has been divided into a port and a starboard block: each block has been discretized by using $96 \times 96 \times 64$ cells in stream-wise, normal and girth-wise direction, respectively. Starting from this grid, five coarser grids have been generated by halving in each direction the number of cells of the previous finer grid. Therefore the coarsest grid is $6 \times 6 \times 4$. The Full Multi Grid algorithm was then applied to compute the solution on each grid level.

Accuracy of the numerical method has been established for global quantities, such as the hydrodynamic coefficients, for which monotonic convergence is obtained on the three finer grids. Indeed, the grid doubling procedure used in the Multi Grid approach easily allows to apply some verifications procedures, as suggested in [8]. Estimates of the grid convergence uncertainties have been obtained for global quantities: C_t, C_s, C_m. Figure 2 reports the Grid Convergence Index (GCI), defined as

$$GCI = \frac{F_x^{2h} - F_x^h}{F_x^h} \tag{1}$$

and the computed values of hydrodynamic coefficients as a function of the grid refinement ratio h_c/h, (h_c is the grid step in the coarsest grid) for all the simulated yaw angles. It is worthwhile to notice that monotonic convergence is obtained on the last three finer grids.

The comparison with experimental values is shown in fig. 1, where the hydrodynamic coefficients have been reported as a function of the yaw angle. While the yaw moment and the side force coefficients show a significant increase with the yaw angle, the variation of the total resistance is

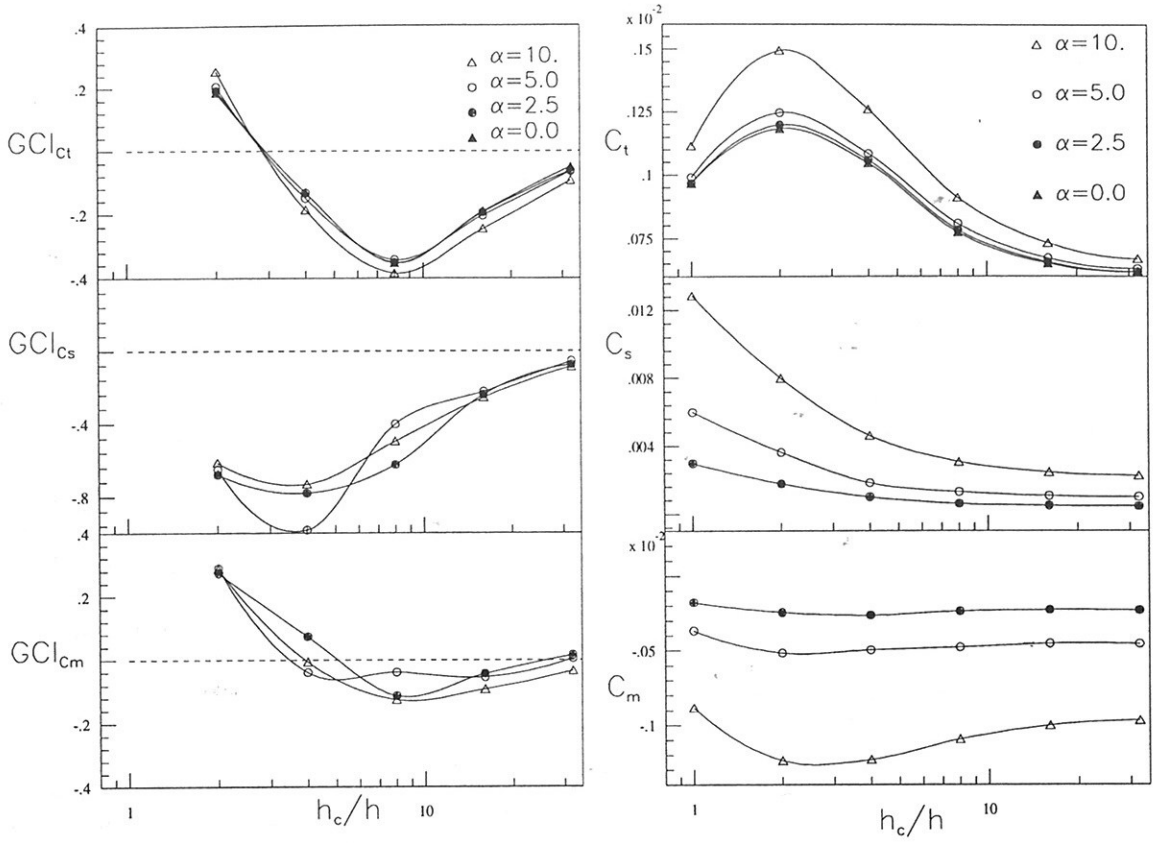

Figure 2: *Grid Convergence Index for the hydrodynamic coefficients* C_t, C_s, C_m *for several yaw angles.* $Fr = 0.316, Re = 5.27 \times 10^6$.

less pronounced. The prediction of the side force and of the yaw moment is satisfactory while some differences are observed in the estimation of the total resistance coefficient, especially in low yaw angles regime, where the numerics over-predict the data by a 20%.

Estimated values of the order of accuracy p, defined as

$$p = \frac{1}{\log 2} \log \left(\frac{f^{4h} - f^{2h}}{f^{2h} - f^{h}} \right) \tag{2}$$

suggests that the asymptotic range was probably reached, at least for the force coefficients.

α	0.0	2.5	5.0	10.0
p_{C_t}	2.00	1.74	1.73	1.52
p_{C_s}	–	1.75	2.05	1.67
p_{C_m}	–	1.46	3.54	1.48

Order of accuracy p for the computed hydrodynamic coefficients for all the yaw angles.

Comparison of the computed wave profiles on the finest grid level with the experiment (figs. 4, 5) reveal a good agreement with measured waves.

Local measurements of the velocity field have been compared with the numerical simulations. The analysis will be focused on the starboard region, where viscous and wave effect is more clearly appreciable. Although global trends are qualitatively predicted, measured data show the presence of a bilge vortex which is not caught in the numerical simulation. At $x = 0.8$ the experimental contours show a detached low speed region whose location is numerically predicted but of smaller intensity. Comparisons for $x = 0.9$, and $x = 1.0$ cross-planes (not showed in this abstract) indicate that the numerical contours are too smooth and that the vorticity in these regions is too weak.

Although comparisons with the data are satisfactory for global coefficients, as well as for wave profiles, contours of the axial velocity in some cross-planes reveal that some of the details of the measured data are still not caught. Indeed, some of the details of the vortex in the starboard region are lost in the simulation. This is clearly shown in fig 3, where the numerical streamline in the cross-plane $x = 1.0$ are compared with data. In the experiments the vortex is approximatively located at $y = 0.02, z = -0.2$ whereas the simulation gives a less intense vortex located at the same depth but at $y = 0.01$.

On the basis of the previous considerations on the convergence properties (see fig. 2), the observed discrepancies seems to be caused by the turbulence model adopted, that induces too strong dissipation of the vortex, rather then by an insufficient grid resolution. However, at the present stage it seems difficult to definitely ascertain the causes of these unsatisfactory prediction of the wake. Further investigations are required to give a more precise answer.

The work was supported by the Italian Ministry of Transportation in the frame of INSEAN research plan 1997-99.

References

[1] Campana E.F., Esposito P.G., Penna R., "Domain Decomposition in Free Surface Viscous Flow", 20-th ONR Symposium on Naval Hydrdynamics, Santa Barbara, 1994.

[2] Campana E.F., Di Mascio A., Penna R., "CFD Analysis of the Flow Past a Ship in Steady Drift Motion", OC '98, Third Osaka colloquium on advanced CFD applications to ship flow and hull form design, May 1998.

[3] Tahara Y., Longo J., Stern F., Himeno Y., " Comparison of CFD and EFD for the Series 60 $C_B = 0.6$ in Steady Yaw Motion", 22-nd ONR Symposium on Naval Hydrodynamics, Aug. 1998.

[4] Chorin A., "A Num. Method for Solving Incomp. Viscous Flow Problems", J. Comp. Phys, 2, 12, 1967.

[5] Harten A., Engquist B., Osher S., Chakravarthy S.R., "Uniformly High Order Accurate Essentially Non–Oscillatory Schemes", J. Comp. Phys., 71,231,1987.

[6] Di Mascio A., Broglia R., Favini B., "Numerical simulation of free-surface viscous flow by ENO-type schemes", 3-rd Int. Conf. on Hydrod., Seul (Korea), Oct. 1998

[7] Longo J.,Ph.D. Thesis, Dept. of Mech. Eng., Univ. of Iowa, 1996.

[8] Coleman, W.H., Stern, F., "Uncertainties and CFD Code Validation", J. Fluids Eng., 119, 795-803, 1888, 1997.

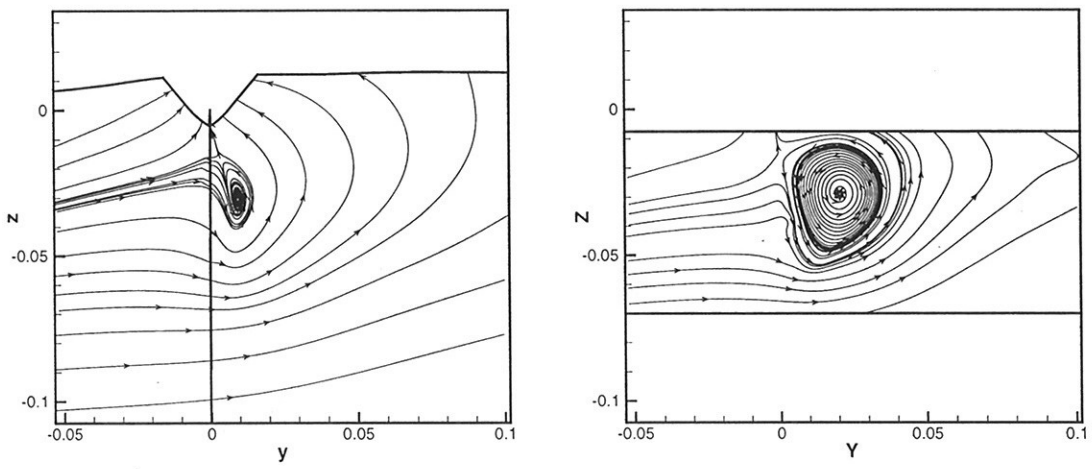

Figure 3: *Numerical streamlines (left) of the $x = 1.0$ cross-plane are reported in comparison with experimental data by Longo (right).*

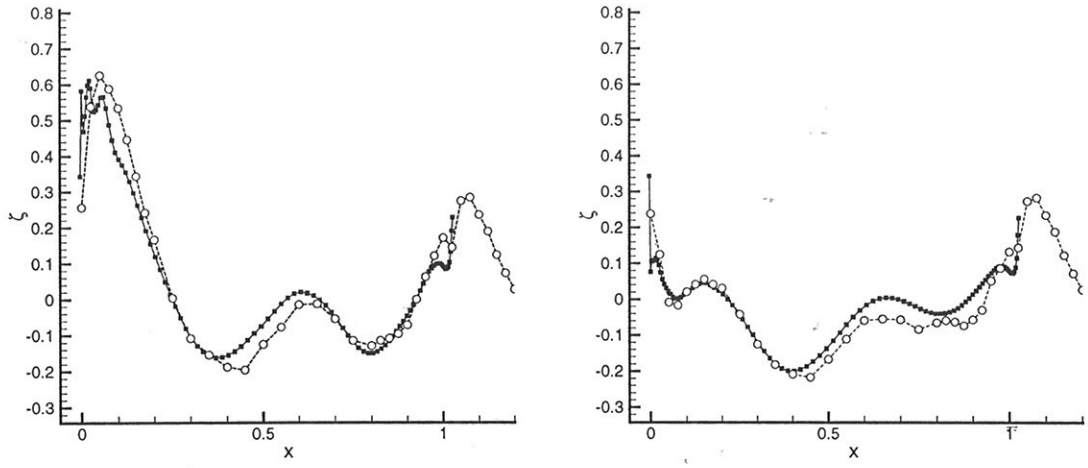

Figure 4: $\alpha = 10°$ *Numerical (solid) and experimental (dashed) wave profiles. Left, port; right, starboard.*

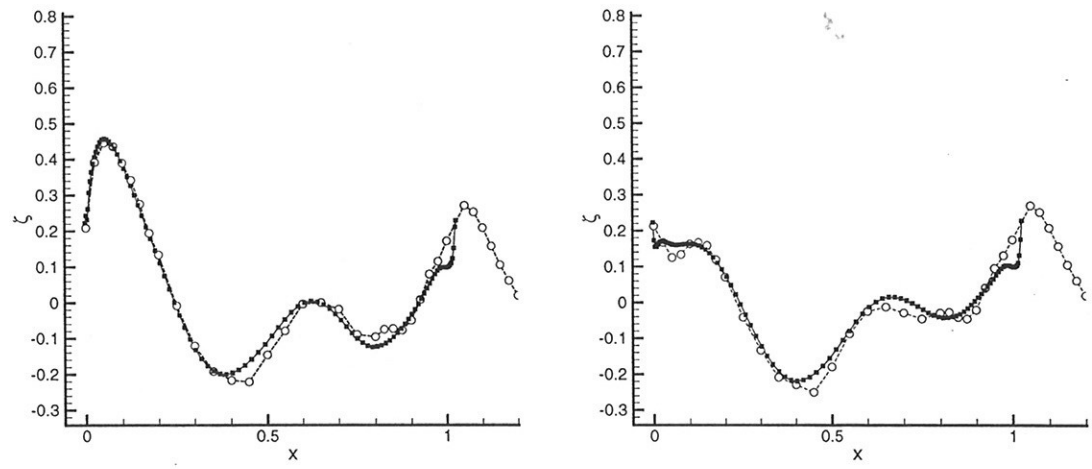

Figure 5: $\alpha = 5°$ *Numerical (solid) and experimental (dashed) wave profiles. Left, port; right, starboard.*

Viscous Flow Computations around Rudders

Ould El Moctar
Technical University Hamburg-Harburg, AB 3–13, Lämmersieth 90, D-22305 Hamburg, Germany

Rudders, placed behind the propeller(s), increase the propulsive efficiency by using part of the rotational energy contained in the propeller slipstream. Rudder forces (lift, drag and stock moment) are required in evaluating the manoeuvrability of ships, in determining a rudder gear size and for structural design of the rudder. Potential theory is widely used to investigate rudder characteristics. In addition Söding's [1] empirical formulae based on measurements in uniform flow and potential theory are used in practice to determine rudder forces. Potential theory is unable to predict stall conditions due to neglecting the viscous effects. Model experiments are carried out at lower Reynolds numbers (R_n) and are of limited significance. The use of the RANSE method is a better approach to analyse the flow around a rudder than the potential theory, especially regarding the possibility of flow separation. In the present study the turbulent flow around rudders with different aspect ratios, profile shapes and thickness in uniform flow are computed at both model and full scale R_n. Different methods of grid generation were investigated. The standard k-ϵ model with wall functions is applied.

The conservation equations for mass and momentum in their integral form [3] serve as the starting point.The solution domain is subdivided in a finite number of CV's which may be of arbitrary shape. Normally, hexahedral cells are used whose each side can be subdivided in any number of faces when the neighbour cell is refined. The conservation equations are applied to each CV, and the integrals are numerically approximated using the midpoint rule approximation. the gradient is calculated using a conservative approximation of second order. The discretized continuity equation is transformed into a pressure-correction equation following the SIMPLE algorithm, adapted to colocated grids. The momentum component equations are linearized using the Picard iteration scheme. The k-ϵ model is adopted to determine the Reynolds stress in Ranse. The eddy viscosity μ_t is expressed using the turbulent kinetic energy k and its dissipation ϵ. The standard set of model constants were used [3]. The discretization and linearization leads to a system of coupled algebraic equations, which is solved by a segregated iterative approach. The inter-equation coupling and non linearities are resolved in a predictor-corrector scheme within outer iterations, which represent the update of the coefficient matrix and source vector. For more details see [3].

The fact that the solution method is designed to use unstructured grids made of CV's with an arbitrary number of faces and with cell-wise refinement allow good flexibility in the grid generation. Different kinds of grid were investigated. the C-Grid is often used for foil configurations. the solution domain consists of an unstructured C-grid with a local refinement of cell layers around the rudder. The mesh spacing becomes smaller toward the edges of the rudder to resolve the tip vortex, Fig. 1. If the rudder is placed behind a propeller, the flow is not uniform and the rudder should be rotated. in this case, it is proposed to put the rudder in a cylinder block, which can be rotated inside the fixed block without changing the shape of the CV's, Fig. 2. The CV's along non matching interfaces are thus treated as polyeder with many faces.

In the following, rudder lift L, drag D and stock moment M are represented by non-dimensional lift, drag and moment coefficients:

$$C_l = \frac{L}{\frac{1}{2}\rho v^2 hc}, \quad C_d = \frac{D}{\frac{1}{2}\rho v^2 hc}, \quad C_m = \frac{M}{\frac{1}{2}\rho v^2 hc^2}$$

v is the uniform inflow velocity, ρ the fluid density, h the rudder height and c the mean chord length. The rudder aspect ratio is defined as $A_r = \frac{h}{c}$. The lift generated by a rudder is the

most important quantity characterising its manoeuvring performance, whereas the rudder drag determines its influence on propulsion power. The moment required to turn a rudder about its shaft is refer to a point about 25%c behind the rudder nose to make this moment as small as possible. The non-dimensional rudder forces and moment are computed here to compare the performance of different rudder designs.
The dependence of numerical solutions on grid resolution was studied by comparing the results obtained on three grids consisting of 120.000, 480.000 and 860.000 CV's. The differences were of the order of 3%, which is the upper limit on discretization errors.

Reynolds number effects
Rudder experiments are usually carried out at R_n which are one to two orders of magnitude smaller than in full scale. To demonstrate the R_n effect, the rudder flow was computed at $R_n = 5 \cdot 10^7$ and $R_n = 2.7 \cdot 10^6$ for the same rudder. Whicker and Fehlners's experiments [6] with this rudder model ($R_n = 2.7 \cdot 10^6$) in a wind tunnel were compared with the numerical results. The computation shows that the larger R_n results in a larger stall angle, whereas results before stall are practically not influenced, Figs. 3-5. The numerical solution agrees very well with the measurements of lift, drag and stock moment except after stall. These deviations are probably due to the turbulence model in view of the massive separation beyond the stall angle.

Aspect ratio effects
Two rudders, with the same profile shape NACA0015 and taper ratio (T_r) 0.45, are investigated at $R_n = 2.7 \cdot 10^6$ and $R_n = 5 \cdot 10^7$ with two different aspect ratios, $A_r = 1.0$ and 3.0. The rudder with the greater aspect ratio produces twice as high lift for a given angle of attack compared with the low-A_r rudder. The maximum lift coefficient is practically independent of the aspect ratio, the drag coefficient remains nearly unchanged, Figs. 6-8.

The effects of profile shape and thickness
NACA profiles are often used as rudder profiles. In order to increase the produced maximum lift or to avoid cavitation problems, other profiles were developed. The flow around three rectangular rudders with profile shapes NACA 0025, HSVA MP73-25 and IfS 62TR25 [1], all having thickness of 0.25c, have been studied at $R_n = 5 \cdot 10^7$. The computed $C_{l,max}$ of the IfS and HSVA rudders are 13% and 10% larger than that of the NACA profile respectively. The HSVA profile has a larger stall angle than NACA and IfS profiles, Fig. 9. The advantage of the NACA profile is the substantially smaller drag, Fig. 10. These effects were also shown by model experiments carried out at small R_n, see [5].
Thick concave profiles (HSVA,IfS) increase both the lift gradient and the maximum lift. Grater NACA profile thickness produces less lift for the same angle of attack. Thick profiles should be avoided because of their larger drag, and the danger of cavitation in high-speed ships, Figs. 10-11.

The computed results for force and moment agree well with measurements and, thus appear accurate enough for various practical applications, especially for optimising the rudder shape. The full-scale Reynolds number results in larger maximum lift and stall angle. A larger Aspect ratio gives a larger lift gradient and an unchanged stall angle. The IfS and HSVA profiles produce substantially more lift than the NACA profile, but also higher drag. Thick concave profiles (HSVA,IfS) increase both the lift gradient and the maximum lift.
The current research will concentrate on including the propeller to analyse its interaction.

[1] Brix, J. (1993), Manoeuvring Technical Manual, Seehafen Verlag
[2] El Moctar, O. (1997), Berechnung von Ruderkräften, IfS Rep. 582, Univ. Hamburg
[3] Ferziger, J.H., Perić, M. (1996), Computational Methods for Fluid Dynamics, Berlin: Springer-Verlag
[4] Söding, H. (1998), Limits of potential Theory in Rudder Flow Predictions, Ship Techn. Res. 45
[5] Thieme, H. (1962), Zur Formgebung von Schiffsrudern, Jahrbuch Schiffbautechn. Gesellschaft
[6] Whicker, L.F.; Fehlner, (1958), Free-stream characteristics of a family of low-Aspect ratio, All-Movable Control Surfaces for Application to Ship Design, Report 933, David Taylor Model Basin

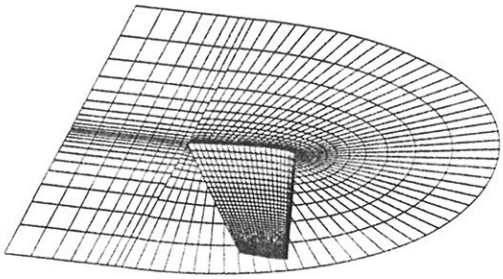

Fig.1 C-grid

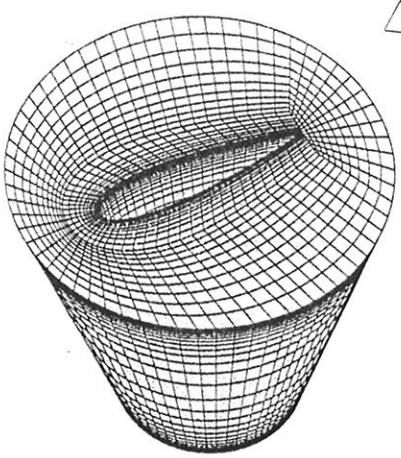

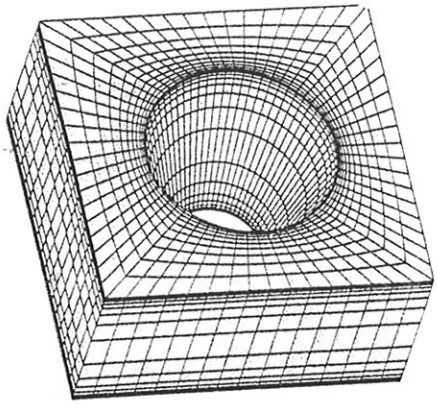

a) b)

Fig.2 Cylindrical rudder block (a) and the surrounding block (b) in the combination of O and H grid blocks

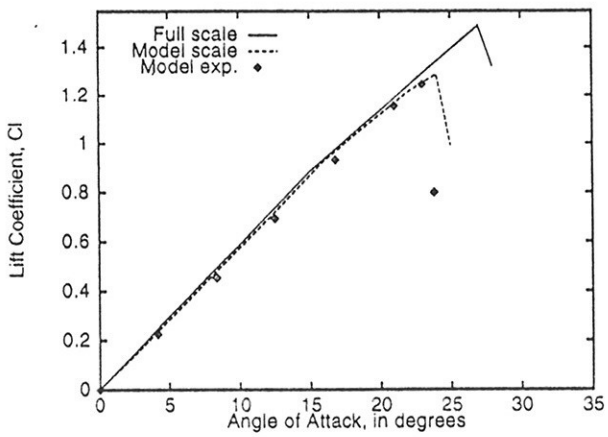

Fig.3: Lift of rudder NACA0015

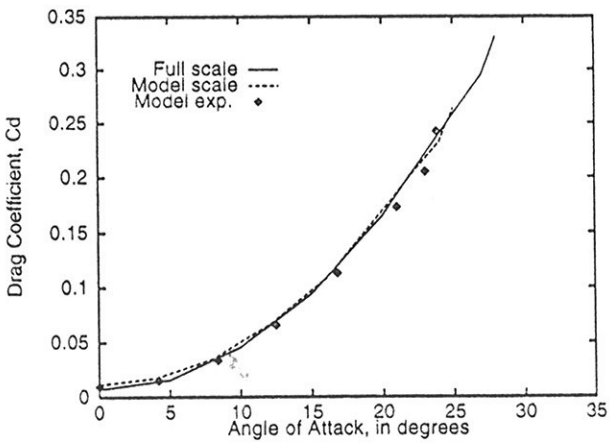

Fig.4: Drag of rudder NACA0015
$A_r = 3$, $T_r = .45$, $R_n = 2.7 \cdot 10^6$, and $R_n = 5. \cdot 10^7$

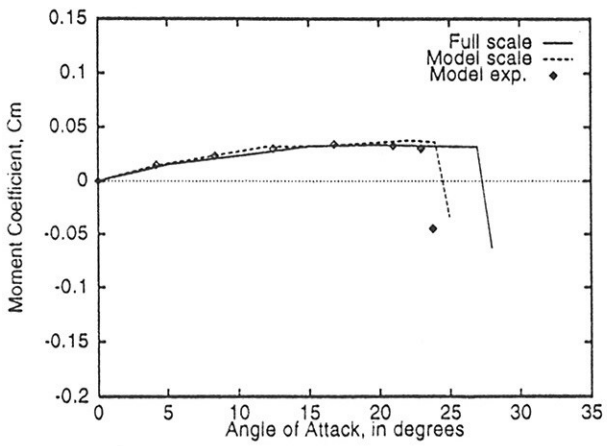

Fig.5: Stock moment of rudder NACA0015
$A_r = 3$, $R_n = 2.7 \cdot 10^6$, and $R_n = 5. \cdot 10^7$

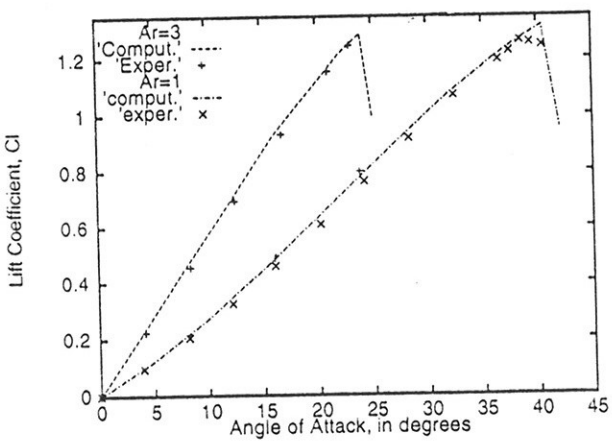

Fig.6: Lift of rudder NACA0015
$A_r = 3$, $A_r = 1$, $R_n = 2.7 \cdot 10^6$

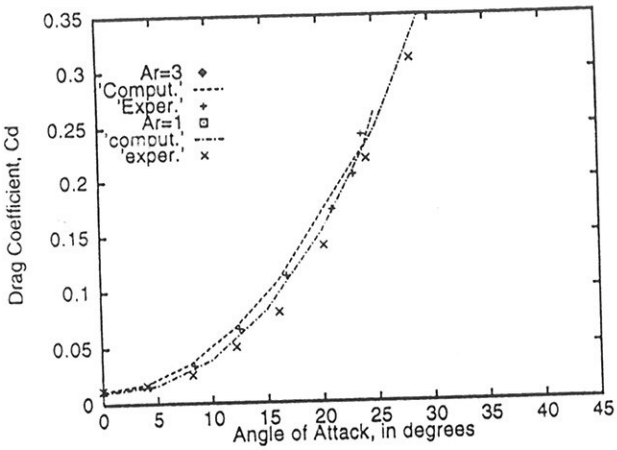

Fig.7: Drag of rudder NACA0015
$A_r = 3$, $R_n = 2.7 \cdot 10^6$, and $R_n = 5. \cdot 10^7$

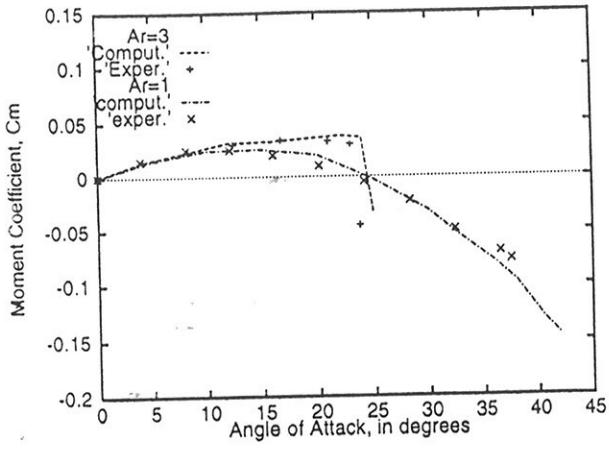

Fig.8: Stock moment of rudder NACA0015
$A_r = 3$, $A_r = 1$, $R_n = 2.7 \cdot 10^6$

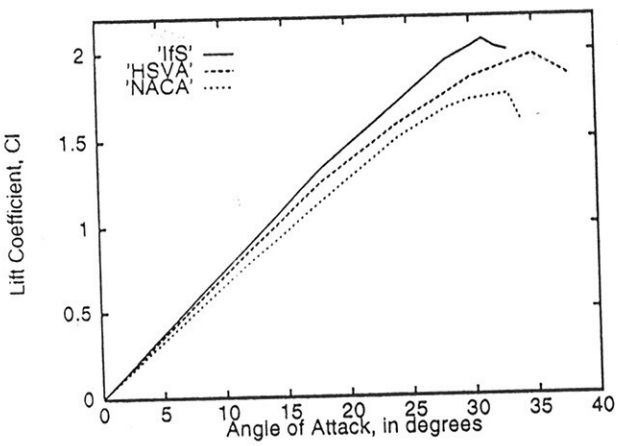

Fig.9: Lift of Rudders with different profiles

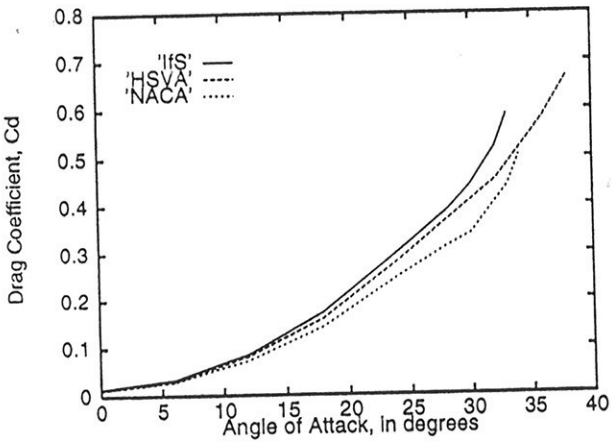

Fig.10: Drag of Rudders with different profiles
$A_r = 4$, $R_n = 5. \cdot 10^7$, $T_r = 1$

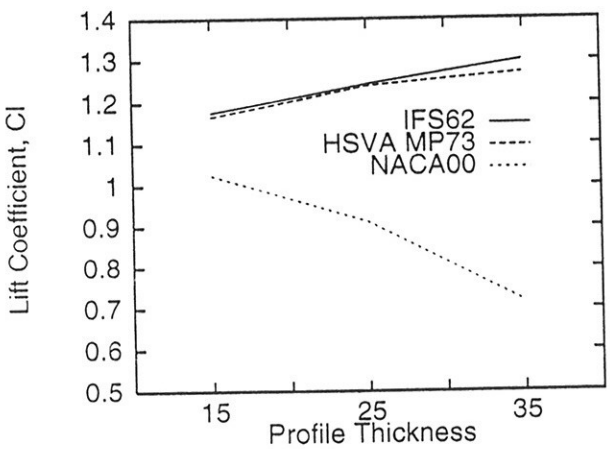

Fig.10: C_l Different profiles with variable thickness

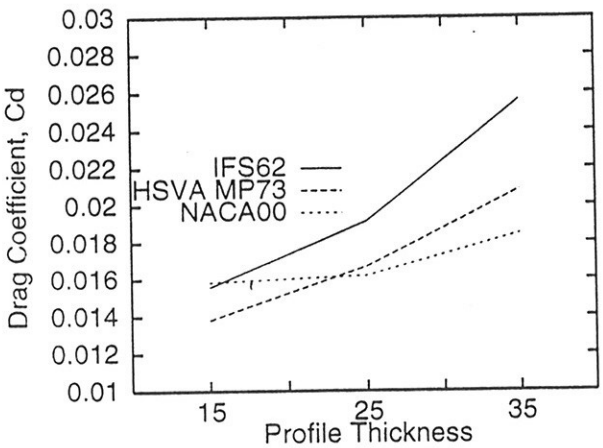

Fig.11: C_d different profiles with variable thickness
$A_r = \infty$, $R_n = 5. \cdot 10^7$

Simulation of Ship Tactical Circle Maneuvers Using Recursive Neural Networks

David E. Hess and William E. Faller,
William E. Smith and Thomas T. Huang
Carderock Division, Naval Surface Warfare Center
9500 MacArthur Blvd
West Bethesda MD 20817-5700 USA

A method is described in which recursive neural networks (RNN) are used to predict the time histories of maneuvering variables of full scale surface ships conducting tactical circle maneuvers in the open ocean. Full scale data describing a series of tactical circle maneuvers with varying rudder deflection angles and approach speeds have been acquired for each of two ships, and these data have been used to train and validate two neural networks, one for each ship. Upon completion of training, typical time histories of the control variables: two propeller shaft speeds and two rudder deflection angles, may be input into the neural networks and predictions of the time histories of the state variables: linear and angular velocity components, will be obtained. These data can then be used to recover the remaining hydrodynamic variables required to describe the motion of the vehicle. The ongoing application of neural network technology to the simulation of ship maneuvers is showing significant promise and is expected to yield a plant model that can then be used for the development of an RNN based model reference control system.

The simulated maneuvers are tactical circles which are conducted in order to determine the inherent turning characteristics of the ship. Of particular interest are such quantities as advance, transfer, tactical and steady diameters, speed loss and steady speed in the turn. The typical procedure for these maneuvers is to first establish steady initial conditions for approach velocity and desired shaft speeds and to maintain these conditions for 30 seconds. Then, an order to Commence Execution (COMEX) of the run is given. Data acquisition at a rate of 1 Hz begins and steady conditions are maintained for an additional 60 seconds. At this time an EXECUTE command is given and the rudders are deflected to the desired angle and maintained for the duration of the maneuver. These conditions are continued until the heading of the vehicle has changed by 540 degrees; the maneuver is then terminated. An ideal tactical circle maneuver illustrating these terms is shown in Fig. 1.

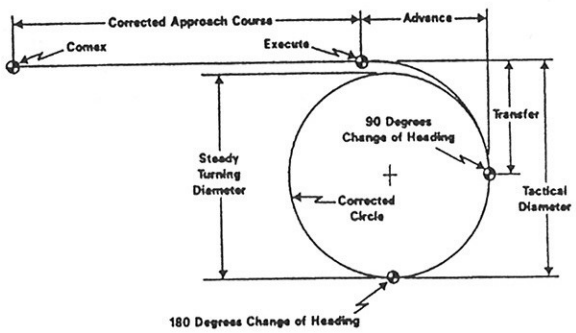

Figure 1. Tactical circle maneuver.

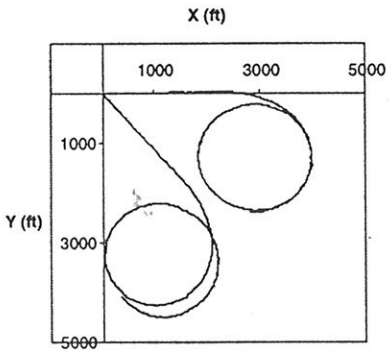

Figure 2. Typical uncorrected and corrected tactical circles.

However, conditions in the open ocean are rarely ideal. Environmental factors such as moderate winds, unfavorable ocean currents and moderately rough seas can combine to produce the actual circle trajectory shown in Fig. 2. Note that the standard right-handed coordinate system with the z-axis positive downwards is used. Knowledge of the time histories of wind speed and direction along with details of the prevailing ocean currents should allow one to formulate the appropriate force contributions which alter the trajectory of the vehicle, and this is one of the areas in which future efforts will be directed. However, for these first attempts to simulate these maneuvers with recursive neural networks, the problem was simplified by attempting to remove environmental effects. For this reason, an automated procedure for removing the

effects of drift was devised and applied to each of the maneuvers. An example of the corrected circle, rotated for convenience to place the steady state approach along the x-axis, is also shown in Fig. 2. The data consist of maneuvers with rudder deflection angles which vary over a range of 10 degrees to 35 degrees and for a series of approach speeds from 10 knots to 30 knots. Because ships with multiple propellers often exhibit similar turning characteristics for both right and left turns, the bulk of the data are right turns with a small number of left turns.

The maneuvering quantities required to describe the motion of the vehicle are the trajectory components $x(t)$, $y(t)$ and $z(t)$ referred to an inertial coordinate system typically oriented as in Fig. 2; the Euler angles consisting of roll $\varphi(t)$, pitch $\theta(t)$ and yaw $\psi(t)$ which describe the orientation of the body coordinate system, placed at the center of gravity of the vehicle, relative to the inertial coordinate system; the velocity components $u(t)$, $v(t)$ and $w(t)$; the acceleration components $\dot{u}(t)$, $\dot{v}(t)$ and $\dot{w}(t)$; the angular velocity components $p(t)$, $q(t)$ and $r(t)$; and the angular acceleration components $\dot{p}(t)$, $\dot{q}(t)$ and $\dot{r}(t)$. In addition, the speed $U(t)$ of the vehicle may be measured or derived from $U = \sqrt{u^2 + v^2 + w^2}$, and these latter quantities are all referred to the body coordinate system. The time histories of the control signals directing the vehicle consist of the two rudder deflection angles, $\delta_{r1}(t)$ and $\delta_{r2}(t)$, and the two propeller shaft speeds, *RPM1* (*t*) and *RPM2* (*t*).

The maneuvering quantities actually measured during tactical circles are the control signals, the trajectory components, x and y, which result from Global Positioning System (GPS) measurements, the Euler angles and the speed. In the absence of knowledge of z and in conformity with the desire to minimize environmental effects, z is set to zero. This information is sufficient to derive the time histories of the remaining maneuvering variables described above. Therefore, prior to training the neural network, all maneuvering data is operated on by computer codes which were developed to: extract the needed variables from the raw data files, correct the circles, derive missing kinematic variables, digitally lowpass filter the time histories to remove noise, and verify mathematical consistency among all variables for each maneuver and across the set of maneuvers.

The recursive neural network employed in this work is a computational technique for developing a time-dependent nonlinear equation system which relates input control variables to output state variables. The neural network is *recursive* which indicates the use of feedback; namely, the information stream issuing from the outputs is redirected to form various additional inputs to the network. Such a model is particularly well suited for nonlinear, time-dependent problems for which the past history of the process is required. The current neural network model is adapted for use with surface ship exercises from technology developed for previous work with submarine maneuvers [1], and additional information describing applications may be found in the references [2,3].

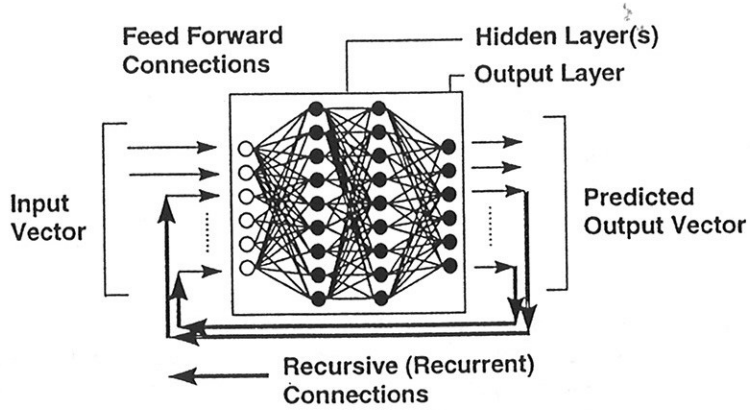

Figure 3. Schematic of the recursive neural network.

The architecture of the network is indicated schematically in Fig. 3; it contains an input layer, two hidden layers and an output layer with the nodes in each layer fully connected to those in the next layer. Each

hidden layer uses bias units and contains 48 nodes using the binary sigmoid activation function. The output layer consists of 6 nodes, also using binary sigmoids, which predict at each time step dimensionless forms of the six state variables: u, v, w, p, q and r. The output layer does not use bias units. The input vector contains 49 contributions which are necessary to describe the forces imparted by the control inputs and the influence of time-dependent flow field effects; these are described as follows. The two rudder deflection angles are used to formulate rudder force expressions by making use of knowledge (predicted from the previous time step) of squared speed and a computed effective angle of attack at the rudder. These two rudder forces at the current time step represent two inputs. An additional 20 inputs are obtained by retaining the values of each input rudder force from the immediately preceding 10 time steps and providing them as inputs for the current time step. The two propeller shaft speed values for the current time step are put in a dimensionless form using a characteristic length (propeller diameter) and speed (predicted from the previous time step) and represent two inputs. An additional two inputs at the current time step are obtained by using the values from the immediately preceding time step for these two expressions. A hydrodynamic force on the hull at the current time step is approximated with a simple expression employing a computed sideslip angle and speed squared (predicted from the previous time step) and represents one input; similarly, values from the immediately preceding 10 time steps are retained and provided as an additional ten inputs for the current time step. The remaining 12 inputs are obtained by using the 6 recursed outputs from the previous time step as well as the six outputs from the time step before that. The *time step* referred to above at each iteration of the neural network represents a step in dimensionless time. Time is rendered dimensionless using a characteristic length (ship length) and speed computed from the preceding iteration; thus, it represents a fraction of the time required for the flow to travel the length of the hull. The neural network is stepped at a constant rate in dimensionless time through each maneuver.

A subset of the tactical circle maneuvers is chosen to train the neural network, and the training set is presented on the order of 40,000 to 80,000 times before training is concluded. During this process, the predicted outputs are compared to the measured outputs, and a modified form of the gradient descent (backpropagation) algorithm is used to adjust the weights. The maneuvers excluded from the training set, and therefore not previously *seen* by the neural network, are used to test the ability of the network to simulate tactical circle maneuvers based on novel rudder deflection and propeller shaft speed time histories. Specifically, of the 15 tactical circles available for the first ship, 12 (80%) were used for training and 3 were retained as novel maneuvers; for the second ship, the training set consisted of 20 maneuvers with 5 circles (20%) retained for testing purposes.

Preliminary results measuring the performance of the neural network for the first ship for three variables of critical importance for tactical circles are presented in the Table. For each variable, these error measures are averaged over each point in the time history and then over all of the available maneuvers. For comparison, the second number in each cell of the Table is averaged over the validation maneuvers only. Note that the Average Angle Measure developed by the Maneuvering Code Certification Board at the Naval Surface Warfare Center is a dimensionless performance measure for which a value of 1.0 represents perfect agreement between measured and predicted variables and a value of 0.0 indicates no agreement.

Variable \ Errors	Absolute Error	Avg. Angle Measure	Correlation Coefficient
u	0.30 / 0.65 kn	0.981 / 0.959	0.973 / 0.943
x	62.7 / 138.5 ft	0.986 / 0.970	0.993 / 0.974
y	67.8 / 147.8 ft	0.942 / 0.874	0.992 / 0.969

Table. Error measures averaged over all files / validation files for neural network.

As mentioned above, the circle maneuvers were performed for a range of rudder deflection angles and therefore a range of steady turning diameters were obtained. If one selects an average turning diameter of 2200 ft and uses this value to normalize the absolute errors in x and y, then the absolute errors are on the

order of 3% averaged over all of the circles and 6.5% for validation circles only. Similar percentages are obtained if one uses an average steady speed in the turn of 10 kn to normalize the absolute error in u.

Representative examples of the predicted trajectory (dark curve) and the measured trajectory (light curve) for a training maneuver and a validation maneuver are presented in Fig. 4 and Fig. 5, respectively. The predicted trajectories are indeed circles and notice that such characteristics as advance, transfer, and tactical and steady turning diameters are captured quite accurately. Results for the other maneuvering variables are of similar quality and will be presented.

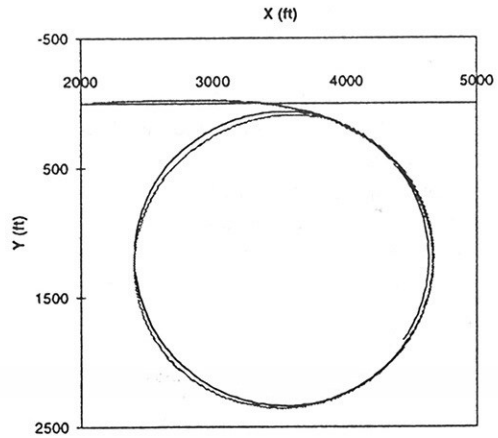

Figure 4. Training run 3062.

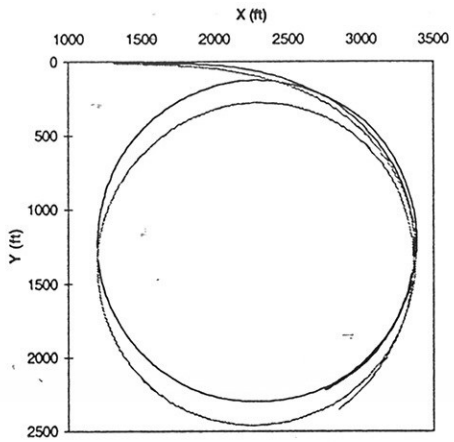

Figure 5. Validation run 3042.

The initial results are encouraging and indicate that recursive neural networks, which enjoy advantages of simplicity and faster-than-real-time speed, may be used for the prediction of time histories of maneuvering variables of full scale surface ships conducting tactical circle exercises. Data describing horizontal overshoot maneuvers for these two ships are also available, and future efforts will be directed towards the simulation of these maneuvers as well.

This work is sponsored by the U.S. Office of Naval Research. The program monitors are Dr. Teresa McMullen, Code 342 and Dr. Pat Purtell, Code 333.

References

1. Faller, W.E., Smith, W.E. and Huang, T.T., "Applied Dynamic System Modeling: Six Degree-Of-Freedom Simulation Of Forced Unsteady Maneuvers Using Recursive Neural Networks", AIAA Paper 97-0336, 35th AIAA Aerospace Sciences Meeting (1997).

2. Faller, W.E., D.E.Hess, W.E.Smith and T.T.Huang "Applications of Recursive Neural Network Technologies to Hydrodynamics", Twenty-Second Symposium on Naval Hydrodynamics, Washington, D.C., August 9-14, 1998.

3. Faller, W.E., D.E.Hess, W.E.Smith and T.T.Huang "Recursive Neural Networks: Six Degree-Of-Freedom Simulation Maneuvering Simulation Capabilities", AIAA Paper 98-2731, 29th AIAA Fluid Dynamics Conference, June 15-18, 1998.

Large Eddy Simulation around a LEBU Drag Reduction Device

Munehiko Hinatsu, Yoshiaki Kodama and Masahiko Makino *

1. Introduction

Recently research in drag reduction has been carried out mainly in mecahnical engineering and this topic is also very atractive in ship hydordynamics because these techniques would have great effects in economic and enviromental problems. The techniques are categorized into active methods and passive methods. Typical example of an active method is microbubbles. This method requires power to inject bubbles into the boundary layer. On the other hand, a typical example of a passive method is a large eddy break up (LEBU) device, which is considered a promising method.

Researches in drag reduction have been mostly experimental. However, flow visualization techniques were mainly used in those experimental works, and information obtained through them is limited. On the other hand, we can obtain a lot of information about turbulence if we use large eddy simulation (LES), and the authors have simulated flows around a LEBU using LES to investigate turbulence properties and the drag reduction mecahnism. Some of the results are presented and discussed herein.

2. LES with the Dynamic SGS Model

In the present study, we used a Large Eddy Simulation(LES) for the simulation of turbulent flows. The space-filtered Navier-Stokes equations are

$$\frac{\partial \overline{u}_i}{\partial t} + \frac{\partial}{\partial x_j}(\overline{u}_i \overline{u}_j) = -\frac{\partial \overline{p}}{\partial x_i} - \frac{\partial \tau_{ij}}{\partial x_j} + \frac{1}{R_e}\frac{\partial^2 \overline{u}_i}{\partial x_j^2} \quad (1)$$

where

$$\tau_{ij} = \overline{u_i u_j} - \overline{u}_i \overline{u}_j = L_{ij} + C_{ij} + R_{ij} \quad (2)$$

here, the overbar denotes a space-filtered variable. $L_{ij} = \overline{\overline{u_i}\,\overline{u_j}} - \overline{u_i}\,\overline{u_j}$ and $C_{ij} = \overline{\overline{u_i} u_j'} + \overline{u_i' \overline{u_j}}$ are Leonard stresses term and the Cross term, both of which are neglected in the present study.

The remaining part $R_{ij} = \overline{u_i' u_j'}$, is the subgrid scale stress term, modeled by the following equation.

$$R_{ij} = -\nu_e S_{ij} + \frac{1}{3}\delta_{ij} R_{kk}, S_{ij} = \frac{1}{2}\left(\frac{\partial u_i}{\partial x_j} + \frac{\partial u_j}{\partial x_i}\right) \quad (3)$$

$$\nu_e = 2(C_s \Delta)^2 \sqrt{2 S_{ij} S_{ij}} \quad (4)$$

The coefficient C_s in equation(4) is evaluated dynamically by the Germano model[1] with Lilly's least square method[2]. Then,

$$C_s = -\frac{\mathcal{L}_{ij}^* M_{ij}}{M_{ij} M_{ij}} \quad (5)$$

with the following relations.

$$M_{ij} = 2\overline{\Delta}^2(\alpha^2 - 1)|\tilde{\overline{S}}|\tilde{\overline{S}}_{ij}, \quad \tilde{\overline{\Delta}}/\overline{\Delta} = \alpha \quad (6)$$

$$\mathcal{L}_{ij}^* = \mathcal{L}_{ij} - \frac{1}{3}\mathcal{L}_{kk}\delta_{ij}, \quad \mathcal{L}_{ij} = \widetilde{\overline{u}_i \overline{u}_j} - \tilde{\overline{u}}_i \tilde{\overline{u}}_j \quad (7)$$

The tilde denotes the variables to which the test filtering is applied, whose width is wider than the grid filter used in the space-filtering process to get equation (1).

$\tilde{\overline{u}}$ in $\mathcal{L}_{ij}$ is evaluated with the following approximation [3].

$$\tilde{\overline{u}} = \int \tilde{G}(x,y)\overline{u}(y)dy \sim \overline{u}(x) + \frac{1}{24}\tilde{\Delta}^2 \overline{u}_{xx} + \cdots \quad (8)$$

3. Computational Scheme

A staggered grid in Cartesian coordinates is used. Second order central differencing is used in the space discretization. Time integration is done by a second order Runge-Kutta method. No upwind scheme is used for discretizing the convection term. C_s estimated by eq.(5) is further averaged in the plane parallel to the wall. Velocity - pressure coupling is based on the SMAC method and the pressure Poisson equation is solved by the Line SOR method.

*Ship Research Institute

4. Computed Results - Channel Flow -

In order to validate the present computational code, we solved a parallel channel flow. The dimension of the computational domain is $x = 2.85, y = 1, z = 1.6$, where x is the longitudinal axis, y is the vertical axis and z is in the spanwise direction. The number of grid points is $(33 \times 41 \times 33)$. In the spanwise directions, equi-width grids are set. Grids are clustered near the wall using *tanh* function.

Since our target is to solve a flow with LEBU, the domain decomposition technique is useful for this problem. So we devided the computation domain into two blocks, lower half and upper half even in the computation of the plain channel flow. Further, considering this fact, a different mesh size is used in the following regions, $-1.35 \leq x \leq -0.5, -0.5 \leq x \leq 0.5$ and $0.5 \leq x \leq 1.5$. The number of mesh cells are set to 10, 10,and 13, respectively in each part. Equispaced grid is used in each region. By solving a simple channel flow with such a complicated grid system, we can validate the grid dependence on the solution.

A negative pressure gradient $\partial p/\partial x = -2$ is applied to keep the flow quasi-steady. Reynolds number $Re = 500$ is assigned and time step Δt is set as 0.0005. The initial flow profile is given by the logarithmic profile with small random disturbances. Periodic boundary conditions are imposed in the x and z directions and the non-slip condition is used at the wall.

Fig. 1 shows the log-profile of velocity. The velocity profile approaches to $y^+ = u^+$ near the wall and in the log-region, computed profile agrees with the log-equation, although the computed result is slightly larger. In Fig.2, we show the turbulence intensities $\sqrt{u'u'}, \sqrt{v'v'}$ and $\sqrt{w'w'}$ with lines. Symbols in the figure are the experimental results given by Kreplin & Eckermann[4]. Note that Kreplin's data are results with $Re = 389$. $\sqrt{u'u'}$ distribution agrees well with the experimental data considering that the higher the Reynolds number is, the greater the turbulence intensity becomes. But $\sqrt{v'v'}$ and $\sqrt{w'w'}$ are smaller than those of experiment especially near the wall. This causes a slight increase of velocity profile in log-region as shown in Fig.1.

Plate.1 shows the $sign(v')(u'v') = \pm 3$ surfaces. We can see the streaky structure of wall bounded turbulence. Streaks are stretched obliquely from the wall. In the photo, white and gray streaks make a pair. A longitudinal vortex line exists between two streaks. This is a well known property of the wall bounded turbulence and hence this results agree quantitatively with the results already obtained by many other researchers. So, although we have to need refinement in the turbulence model, we think that the present code would work so long as we discuss a qualitative prospect for the effect of LEBU on turbulent flows.

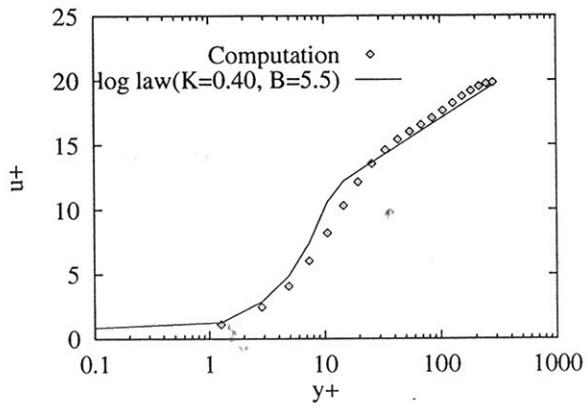

Fig.1 Logplot Profile of Mean Velocity

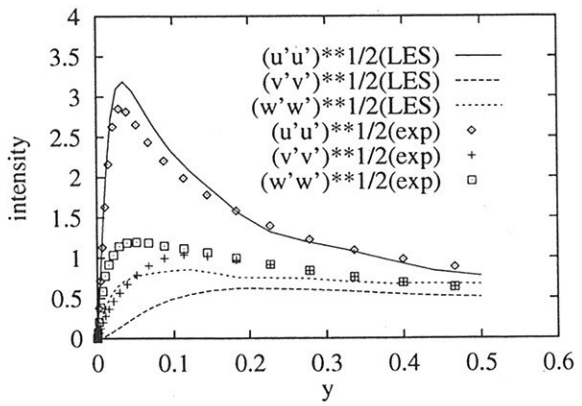

Fig.2 Turbulence Intencities in Channel Flow

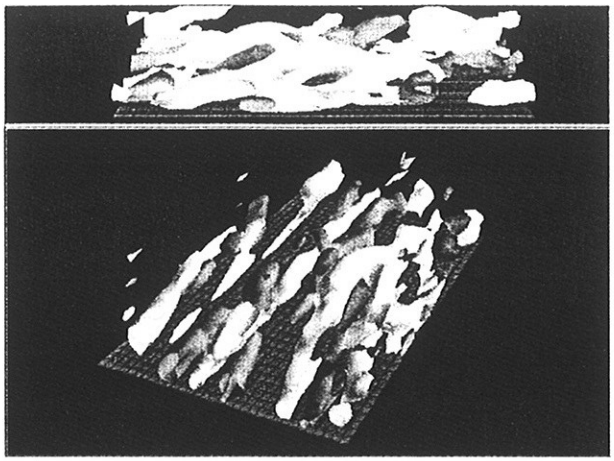

Plate.1 Streak structure of wall turbulence

5. Computation of Flow around a LEBU (LEBU in Periodic Channel Flow)

Here we model the LEBU as a flat plate of zero thickness and it is set in a periodic channel flow. Therefore in this model, an infinite number of LEBUs are placed equi-distantly in a row. The longitudinal length of the computational domain is set to 10 and channel width is set to 1. The length of the LEBU is 1 and it is located at $y = 0.25$, 25% of the channel width away from the wall.

Flow domain is gridded with $(101 \times 51 \times 31)$ mesh nodes. 21 and 31 points are used for dividing the lower and upper LEBU domains in the y direction, respectively. In the LEBU part, 10 equi-spaced cells are used in the x-directon. Periodic boundary conditions are used in the longitudinal and spanwise directions. A pressure gradient of -2 is imposed to keep the flow quasi-steady and the Reynolds numbr is set to 500, as in the previous channel flow. Δt is set to 0.0002.

6. Results of LEBU Flow Simulation

Figs. 3 and 4 show the change of mean velocity profiles and turbulence energy profiles along the channel. Here the LEBU is located at $-0.5 \leq x \leq 0.5$. The baseline of each curve is shifted by 1 for easy observation. Velocity deficit along the LEBU line is seen. This means that the LEBU effect remains until the next downstream LEBU and consequently, the LEBU row has a blockage effect on the channel flow. From this, the length of the present computational domain may not be sufficient to investigate the effect of a single LEBU upon the turbulent flow. The turbulence energy at the wall beneath the LEBU is strengthened and strong turbulence energy is generated at the LEBU but they are weakend as the flow goes downstream.

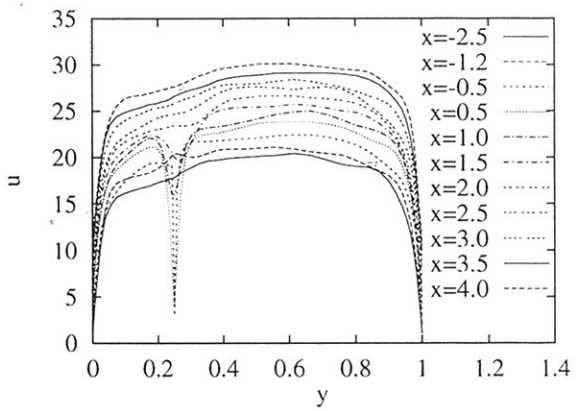

Fig.3 Change of mean velocity profile along channel

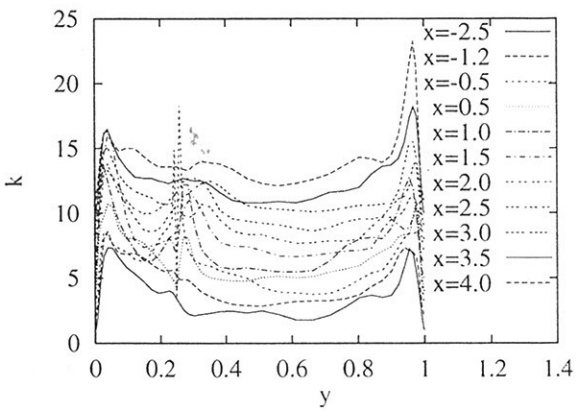

Fig.4 Change of Turbulence Energy along Channel

To investigate more deeply, we show the longitudinal vorticity distribution and pressure distribution in Figs. 5 and 6. They are both averaged in the spanwise direction. The vertical lines in the figures show the position of the LEBU.

Fig.5 Spanwise averaged longitudinal vortices

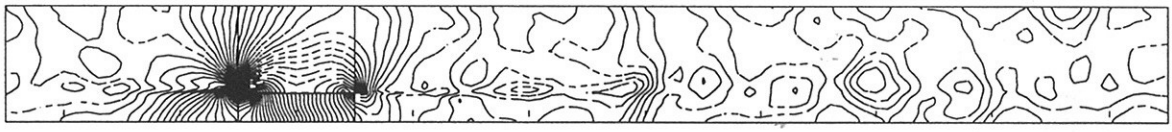

Fig.6 spanwise averaged pressure without constant pressure gradient

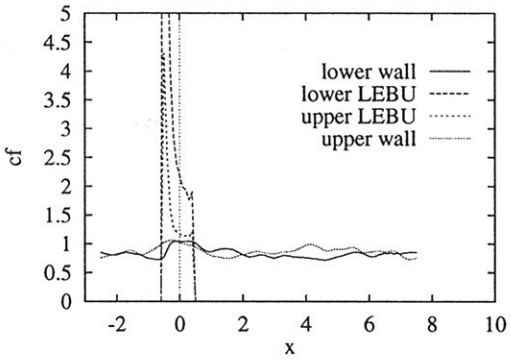

Fig.7 Distribution of spanwise averaged friction, 100-timestep averaged

The streaky structure of the wall turbulent boundary layer remains along the upper wall, on the other hand, along the lower wall, large structural vortices distribution is broken by the LEBU. The weakened streaks on the lower wall are still observed but they are pressed down toward the wall. This may weaken the turblence energy at the lower wall, as shown in Fig.5. From the pressure distibution, even the thickless LEBU plays a role in blocking the flow. This is due to the displacement effect of the LEBU boundary layer. Finally, we show the skin friction distribution along the wall. They have been averaged over 100-timestep. As the LEBU is approached the friction increases in both the upper and lower channel all, but reduces with distance downstream. The reduction rate of the frictional force, corresponding to the gradient of the cf line, is slightly greater on the lower wall than on the LEBU-away wall and spans about 5 LEBU units.

By integrating the skin friction, We can evaluate the rate of drag for each part, lower wall, upper wall and the LEBU. Then, we get $D_{lowerwall}/D_{upperwall} = 0.953$, $D_{LEBU}/D_{upperwall} = 0.637$. Since we can regard the upper wall as a LEBU-free wall, the sum of $(D_{LEBU} + D_{lowerwall})/D_{upperwall}$ can be considered the total drag ratio. Unfortunately this value is 1.59 and the net drag reduction can not be obtained. In the present model, the length of LEBU may be too long as a drag redction device. We need further simulations with different LEBU size and location and also a case that a single LEBU is located in a fully developed turbulent boundary layer is necessary. They remain as future works.

References

[1] M.Germano,U et al., Phys. Fluids. A3(7), July, (1991)

[2] D.K.Lilly, Phys. Fluids A4(3) March 1992

[3] N. Taniguchi et al., 9-th NST Sympo. IIS, Univ. Tokyo, (in Japanese) March (1994)

[4] H-P.Kreplin et al., Phys. Fluids 22(7) July (1979)

(Abstract for the Numerical Towing Tank Symposium, September 1998)

Diffraction Wave of a Blunt Ship at Forward Speed in Ballast-Load Condition

Hidetsugu IWASHITA
Engineering Systems, Hiroshima University
Kagamiyama 1-4-1, Higashi-Hiroshima 739, JAPAN

Introduction

Nowadays, the focus of the seakeeping computations is changing from the ordinal prediction of the global forces and/or ship motions to more accurate prediction of the local wave field represented by the wave pressure acting on a ship, for the purpose of the global structral analysis based on FEM. *Iwashita et al. (1991)* systematically investigated about the wave pressure distribution of a blunt VLCC advancing in oblique short waves and showed its negligible discrepancies between experiments and theoretical computations based on the linear theory. Consecutively the importance of the influence of the steady flow in seakeeping computations including wave pressure estimation had been studied by *Iwashita et al. (1994)*, *Iwashita & Bertram (1997)* and *Iwashita (1998)*. It has been made clear up to now that the estimation accuracy of the wave pressure is improved in some quantity by taking into account the influence of the steady flow in both the free-surface and body surface conditions. More accurate estimation may be expected only by fully capturing the steady Kelvin-wave field in the free-surface and body surface conditions and this still remains as a future work.

This paper presents another experimental and numerical example on a local wave field which shows the insufficiency of the theoretical prediction and suggests urgent settlement for the practical aspect of the theory. The diffraction wave around the bow part of a blunt ship advancing in head waves is predicted by a typical RPM and its results are compared with experiments. The significant discrepancy between two results are discussed relating it to the discrepancy on the wave pressure.

Formulation

We consider a ship advancing at constant forward speed U in oblique regular waves encountered at angle χ, Fig.1. The ship motion is restricted at its equilibrium position and the wave amplitude A of the incident wave is assumed to be small. ω_0 is the circular frequency and K the wave number of the incident wave. The encounter circular frequency is $\omega_e (= \omega_0 - KU\cos\chi)$. The linear theory is employed for this problem assuming ideal (potential) flow.

The velocity potential Ψ governed by Laplace's equation can be expressed as

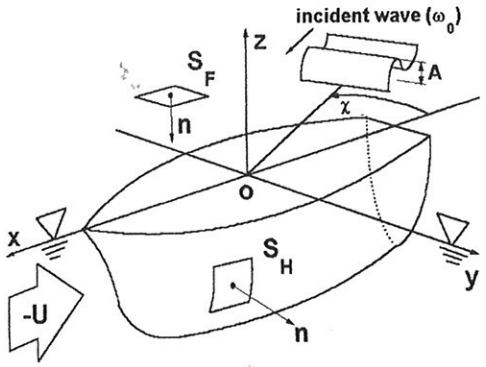

Fig. 1 Coordinate system

$$\Psi(x,y,z;t) = U[\Phi(x,y,z) + \varphi(x,y,z)] + \Re[\phi(x,y,z)e^{i\omega_e t}] \tag{1}$$

where

$$\phi = \frac{gA}{\omega_0}(\phi_0 + \phi_7), \quad \phi_0 = ie^{Kz - iK(x\cos\chi + y\sin\chi)} \tag{2}$$

Φ means the double-body flow, φ the steady wave field and ϕ the unsteady wave field. Assuming small disturbance due to the ship, we can linearize the free-surface conditions for φ and ϕ in several

forms. In this paper we adopted the following free-surface conditions derived by *Yasukawa (1990)* and corresponding body boundary conditions. For φ it becomes

$$\frac{1}{2K_0}\overline{\nabla}\Phi\cdot\overline{\nabla}(\overline{\nabla}\Phi\cdot\overline{\nabla}\Phi)+\frac{1}{K_0}\overline{\nabla}\Phi\cdot\overline{\nabla}(\overline{\nabla}\Phi\cdot\overline{\nabla}\varphi)+\frac{1}{2K_0}\overline{\nabla}(\overline{\nabla}\Phi\cdot\overline{\nabla}\Phi)\cdot\overline{\nabla}\varphi+\frac{\partial\varphi}{\partial z}=0 \quad \text{on } z=0 \tag{3}$$

$$\frac{\partial\varphi}{\partial n}=0 \quad \text{on } S_H \tag{4}$$

and for ϕ_7

$$-K_e\phi_7+2i\tau\overline{\nabla}\Phi\cdot\overline{\nabla}\phi_7+\frac{1}{K_0}\overline{\nabla}\Phi\cdot\overline{\nabla}(\overline{\nabla}\Phi\cdot\overline{\nabla}\phi_7)+\frac{1}{2K_0}\overline{\nabla}(\overline{\nabla}\Phi\cdot\overline{\nabla}\Phi)\cdot\overline{\nabla}\phi_7+\frac{\partial\phi_7}{\partial z}=0 \quad \text{on } z=0 \tag{5}$$

$$\frac{\partial\phi_7}{\partial n}=-\frac{\partial\phi_0}{\partial n} \quad \text{on } S_H \tag{6}$$

where $\boldsymbol{V}=\nabla\Phi$, $K_0=g/U^2$, $K_e=\omega_e^2/g$, $\tau=U\omega_e/g$ and $\overline{\nabla}$ is defined as a two-dimensional Laplacian with respect to x and y on the free surface. Eq.(3) coincides with the *Dawson's (1977)* free-surface condition in the steady problem and eq.(5) is a corresponding form in the unsteady problem.

If we put $\Phi=-x$, $\partial\varphi/\partial n=n_x$ and $\boldsymbol{V}=\nabla[-x+\varphi]$, the formulation (3) $\sim$ (6) leads to the Neumann-Kelvin formulation.

The diffraction wave $\Re[\zeta_7\, e^{i\omega_e t}]$ is calculated by using the diffraction potential ϕ_7 and its derivatives as follows:

$$\zeta_7(x,y)=-i\frac{\tau}{\nu}\Big(1+\frac{1}{iK_0\tau}\boldsymbol{V}\cdot\overline{\nabla}\Big)\phi_7 \qquad \text{on } z=0 \tag{7}$$

where $\nu=U\omega_0/g$.

Numerical methods

The RPM applied in this study is a collocation method developed by *Jensen et al. (1986)* and *Ando et al. (1988)* for the steady problem and extended to the unsteady problem by *Bertram (1990)*. The radiation condition is satisfied by shifting the collocation point one panel upward on the free surface. Recently *Eguchi (1995)* and *Nakatake et al. (1995)* proposed its extended computation method which is quite robust and stable even for the blunt ship in the steady problem. We solve our problem applying this method to the unsteady problem.

The steady and unsteady potentials, φ and ϕ_7, are both expressed by the source distributions on the body surface S_H and the free surface S_F as follows:

$$\left.\begin{matrix}\varphi(P)\\ \phi_7(P)\end{matrix}\right\}=-\iint_{S_H+S_F}\left\{\begin{matrix}\sigma_s(Q)\\ \sigma_7(Q)\end{matrix}\right\}G(P,Q)\,dS \tag{8}$$

where

$$G(P,Q)=\begin{cases}(1/r+1/r')/4\pi & \text{for } Q \text{ on } S_H\\ 1/4\pi r & \text{for } Q \text{ on } S_F\end{cases},\qquad \left.\begin{matrix}r\\ r'\end{matrix}\right\}=\sqrt{(x-x')^2+(y-y')^2+(z\mp z')^2}$$

The body surface and the free-surface are discretized into the finite number of constant panels, and numerical solutions for steady and unsteady problems are obtained such that a corresponding set of the free-surface condition and the body boundary condition are satisfied at collocation points. The collocation points on S_H coincides with the geometric center of each panel and those on S_F are shifted one panel upward in order to force the radiation condition numerically. This numerical radiation condition is valid only for $\tau>1/4$ in the unsteady problem where the waves do not propagate to the forward direction of the ship. Fig. 2 illustrates typical computation grids on S_H and S_F. For the panels inside the waterline on S_F, source distributions are forced to be zero, or those panels are totally removed from the computation domain, *Eguchi (1995)* and *Nakatake et al. (1995)*.

Results

Numerical computations are performed for a Series-60 model of $C_b = 0.8$. Both the ballast-load condition and the full-load condition are computed based on the doubl-body formulation and the Neumann-Kelvin formulation described above. Numerical results are compared with corresponding experiments presented by *Ohkusu & Wen (1996)* only for the ballst-load condition. Fig. 2 shows the hull form and the computation grids for the Series-60 model in the ballast-load condition ($C_b = 0.8$, $B/d = 5.9412$).

Fig.3 shows the diffraction waves along the transvers line at ordinate 9, 8, 7 and 6. Notwithstanding the double-body formulation seems to improve the computation results slightly, the remarkable discrepancy between computed and measured results can be still observed especially near the bow part and it decreases as the distance from the bow increases. At ordinate 9, the computed result underestimates the experiment about 50 % in magunitude and this result consistent with the result that we have obtained for the wave pressure, *Iwashita et al. (1993, 1994)*. The significant influence of the steady Kelvin-wave field in the free surface condition, which is not taken into account in any formulations presented here, is considered as a cause.

References

ANDO, J., NAKATAKE K. (1988), *A Method to Calculate Wave Flow by Rankine Source*, Transactions of The West-Japan Soc. of Naval Arch. No. 75 (in Japanese)

BERTRAM, V. (1990), *Fulfilling Open-Boundary and Radiation Condition in Free-Surface Problems Using Rankine Sources*, Ship Technology Research, Vol. 37/2

EGUCHI, T. (1995), *Numerical Analysis of Rankine Source Collocation Method for the Steady Wave Making Resistance Problem*, J. Soc. Naval Arch. Japan 177 (in Japanese)

DAWSON, C. W. (1977), *A Practical Computer Method for Solving Ship Wave Problems*, 2nd Int. Conf. on Numerical Ship Hydrodynamics, Berkeley

IWASHITA, H., ITO, A., OKADA, T., OHKUSU, M., TAKAKI, M., MIZOGUCHI, S. (1993), *Wave Forces Acting on a Blunt Ship with Forward Speed in Oblique Sea (2rd Report)*, J. Soc. Naval Arch. Japan 173 (in Japanese)

IWASHITA, H., ITO, A., OKADA, T., OHKUSU, M., TAKAKI, M., MIZOGUCHI, S. (1994), *Wave Forces Acting on a Blunt Ship with Forward Speed in Oblique Sea (3rd Report)*, J. Soc. Naval Arch. Japan 176 (in Japanese)

IWASHITA, H., BERTRAM, V. (1997), *Numerical Study on the Influence of the Steady Flow in Seakeeping*, 12th WWWFB, Marseille

IWASHITA, H. (1998), *Influence of the Steady Flow in Seakeeping of a Blunt Ship through the Free Surface Condition*, 13th WWWFB, The Netherlands

JENSEN, G., MI, Z.-X., SÖDING, H. (1986), *Rankine Source Methods for Numerical Solutions of the Steady Wave Resistance Problem*, 16th Symp. on Nav. Hydrodyn., Berkeley

NAKATAKE K., ANDO, J. (1995), *A Method to Calculate Wave Flow around a Wide Ship*, Transactions of The West-Japan Soc. of Naval Arch. No. 90(in japanese)

OHKUSU, M., WEN, G. C. (1996), *Radiation and Diffraction Waves of a Ship at Forward Speed*, Proc. 21st Symp. Naval Hydro. Trondheim

YASUKAWA, H. (1990), *A Rankine Panel Method to Calculate Unsteady Ship Hydrodynamic Forces*, J. Soc. Naval Arch. Japan 168

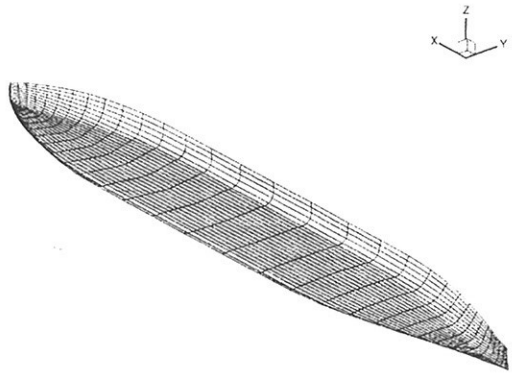

(a) Hull form and computation grids
($N_H = 448$ on half)

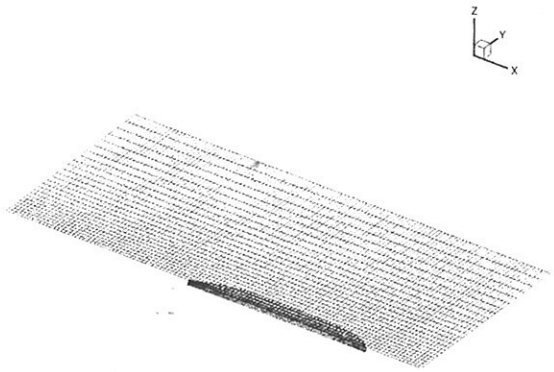

(b) Computation grids ($N_H = 448$, $N_F = 2683$)

Fig. 2 Series-60 model in ballast-load condition ($C_b = 0.8$, $B/d = 5.9412$)

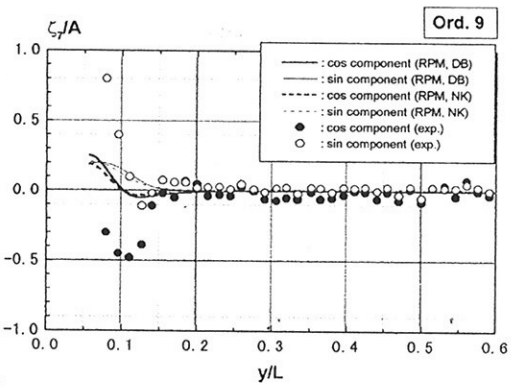

(a) Ord. 9

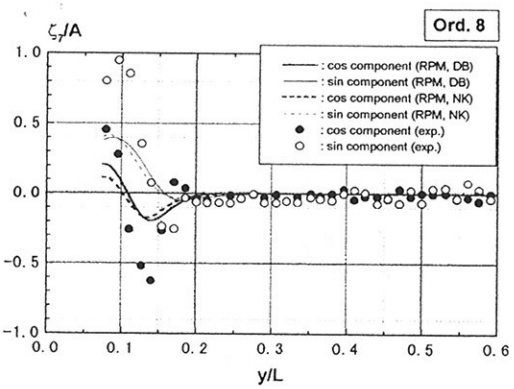

(b) Ord. 8

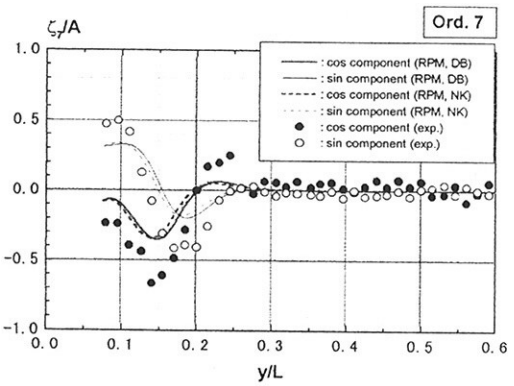

(c) Ord. 7

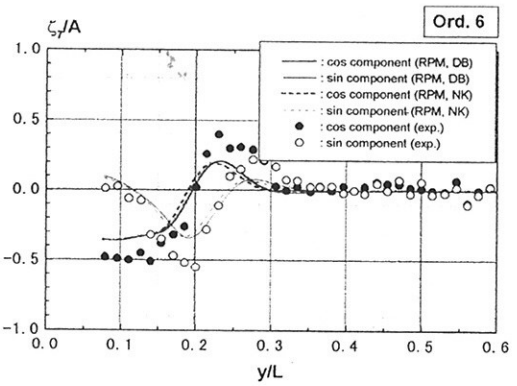

(d) Ord. 6

Fig. 3 Diffraction wave distributions along transvers line in ballast-load condition ($B/d = 5.9412$)

LES of a flow past a surface piercing circular cylinder

Takafumi Kawamura*

1 Introduction

The interaction of turbulent flows with a free surface and surface waves is a very intriguing problem in fluid dynamics, and has also been a subject of active research recently. This subject has been investigated with respect to open chanel flow, free-surface jet flows, juncture of free-surface and boundary layer or wake, and so on. However, most of previous studies deal with cases with negligible free-surface deformations, and effects of surface waves have not been extensively investigated. In this study, we investigate strong interactions between a turbulent shear flow and large amplitude nonlinear surface waves about a piercing circular cylinder in a steady current by large eddy simulation (LES).

This physical problem has been studied by Inoue et al.[1] experimentally, and their results suggest that a strong interaction exists between highly nonlinear surface waves and the separated vortical flow behind the cylinder. Strong vertical surface fluctuations were observed near the stern in the experiment at the Froude number of 0.8, and the periodic vortex shedding was suppressed near the free surface presumably due to the interaction with surface waves. Velocity measurements suggest that the fluctuation is dominated by the quasi-periodic vortex-shedding in the deeper two-dimensional flow region, but it is dominated by higher frequency, and more stochastic motions near the free surface. The objective of this study is to provide a better understanding of this complex flow by applying LES.

2 Numerical method

2.1 Governing equation and computational procedure

The governing equations are the grid-filtered incompressible Navier-Stokes equations. All the quantities are nondimensionalised with respect to the diameter of the cylinder D and the uniform velocity U_0. The origin of the coordinate system is the centre line of the cylinder at the still water level. The x_1, x_2 and x_3-axes are taken in the direction of the uniform flow, in the spanwise direction and in the vertical direction upward, respectively.

The numerical method developed at ICCH is used for the computations presented in this study. The details of the method and validations are found in Ref. [3, 2]. This finite volume code solves the grid-filtered Navier-Stokes equations discretised on general curvilinear grid based on a partial transformation, where the Cartesian velocity components, pressure and turbulence quantities defined at cell centres are the dependent variables. A second order central interpolation is used for calculating fluxes except for convective flux for which the second order QUICK scheme is used.

Time integration is performed by a second-order fractional step method. First in the predictor step, the intermediate velocity at cell centre is computed by integrating the momentum equations using a second order semi-implicit scheme, and the continuity equation is implemented in the corrector step.

*International Research Centre for Computational Hydrodynamics (ICCH), Denmark

The Smagorinsky model is used to model the SGS stress in this study. The SGS stress is given by

$$\tau_{ij} = -2\nu_T S_{ij} = -2(C_s\Delta)^2\sqrt{2S_{ij}S_{ij}}S_{ij}, \tag{1}$$

where ν_T, S_{ij}, C_s and Δ are the eddy viscosity, the strain rate tensor, the model coefficient and the cubic root of the volume of the cell, respectively.

The computational mesh is fitted to the free surface and updated every time step by moving grid points in the vertical direction following the free surface movement expressed by

$$\frac{\partial h}{\partial t} + u_1\frac{\partial h}{\partial x_1} + u_2\frac{\partial h}{\partial x_2} = u_3, \tag{2}$$

where h is the height of the free surface from the still water level and u_i is the Cartesian velocity component. The volume flux due to this movement of grid is taken into account in the momentum equation.

2.2 Boundary conditions

Computational domain is discretised using O-H-type mesh. The boundary of the computational domain consist of free surface, body surface, bottom, inflow and outflow. Assuming that the surface tension and viscous stress of air are negligible, the dynamic free surface condition is given by

$$(2\nu S_{ij} - p\delta_{ij})\, n_j = 0, \tag{3}$$

where ν is the kinematic viscosity, δ_{ij} is the Kronecker delta, and n_j is the unit normal vector of the free surface. On the body surface, no-slip condition is imposed and surface elevation is linearly extrapolated, while a symmetry condition is applied at the bottom boundary. At the inflow boundary, the velocity components are fixed at the free-stream value and a homogeneous Neumann condition is applied to the pressure. At the outflow, the velocity components are extrapolated and pressure is kept at zero. An artificial damping function is applied to the surface elevation near the boundary, and it is damped to zero before reaching the outer boundary.

3 Numerical simulation

The grid system used for the simulation is shown in Figure 1. The number of mesh points is 128×64×16 in the tangential, radial and vertical directions respectively. This number is set according to convergence studies carried out using finer and coarser grids. A deep draft is assumed in the present case and the depth of the domain is set to 4, which is deep enough according to the experiment. The distance from the centre of the cylinder to the outer boundary ranges from 10 to 15. The Froude number and the Reynolds numbers are set to the values in the experiment, which are 0.8 and 2.7×10^4 respectively. The flow initially at rest is gradually accelerated using 10 time units, while the time increment is 0.005.

Computed and measured mean surface elevation contours are shown in Figure 2. The LES computation agrees well with the measurement, especially the flat region behind the cylinder is very well captured. The root mean square of the computed and measured vertical fluctuations of the free surface are compared in Figure 3. The LES result agrees very well with the measurement. The peak position and intensity are very accurately computed. The location of high intensity fluctuation corresponds to an edge of the flat region found in the

mean surface elevation contour Figure 2. This corresponds to the description of Inoue et al.[1] that the surface fluctuation starts where the gradient of the free surface vanishes.

Figure 4 shows a time history of the streamwise velocity at one point in the wake at three depths $x_3 = -0.6$, $x_3 = -1.0$, and $x_3 = -4.0$. The velocity fluctuations are dominated by periodic vortex-shedding at $x_3 = -4.0$, where the mean flow is almost two-dimensional. At one diameter deep ($x_3 = -1.0$), the amplitude of the fluctuation becomes very small. However, the character of the fluctuation changes drastically at $x_3 = -0.6$, where the fluctuation is more random than in the deep two-dimensional flow region. The interaction between surface waves and the separated vortical flow is more apparent in Figure 5 showing an instantaneous field of computed vertical vorticity component on the free surface and on the bottom free-slip plane. A vortex-shedding is clearly observed near the bottom plane where the flow is almost two-dimensional, however it is much less dominant on the free surface. It is supposed that the wake-wave interaction enlarges the distance between the two separated layers towards the downstream direction suppressing the vortex-shedding.

4 Conclusions

Turbulent flow around a surface piercing circular cylinder at $Fn = 0.8$ has been investigated by LES. The results have been validated through comparisons with data for the mean surface elevation and vertical fluctuation of the free surface.

A complex flow pattern resulting from the wave-wake interaction is elucidated by the computation. It is shown that the quasi-periodical vortex-shedding is suppressed near the free surface due to the three-dimensional flow pattern near the surface resulting from surface wave generation. It is also shown that the character of the velocity fluctuation in the wake varies drastically in the vertical direction toward the free surface. In the deeper region the fluctuation is dominated by periodical vortex-shedding, while at a depth of one diameter, the amplitude of the fluctuation is found to be very small, presumably due to the suppression of vortex-shedding mentioned above. However, more random and intensive high frequency fluctuation is observed near the free surface. These features are found both in the LES and in the experiment, showing that LES is capable of simulating such free-surface induced fluctuations.

Acknowledgement

This work was financed by the Danish National Research Foundation. Their financial support is greatly appreciated.

References

[1] M. Inoue, N. Baba, and Y. Himeno. Experimental and numerical study of viscous flow field around an advancing vertical circular cylinder piercing a free-surface. *J. Kansai Soc. Naval Archit. of Japan*, 220:57–64, 1993.

[2] T. Kawamura. *Numerical simulation of 3D turbulent free-surface flows.* PhD thesis, Department of Naval Architecture and Ocean Engineering, School of Engineering, University of Tokyo, 1998.

[3] S. Mayer, A. Garapon, and L. Sørensen. A fractional step method for unsteady free surface flow with applications to non-linear wave dynamics. *to appear in Int. J. Num. Meth. Fluids*, 1998.

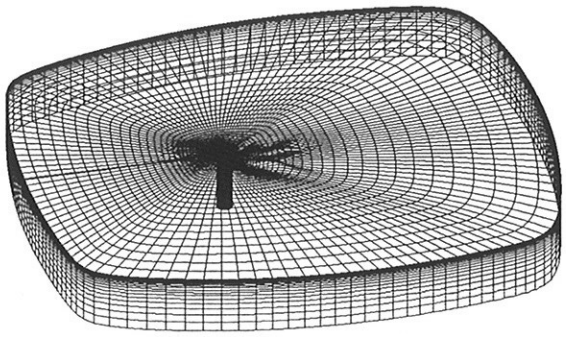

Figure 1: Grid system.

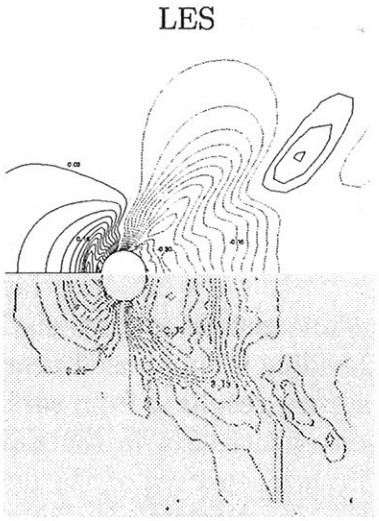

Measurement

Figure 2: Mean surface elevation.

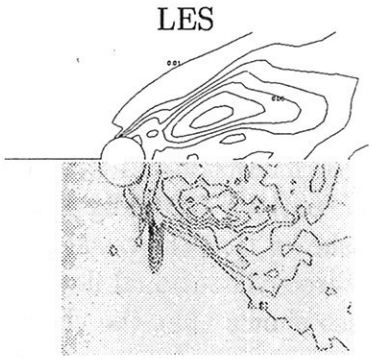

Measurement

Figure 3: RMS of the vertical fluctuation of the surface.

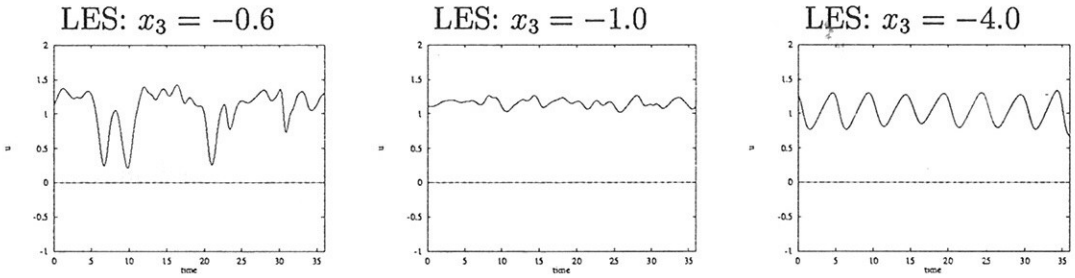

Figure 4: Time history of the streamwise velocity component at $(x_1, x_2) = (2, 1)$. The time axis shows relative time.

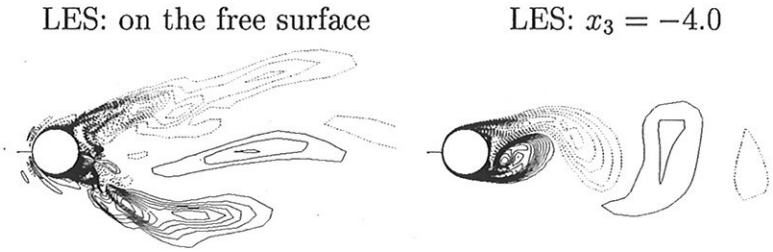

Figure 5: Comparison of the instantaneous vertical component of vorticity $\bar{\omega}_3$. Contour interval is 0.4.

PREDICTIONS OF MULTICOMPONENT FREE-SURFACE FLOWS

S. Muzaferija and M. Perić
Technische Universität Hamburg - Harburg,
Arbeitsbereich Fluiddynamik und Schiffstheorie,
Lämmersieth 90, D-22305 Hamburg, Germany

INTRODUCTION

Problems which involve a number of immiscible fluids are not rear in everyday life. Examples relevant for marine environmental technology are oil spills, sloshing of oil and water in a damaged tank or intrusion of saline into sweet water which happens at a river mouth. Numerical predictions of these problems are potentially very interesting. They can help us to gain better understanding of a problem and to test the efficiency of our possible solutions.

The free-surface capturing method presented in [1] is similar to those presented by Lafaurie at al. [2] and Ubbink [3] and has been used until now for free-surface flows which involve two fluids only [4-6]. The method can successfully be applied to problems where the free surface changes its topology due to wave breaking, overturning or splashing. In this sense, the method has a clear advantage over interface-capturing methods [7]. Furthermore, as it will be shown in this paper, the method can be extended to deal with flows which involve a number of immiscible fluids.

MATHEMATICAL MODEL

The conservation equations of mass, volume concentrations and momentum describe the behavior of a multi-fluid system:

$$\frac{\mathrm{d}}{\mathrm{d}t}\int_V \rho \,\mathrm{d}V + \int_S \rho \mathbf{v}\cdot\mathbf{n}\,\mathrm{d}S = 0\,, \tag{1}$$

$$\frac{\mathrm{d}}{\mathrm{d}t}\int_V c_i \,\mathrm{d}V + \int_S c_i \mathbf{v}\cdot\mathbf{n}\,\mathrm{d}S = 0\,, \tag{2}$$

$$\frac{\mathrm{d}}{\mathrm{d}t}\int_V \rho\mathbf{v} \,\mathrm{d}V + \int_S \rho\mathbf{v}\mathbf{v}\cdot\mathbf{n}\,\mathrm{d}S = \int_S \boldsymbol{T}\cdot\mathbf{n}\,\mathrm{d}S + \int_V \mathbf{f}_\mathrm{b}\,\mathrm{d}V. \tag{3}$$

Here, V is an arbitrary control volume bounded by a closed surface S, ρ is the density, $\mathbf{v}$ is the fluid velocity vector, $\mathbf{n}$ is the unit vector normal to the surface S and directed outwards, c_i is the volume concentration of the ith fluid component, $\boldsymbol{T}$ is the stress tensor, and $\mathbf{f}_\mathrm{b}$ is the resultant body force.

The mixture of fluids is treated as a single effective fluid, whose physical properties can be expressed as a function of the volume concentrations and the physical properties of each fluid component:

$$\rho = \sum_i c_i\rho_i\ ; \quad \mu = \sum_i c_i\mu_i\ ; \quad \sum_i c_i = 1 \tag{4}$$

where ρ_i and μ_i are the density and dynamic viscosity of the ith fluid component, respectively.

One should notice that the mathematical formulation of the problem is not limited to any specific number of fluids.

NUMERICAL METHOD

In order to solve the governing equations, the solution domain is first subdivided into an arbitrary number of contiguous control volumes (CVs) or cells. Control volumes can be of an arbitrary polyhedral shape allowing for local grid refinement, sliding grids, and grids with non-matching block interfaces. More details about this finite-volume FV discretization can be found in [8]. Here only the interface-capturing features of the method will be presented.

A successful scheme for interface capturing must exploit the interface sharpening nature of the downwind scheme, it must prevent over- and underflow of cells (it has to be bounded), and it should have a mechanism to avoid alignment of the interface with the numerical grid. The High Resolution Interface Capturing (HRIC) scheme [1] achives this by a non-linear blend of the upwind (UD) and the downwind (DD) scheme. The UD scheme approximates the cell-face value by the value at the upstream cell center (Fig. 1). It is unconditionally stable and always produces a bounded solution. On the other hand, the DD scheme is an unconditionally unstable scheme that introduces negative numerical diffusion. It approximates the cell-face value by the value at the downstream cell center. The way of blending UD and DD can be analyzed in the Normalized Variable Diagram (NVD) [9]. The local normalized volume fraction $\tilde{c}$ in the vicinity of the cell center C is defined as follows:

$$\tilde{c}(\mathbf{r}) = \frac{c(\mathbf{r},t) - c_{\mathrm{U}}}{c_{\mathrm{D}} - c_{\mathrm{U}}} , \tag{5}$$

where subscripts U and D denote the respective nodes upstream and downstream of the cell center C, and $\mathbf{r}$ is the position vector. The HRIC scheme computes the cell-face value of the normalized volume fraction according to the following expression (Fig. 2):

$$\tilde{c}_{\mathrm{j}} = \begin{cases} \tilde{c}_{\mathrm{C}} & \text{if} \quad \tilde{c}_{\mathrm{C}} < 0 \\ 2\tilde{c}_{\mathrm{C}} & \text{if} \quad 0 \leq \tilde{c}_{\mathrm{C}} < 0.5 \\ 1 & \text{if} \quad 0.5 \leq \tilde{c}_{\mathrm{C}} < 1 \\ \tilde{c}_{\mathrm{C}} & \text{if} \quad 1 \leq \tilde{c}_{\mathrm{C}} \end{cases} \tag{6}$$

In order to prevent an alignment of the interface with the numerical grid because of the use of the downwind discretization [2] , the HRIC scheme corrects the $\tilde{c}_{\mathrm{j}}$ value according to the following expression:

$$\tilde{c}^{*}_{\mathrm{j}} = \tilde{c}_{\mathrm{j}}\sqrt{\cos\theta} + \tilde{c}_{\mathrm{C}}(1 - \sqrt{\cos\theta}) . \tag{7}$$

where θ is the angle between the normal to the interface (defined by the gradient of the volume fraction ∇c) and the normal to the cell face (Fig. 1).

The blending of upwind and downwind schemes is dynamic and accounts for the local distribution of the volume fraction. However, if the local Courant number Co is too large, the dynamic nature of the scheme may cause convergence problems. In order to prevent this, the HRIC discretization also takes into account the value of Courant number, yielding the cell-face value of the volume fraction according to the following expression:

$$\tilde{c}^{**}_{\mathrm{j}} = \begin{cases} \tilde{c}^{*}_{\mathrm{j}} & \text{if} \quad \mathrm{Co} < 0.3 \\ \tilde{c}_{\mathrm{C}} & \text{if} \quad 0.7 < \mathrm{Co} \\ \tilde{c}_{\mathrm{C}} + (\tilde{c}^{*}_{\mathrm{j}} - \tilde{c}_{\mathrm{C}})\frac{0.7-\mathrm{Co}}{0.7-0.3} & \text{otherwise} \end{cases} \tag{8}$$

Finally, the HRIC cell-face value of c is computed according to Eq.(5) as follows:

$$c^{\mathrm{HRIC}}_{\mathrm{j}} = \gamma\, c_{\mathrm{C}} + (1-\gamma)c_{\mathrm{D}} , \qquad \gamma = \frac{(1 - \tilde{c}^{**}_{\mathrm{j}})(c_{\mathrm{D}} - c_{\mathrm{U}})}{c_{\mathrm{D}} - c_{\mathrm{C}}} . \tag{9}$$

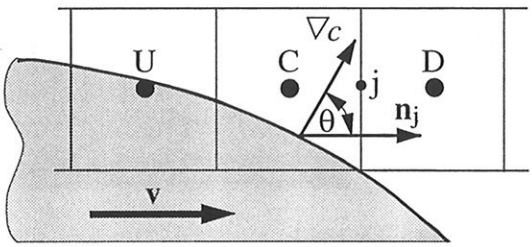

Figure 1: Notation and values used for NVD diagram and HRIC scheme.

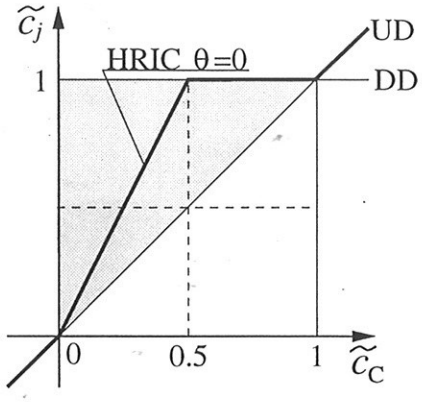

Figure 2: NVD diagram and the HRIC scheme.

EXAMPLES

The breaking-dam experiment of Koshizuka at al. [10] is a very atractive problem which one can use to demonstrate the qualitative behaviour of the method as well as its applicability to problems with breaking and overturning waves.

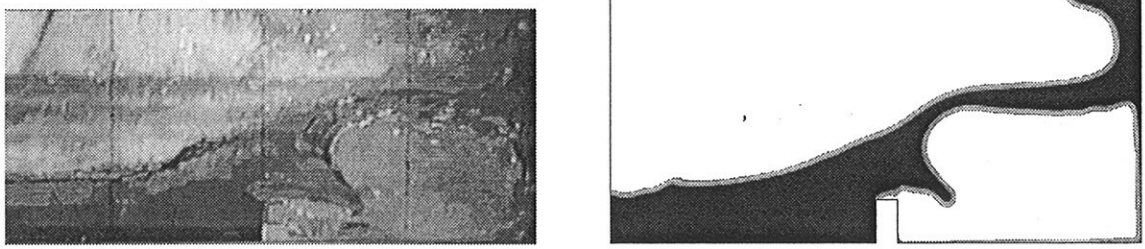

Figure 3: Comparison of experimental visualisation [10] and computation of the breaking-dam flow 0.5 seconds after one side wall is removed.

In this case it is important to consider the flow of both water and air, especially when air becomes trapped in water, as shown in Fig. 3. Water slides along an air cushion which due to large buoyancy force tends to rise up and to break up the water layer which sits on it. The predicted form of the free surface has all qualites of the free surface observed in the experiment.

Another example is sloshing in a quadratic tank, which involves four fluids of different density. The initial distribution of those four fluids is shown in Fig. 4.a. The fluid densities are 1, 250, 500, 750 and 1000 kg/m^3. The fluids are colored according to their densities; black is used for the haviest and white for the lightest fluid. Since the initial distribution of fluids cannot be preserved, they star moving. Figure 4.b shows an arrangement of fluids shortly after the begining of the simulation. The heviest fluid pushes others trying to reach the state of its minimum potential energy. After a wail all motions die out due to the work of the viscous forces, and the system reachs the state of its minimum potential energy, which is shown in Fig. 4.c.

SUMMARY

In this paper we have shown how the free-surface capturing method [1] can be used for simulation of multicomponent free-surface flows. The examples show good qualitative behaviour of the method when applied to multicomponent fluid flows. In the future, the method will

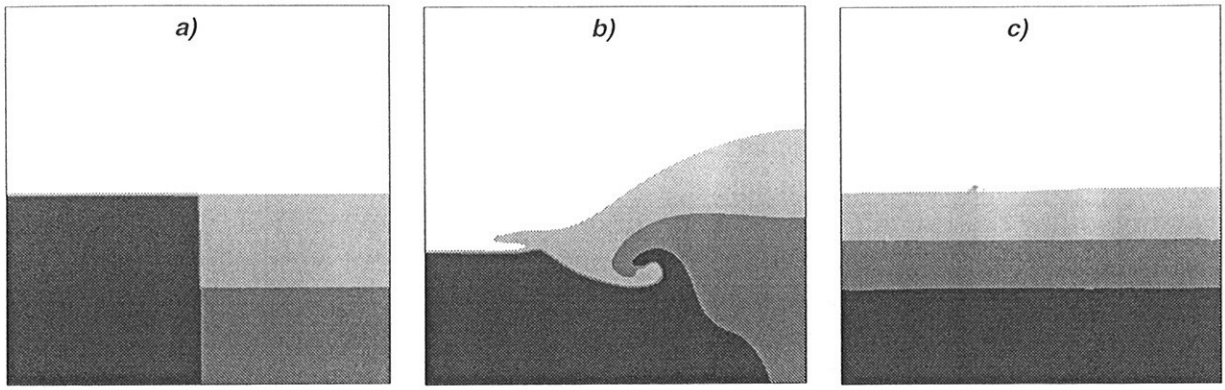

Figure 4: Sloshing of four fluids in a tank.

be tested for the praxis more relevant situations and problems for which quantitative validations are also possible.

References

1. S. Muzaferija, and M. Perić, "Computation of free surface flows using interface-tracking and interface-capturing methods", chap. 3 in O. Mahrenholtz and M. Markiewicz (eds.), *Nonlinear Water Wave Interaction*, Computational Mechanics Publications, Southampton, 1998.

2. B. Lafaurie, C. Nardone, R. Scardovelli, S. Zaleski, and G. Zanetti, "Modeling merging and fragmentation in multiphase flows with SURFER", *J. Comput. Phys.*, **113**, 134–147, (1994).

3. O. Ubbink, Numerical prediction of two fluid systems with sharp interfaces, PhD thesis, University of London, 1997.

4. P.C. Sames, T.E. Schellin, S. Muzaferija and M. Peric, "Application of a two-fluid finite volume method to ship slamming", *OMAE - Offshore Mechanics and Arctic Engineering* Lissabon, 1998.

5. R. Azcueta, S. Muzaferija and M. Perić, "Computation of water and air flow around ships", Procidings of *Euromech 374 - Recent Computational Developments in Steady and Unstady Naval Hydrodynamics* Poitiers, April 27-29, 1998.

6. S. Muzaferija, M. Perić, P.C. Sames and T.E. Schellin, "A two-fluid Navier-Stokes solver to simulate water entry", Procidings of *22nd Symposium on Naval Hydrodynamics*, Washington, D.C. - August 9-14, 1998.

7. S. Muzaferija, and M. Perić, "Computation of free-surface flows using finite volume method and moving grids", *Numer. Heat Transfer, Part B*, **32**, 369–384, (1997).

8. I. Demirdžić, S. Muzaferija and M. Perić, "Advances in computation of heat transfer, fluid flow, and solid body deformation using finite volume approaches", in W.J. Minkowycz, E.M. Sparrow (Editors), *Advances in Numerical Heat Transfer*, chap. 2, Taylor and Francis, New York, 1996.

9. B.P Leonard, "Bounded higher-order upwind multidimensional finite-volume convection-diffusion algorithms", in W.J. Minkowycz, E.M. Sparrow (eds.), *Advances in Numerical Heat Transfer*, chap. 1, pp. 1–57, Taylor and Francis, New York, 1996.

10. S. Koshizuka, H. Tamako and Y. Oka, "A particle method for incompressible viscous flow with fluid fragmentation, *Comput. Fluid Dynamics J.*, **4**, 29–46, (1995).

VISCOUS FLOW CALCULATIONS PAST A YACHT HULL

by

George D. Tzabiras

Department of Naval Architecture and Marine Engineering, National Technical University of Athens, Heroon Polytechniou 9, Zografou 157 73, Athens, Greece, e-mail tzab@naval.ntua.gr

Summary. The present work is concerned with the calculation of the turbulent flow-field around a yacht hull with a keel. The RANS equations are solved in two blocks and boundary conditions are exchanged between them until convergence is reached. The k-ε model is adopted to simulate turbulence and the solution algorithm follows the fundamental concepts of pressure-correction methods on staggered grids.

1. Introduction

The impressive development of CFD methods has grown to be an extremely valuable tool for designs in marine hydrodynamics. Among the problems which can be studied effectively by CFD is the influence of appendages on the flow structure around the hull. There are two general approaches that may be followed to perform computations in such complex domains. According to the first one, the calculation domain is divided in blocks and the numerical solution proceeds treating them either as a whole or separately by exchanging boundary conditions. In the second approach an unstructured grid configuration is employed to cover partly "difficult regions" or, alternatively, the whole calculation domain. Each method exhibits its own advantages and shortcomings with respect to accuracy and convergence, depending on the examined geometry. The aim of this work is to present the fundamental aspects of a two-block solution that has been developed to calculate the turbulent flow field around a yacht hull including an extended keel. The main objective of the method is to compute the total resistance of the body in order to study the sensitivity of results with regard to the size and the shape of the keel.

2. Grid Generation

The calculation domain around the complete configuration is divided in two blocks, the one surrounding the hull and the other surrounding the naked keel which has the shape of a three-dimensional swept wing. In both cases the computational grid is generated by applying the conformal mapping technique. The mesh around the hull consists of subsequent plane orthogonal curvilinear grids which are created by transforming the transverse sections onto the unit circle [1]. A similar C-type grid is generated around the keel where the wing sections are transformed on the unit circle following again a general conformal mapping approach, [2]. Characteristic grid sections of the combined blocks are shown in Fig. 1.

3. Governing Equations

The finite volume method has been employed to solve the transport equations which govern the steady, incompressible and turbulent flow past the examined vessel. In a local 3D orthogonal curvilinear system (x_i, x_j, x_l) with metrics (h_i, h_j, h_l) the u_i-Reynolds (or time-averaged Navier-Stokes) equation reads [1]:

$$\frac{\rho}{h_i h_j h_l}\left[\frac{\partial(h_j h_l u_i u_i)}{\partial x_i}+\frac{\partial(h_i h_l u_j u_i)}{\partial x_j}+\frac{\partial(h_i h_j u_l u_i)}{\partial x_l}\right]$$
$$=-\frac{1}{h_i}\frac{\partial p}{\partial x_i}+\rho u_j^2 K_{ji}+\rho u_l^2 K_{li}-\rho u_i u_j K_{ij}-\rho u_i u_l K_{il}+(\sigma_{ii}-\sigma_{jj})K_{ji}+$$
$$+(\sigma_{ii}-\sigma_{ll})K_{li}+\sigma_{ij}(2K_{ij}+K_{lj})+\sigma_{il}(2K_{il}+K_{jl})+$$
$$+\frac{1}{h_i}\frac{\partial \sigma_{ii}}{\partial x_i}+\frac{1}{h_j}\frac{\partial \sigma_{ij}}{\partial x_j}+\frac{1}{h_l}\frac{\partial \sigma_{il}}{\partial x_l} \qquad (1)$$

where u_i, u_j and u_l are the mean values of the velocity components and K_{ij} stands for the curvature tensor. The stress tensor components σ_{ij} are evaluated by employing the standard two-equation k-ε model. The differential equations (1) are integrated in control volumes corresponding to a staggered grid arrangement [1] and discretized following second order finite differences in space. The resulting algebraic equations comprise an elliptic system for each variable, while a hybrid scheme [3] is adopted to model the convective and diffusive terms.

4. The Solution Algorithm

An iterative procedure is followed to attain convergence in both blocks. A first solution is completed for the bare hull, i.e. neglecting the keel effects. To achieve fast convergence, the successive grid refinement technique described in [3] is combined with a parabolic solution of the discretized equations. In this block, the external boundaries are placed at an adequate distance from the body, so that Dirichlet-type conditions can be applied assuming that the flow is undisturbed. At the exit plane Neumman boundary conditions are applied for each variable, except the pressure which is extrapolated. The turbulence effects close to the body surface are taken into account by the wall function application [1].

Once convergence has been achieved in the first block, the values of variables on the external boundaries (B), Fig. 2, of the second block are calculated by linear interpolation. Evidently, the C-grid around the keel is located within the first block which is used to compute the flow past the hull. The solution in the second domain is obtained by combining a marching procedure with a fully elliptic one : the velocity components and the turbulence quantities are calculated as elliptic on wing sections while in the third direction a parabolic solution is followed, corresponding to a sweep of the domain. On the contrary, the pressure-correction equation is solved by a fully elliptic solver at the end of the aforementioned sweep. This treatment is necessary since the lateral velocity component (along the wing span) may take positive or negative values, according to the examined incidence, that influence strongly the convergence rate. At the exit plane of the domain under consideration non-reflecting conditions are adopted [4], while the wall functions are again employed near the solid surface.

When the solution is completed in the second block, boundary conditions are specified by linear interpolations on the surface (A), Fig. 3, which is located within the calculation domain. These values are adopted as internal Dirichlet conditions for the first block, i.e. no solution in the interior of (A) is performed. The solution proceeds again until convergence is achieved around the hull, etc, until the calculated total forces of the combined geometry remain practically constant.

5. A Test Case

A first application has been carried out for a yacht hull which has been tested experimentally in the towing tank of the Laboratory for Ship and Marine Hydrodynamics of NTUA. The waterline length of the model is 3.73 m and the span of the keel 0.80m. The latter has approximately the shape of a NACA 0018 section. Computations were performed for a symmetric case (i..e. zero incidence) at the low Froude number of 0.16 in order to reduce as far as possible the free surface effects. The corresponding Reynolds number was equal to 4.27×10^6. A grid of 60x60x180 nodes was used in the first block, where the first number denotes the nodes girthwise, the second normal to the body surface and the third is the number of transverse sections. With the same notation, a 238x20x40 grid was employed for calculations around the keel. In order to compare the calculated total resistance of the bare hull, experiments were carried out with and without the keel. In the first case, the computed total resistance of 0.387 Kp was quite close to the measured one of 0.370 Kp. Then, the described procedure was applied to calculate the effect of the keel. Convergence was achieved in 5 block-iterations and the computed resistance was found equal to 0.570Kp which is lower by almost 7% than the measured one. Apart from the numerical uncertainties, this discrepancy may partly be attributed to the end effects of the geometry of the real keel which were not taken into account in the calculations. In any case these results have been considered very encouraging and the research work is continued with applications of the method at various incidence angles .

Acknowledgments

The author wishes to acknowledge the significant support of the Hellenic Secretariat for Research and Technology for accomplishing the described work.

References

[1] G.D. Tzabiras, "A numerical study of the turbulent flow around the stern of ship models", Int. J. for Numerical Methods in Fluids, 9, November 1991, pp. 1179-1204

[2] G.D. Tzabiras, A. Dimas and T. A. Loukakis, "A numerical method for the calculation of incompressible, steady, separated flows around aerofoils", Int. J. for Numerical Methods in Fluids, 6, 1986, pp. 789-809

[3] G. D. Tzabiras, "Resistance and self propulsion numerical experiments on two tankers at model and full scale", Ship Techn. Research, 40, February 1993, pp. 20-38

[4] G.D. Tzabiras, "A numerical investigation of 2D, steady free surface flows", Int. J. for Numerical Methods in Fluids, 25, 1997, pp. 567-598.

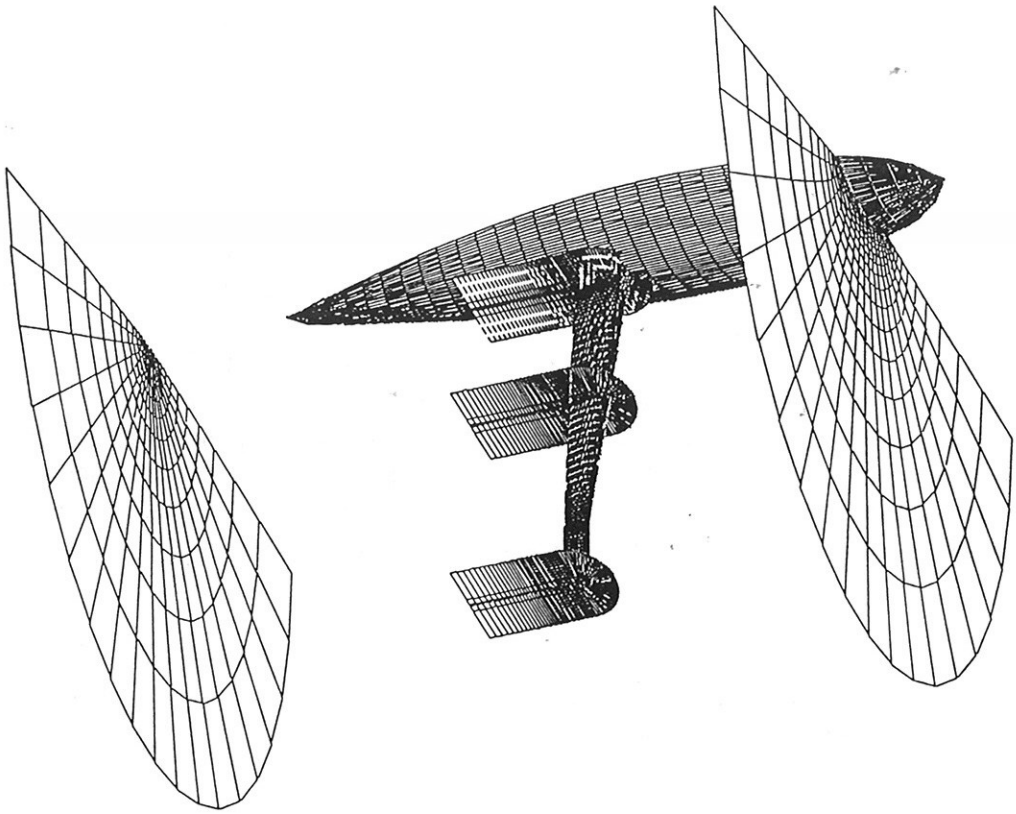

Figure 1. Characteristic grid surfaces around the complete configuration

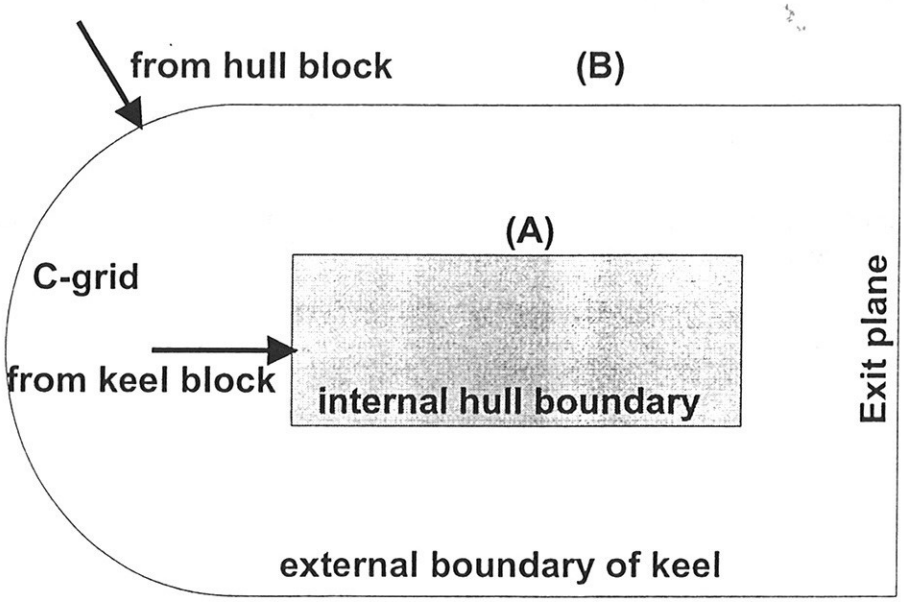

Figure 2. Exchange of boundary conditions between blocks

The level set technique applied to 2-d wave problems

Mathias Vogt and Lars Larsson

Abstract

A level set technique is used with a finite volume method to solve the incompressible Navier-Stokes equations for 2-dimensional free surface viscous flow simulations. Numerical parameters, such as air height, grid density and the width of the band where the physical properties change from air to water are systematically varied. The level set and the moving grid methods are compared for a bottom bump and a submerged NACA 0012 hydrofoil. Solitons generated by a bottom mound and the onset of breaking as function of submergence and speed of the hydrofoil are also predicted.

Level set method

A modern numerical algorithm for viscous flow to treat moving boundaries based on a fixed grid is the level set technique, *Osher and Sethian (1988)*. In the level set formulation and non-dimensionalized by the reference length L, the free stream velocity U_o and the density, ρ, and the viscosity, ν, of water the Navier-Stokes equations may be written as

$$\bar{u}_t = -\bar{u} \cdot \nabla \bar{u} + \frac{\zeta_2 \nabla^2 \bar{u}}{\zeta_1 Re} - \frac{\nabla p}{\zeta_1} - \frac{\nabla x_2}{Fn^2}$$

where $\bar{u}$ is the velocity vector, p is the pressure, subscript t denotes the time derivative, ∇^2 is the Laplacian operator and ∇ is the gradient operator. $Re = U_o L/\nu$ is the Reynolds number and $Fn = U_o/\sqrt{gL}$ is the Froude number. ζ_1 and ζ_2 are density and viscosity functions dependent on the level set function, ϕ.

The level set function is a smooth scalar function defined in the whole domain, including both air and water, and the interface is a subset with a value of zero of this function. Initially, the function is equal to the distance, with sign, from the interface. For later times the value is obtained from the equation

$$\phi_t = -\bar{u} \cdot \nabla \phi$$

This means that the level set function moves with the fluid as an extra quantity. The interface may thus be found from the location where the function is zero. To smooth the jump at the interface the physical properties are smoothed in a band, defined between two values of the level set function, around the zero level set. To keep the band width constant in time the level set function is reinitialized by iterating a Hamilton-Jacobi equation

$$\phi_t = 1 - |\nabla \phi|$$

to steady state. This ensures that the gradient of the level set function is one. Depending on the sign of the level set function the flow properties are given appropriate values

$$\zeta_i = \begin{cases} 1 & \text{if} \quad \phi > \alpha \\ \lambda_i & \text{if} \quad \phi < -\alpha \\ \overline{\zeta}_i + \Delta\zeta_i \sin\left\langle \frac{\pi\phi}{2\alpha} \right\rangle & \text{otherwise} \end{cases} \qquad \text{where} \qquad \begin{aligned} \overline{\zeta}_i &= 0.5\,(1 + \lambda_i) \\ \Delta\zeta_i &= 0.5\,(1 - \lambda_i) \end{aligned}$$

and λ_1 and λ_2 are the ratios between the air and water properties for the density and viscosity respectively. α is half the finite thickness of the band in which the density and viscosity change.

The level set method has the potential to simulate overturning and breaking of waves and even merging without special treatment. Geometrical quantities are not recalculated when the free surface moves like they have to in the moving grid method. It is straightforward and simple to implement the level set method and no complexities are added when it is extended to three dimensions.

Numerical formulation

In the present method the equations of motions, the Navier-Stokes equations, are defined on a staggered grid system. The fluid domain is discretized by a finite-volume formulation and velocity and pressure are updated with a time splitting fractional step method combined with a velocity and pressure simultaneous iteration method. Convective terms and equations for the free surface are discretized with third order upwind schemes.

Turbulence is modelled with the standard k-ε model with wall functions. The turbulence model can not handle the smoothed density and viscosity in the level set formulation near the free surface. So, when the level set method is used the turbulent quantities are solved up to a grid line a few cells under the deepest wave trough where the turbulent viscosity is assumed to be negligible.

One way to apply non-reflecting boundary conditions is to extend the computational domain with an added dissipation zone, *Hino et al. (1993)*. The level set function is damped with an artificial wave damping function, γ, as follows

$$\frac{\partial \phi}{\partial t} = -u_i \cdot \frac{\partial \phi}{\partial x_i} - \gamma(x)\,\phi|_{y=yfs} \qquad \text{where} \qquad \gamma(x) = \begin{cases} A\left(\dfrac{x-x_d}{x_o-x_d}\right)^2 & \text{if } x_d \le x \le x_o \\ 0 & \text{otherwise} \end{cases},$$

A is a constant, x_o is the x-coordinate at the outflow boundary and x_d is defined as $x_d = x_o - 2\pi Fn^2$. Since the initial free surface does not necessarily coincide with a node, the level set function at $y = yfs$, $\phi|_{y=yfs}$ is calculated by linear interpolation. In the moving grid method the kinematic free surface boundary condition is modified with the damping function in a similar manner. This method increases the computational cost undesirably, especially for 3-D computations. Another method is to match the Navier-Stokes equations on the outlet boundary using an anisotropic propagation wave equation, *Jin and Braza (1993)*. A modified version of this, used in the moving grid method is

$$\frac{\partial u_1}{\partial t} + u_1 \frac{\partial u_1}{\partial x_1} - \nu \frac{\partial^2 u_1}{\partial x_2^2} = 0,$$

u_2 is given by the continuity equation whereas pressure and the free surface are linearly extrapolated. Today there is no such method in the level set formulation. For more details on the numerical implementation see *Vogt (1998)*.

Results and discussion

For most cases here the turbulence had no significant effect on the free surface wave profile and was therefore omitted for those cases.

A grid density test for the case of waves generated by a submerged hydrofoil, *Duncan (1983)*, running at Fn=0.567 and non-dimensional depth, d=1.034 is shown in figure 1. The medium grid is hereafter used. Since ship flow calculations mostly concern the water flow only, and due to the fact that the introduction of a band in which the physical properties change is an unphysical approximation, it is favourable to keep the air domain and the band width to a minimum. It is shown here, fig-

ure 2, that for stationary non-breaking waves the band has little influence on the wave profile when the number of cells in the direction normal to the free surface is restricted to a few cells in the band. Further, the air domain only needs to be about 10 cells from the free surface and thus does not affect the computational cost significantly, figure 3. Computations with the moving grid method and the level set technique are compared with experiments in figure 4. With the moving grid method the wave troughs and the first wave are not as well predicted as with the level set technique while both phase and amplitude of the last wave is better predicted with the moving grid method than with the level set technique.

The waves generated by a bottom bump, *Cahouet (1984)*, at Fn=0.43 are compared with computations with the moving grid method and the level set technique in figure 5. To get a stable solution the turbulence model was switched on. The non-reflecting outlet boundary condition was used in the moving grid method and with the level set technique the convective terms were computed with a hybrid scheme with the coefficient of 0.2 i.e. 80% central differences and 20% first order upwind scheme. The dissipation of the waves computed with the level set technique is not visible in the figure but further downstream the waves are damped.

The flow over a bottom mound, *Lee et al. (1989)*, with a sinusoidal shape at Fn=0.9 is shown in figure 6. The upstream advancing solitons, the depressed water level behind the mound and the trailing waves are clearly visible.

Since the density and viscosity are smoothed near the free surface and there is no turbulence model included in the level set formulation, the stresses near the surface cannot be expected to be correct. Nevertheless, it is shown in figure 7 that it is possible to detect the onset of breaking for a submerged hydrofoil running at different depths and Froude numbers. The definition for breaking was taken to be when the normal to the surface was pointing downwards, even though spilling breaking occurs long before that. This was never a problem because a slight change in the depth or Froude number conditions for values near the border line between the breaking and non-breaking regions resulted in an abrupt change of the wave profile.

A breaking wave generated by a submerged hydrofoil at Fn=0.425 and d=0.50 is shown in figure 8. The result is only qualitative since the resolution is insufficient, but it shows that the level set method is capable handling changes in topology.

References

Cahouet J. (1984) "Etude numerique et experimentale du probleme bidmensional de la resistance de vagues non-lineaire", *Ph. D. Theses,* Paris, ENSTA

Duncan J.H. (1983) "The breaking and non-breaking wave resistance of a two-dimensional hydrofoil", *J. Fluid Mech.,* vol 126, 507-520

Hino T., Martinelli L. and Jameson A. (1993) "A finit-volume method with unsructered grid for free surface flow simulations", *Six th int. conf. on num. ship hydrodynamics,* 173-193

Jin G. and Braza M. (1993) "A nonreflecting outlet boundary condition for incompressible unsteady Navier-Stokes calculations", *J. of comp. phys.,* vol 107, 239-253

Lee S.L., Yates G.T. and Wu T.Y. (1989) "Experiments and analysis of upstream advancing solitary waves generated by moving disturbances", *J. Fluid Mech.,* vol 193, 569-593

Osher S. and Sethian J.A. (1988) "Fronts propagating with curvature-dependentspeed: algorthms based on Hamilton-Jacobi formulations", *J. of comp. phys.,* vol 79, 12-49

Vogt M. (1998) "A numerical investigation of the level set method for computing free surface waves" , *Department of Naval Architecture and Ocean Engineering, Chalmers University of Technology, report CHA/NAV/R-98/0054*

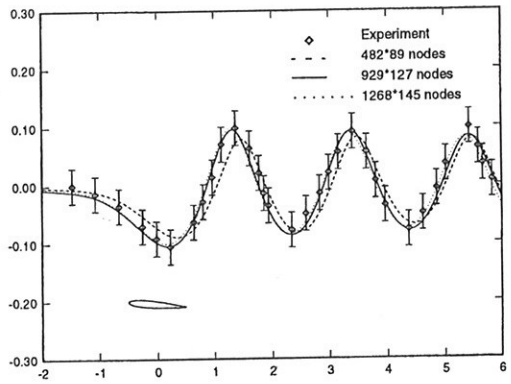

Figure 1 Grid density test.

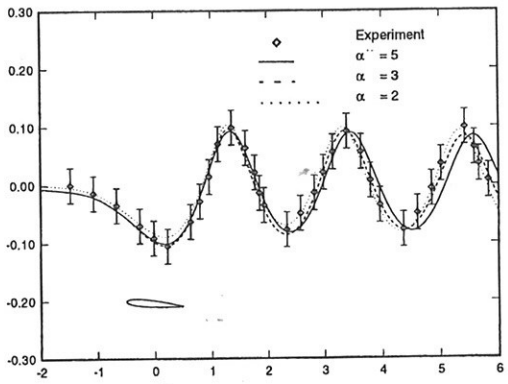

Figure 2 Bandwidth test.

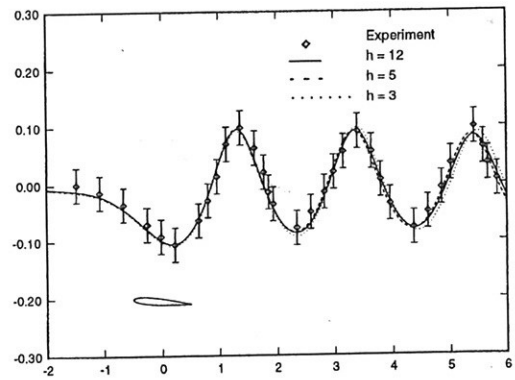

Figure 3 Number of cells above the wave crest.

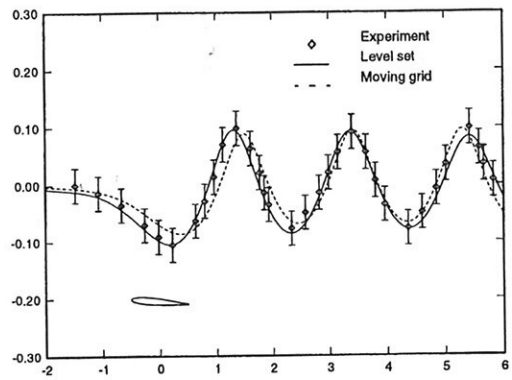

Figure 4 Comparison between numerical methods and experiments, *Fn*=0.567, *d*=1.034.

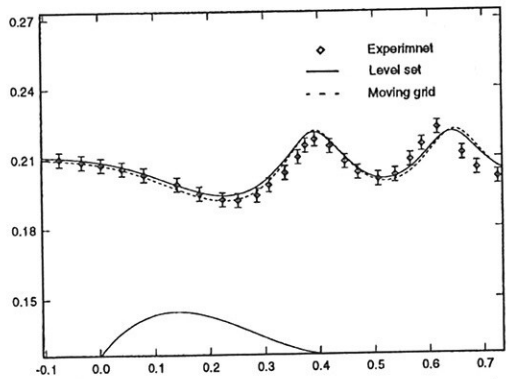

Figure 5 Comparison between numerical methods and experiments, *Fn*=0.43.

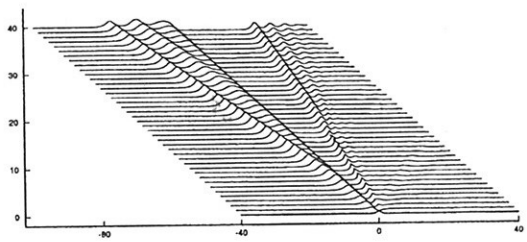

Figure 6 Generation of solitons over a bottom mound, *Fn*=0.9.

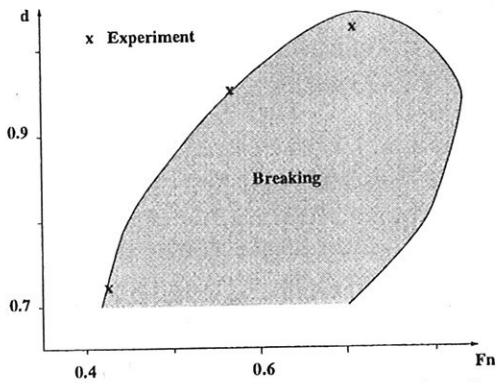

Figure 7 Wave breaking prediction as a function of foil submergence and speed.

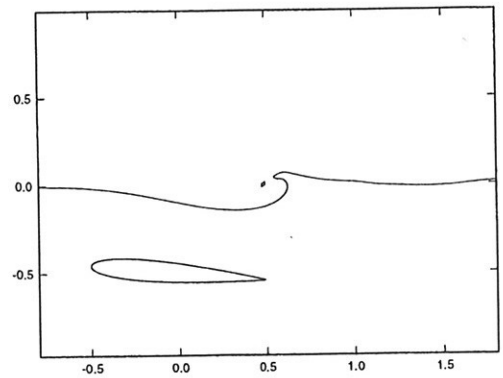

Figure 8 Overturning wave and the break-off of a water drop, *Fn*=0.425, *d*=0.5.

A Rankine Source Method for Wave Resistance Minimization

Hironori YASUKAWA, *Nagasaki Experimental Tank, Mitsubishi Heavy Industries**

1. Introduction

Ship hull forms with minimum wave resistance obtained through a series of iterative calculations by Rankine source method in conjunction with optimization technique (nonlinear programming) have been presented, e.g., by Kim (1989), Janson et al.(1994), Yasukawa (1995) and Mifune et al.(1995). However, computational time is considerable large until obtaining the converged solution since Rankine source method spends much time in evaluating the wave resistance.

This paper proposes a Rankine source method, which is here called Rankine Source Kochin-Function Method (RSKFM), to evaluate the wave resistance with short computational time for the hull form optimization. This method deals with a problem of wave resistance change when slightly modifing the hull form based on the given mother ship. As an application example of the present method, calculation results are introduced with respect to the hull form optimization based on Series 60 (C_b=0.6) hull using the present RSKFM in conjunction with the optimization technique.

2. Wave Resistance for a Modified Hull Form

In the coordinate system, x-axis is defined as direction from the ship stern to the fore, y-axis as lateral direction and z-axis as vertical upward. The $x-y$ plane is defined as a still water surface.

Denoting an original hull form as $F_0(x,y,z) \equiv f_0(x,z) \mp y = 0$, the modified hull form is represented as $F(x,y,z) \equiv F_0(x,y,z) \mp f(x,z) = 0$, where a hull form modification quantity is expressed as $y = \pm f(x,z)$. The f is assumed to be small in quantity. Total velocity potential around the modified hull form $\Phi(x,y,z)$ is represented as:

$$\Phi(x,y,z) = \phi_0(x,y,z) + \phi_1(x,y,z) + \phi(x,y,z) \tag{1}$$

where ϕ_0 means the double-body flow potential for the original form, ϕ_1 the steady wavy flow potential for the original form and a perturbation potential due to the hull form modification ϕ. It is assumed that ϕ is the same order as ϕ_1 and is small in comparison with ϕ_0.

The free-surface condition proposed by Baba (1976) is employed as the free-surface condition. Then, free-surface conditions with respect to ϕ and ϕ_1 are represented as follows:

$$\left(u_0\frac{\partial}{\partial x} + v_0\frac{\partial}{\partial y}\right)^2 \phi_1 + g\frac{\partial \phi_1}{\partial z} = gD(x,y) \qquad \text{on} \quad z=0 \tag{2}$$

$$\left(u_0\frac{\partial}{\partial x} + v_0\frac{\partial}{\partial y}\right)^2 \phi + g\frac{\partial \phi}{\partial z} = 0 \qquad \text{on} \quad z=0 \tag{3}$$

where

$$D(x,y) = \frac{\partial}{\partial x}(\zeta_0(x,y)u_0) + \frac{\partial}{\partial y}(\zeta_0(x,y)v_0), \quad \zeta_0(x,y) = \frac{1}{2g}(U^2 - u_0^2 - v_0^2)$$

U denotes the ship velocity, ζ_0 the wave elevation based on double-body flow, (u_0, v_0) the velocity component of the double-body flow on still water and g the acceleration gravity.

The hull surface condition should be fulfilled on the surface of the modified hull form and is represented as follows:

$$(\nabla\phi_0 + \nabla\phi_1 + \nabla\phi)\cdot\nabla F = 0 \qquad \text{on} \quad y = \pm(f + f_0) \tag{4}$$

*3-48 Bukyo-Machi, Nagasaki 852-8131, JAPAN, email: yasukawa@ngsrdc.mhi.co.jp

Linearizing the equation so as to fulfill the boundary condition on the hull surface of the original form, the following conditions with respect to ϕ_1 and ϕ are obtained:

$$\frac{\partial \phi_1}{\partial n} = 0 \ + \ O(\phi_1^2, \phi_1 f) \qquad \text{on} \ \ y = \pm f_0 \tag{5}$$

$$\frac{\partial \phi}{\partial n} = n_y(\phi_{0x} f_x + \phi_{0z} f_z) \ + \ O(\phi^2, \phi f, \phi\phi_1, f^2) \qquad \text{on} \ \ y = \pm f_0 \tag{6}$$

(n_x, n_y, n_z) demotes outward normal vector of the hull surface. The boundary value problems for the original ship (ϕ_0, ϕ_1) can be solved easily by Rankine source method (Dawson 1977). Therefore, the residual problem is to solve the problem with respect to ϕ. The boundary conditions of ϕ are the same form as those of ϕ_1 except the right hand side, which is the flow perturbation term, of the boundary conditions. Using similar Rankine source method to that for ϕ_1, the problem with respect to ϕ can be solved easily. The position where the present hull boundary condition should be fulfilled is the original ship hull surface. This means that rearrangement of the hull and free-surface panels is not necessary for evaluating the wave resistance against the various hull form modification. This feature is convenience for reduction of computation time of the wave resistance.

In the boundary value problem of this form, the following Kochin-function for evaluating the wave resistance can be defined (Yasukawa 1998):

$$H_T(\theta) = H_1(\theta) + H(\theta) \tag{7}$$

where

$$\begin{aligned} H_1(\theta) = & - \iint_{S_H} \phi_1(x,y,z)\,(n_x i\cos\theta + n_y i\sin\theta + n_z)\,k\,E(\theta;x,y,z)dS \\ & - \frac{U^2}{g}\iint_{S_F} \phi_1(x,y,0)\left[\varphi_x(\varphi_x+2)\cos^2\theta + 2(\varphi_x+1)\varphi_y\cos\theta\sin\theta\right. \\ & \left. +\varphi_y^2\sin^2\theta\right] k^2 E(\theta;x,y,0)dxdy \ - \iint_{S_F} D(x,y)E(\theta;x,y,0)dxdy \end{aligned} \tag{8}$$

$$\begin{aligned} H(\theta) = & \iint_{S_H} n_y(\phi_{0x}f_x + \phi_{0z}f_z)E(\theta;x,y,z)dS \\ & - \iint_{S_H} \phi(x,y,z)\,(n_x i\cos\theta + n_y i\sin\theta + n_z)\,kE(\theta;x,y,z)dS \\ & - \frac{U^2}{g}\iint_{S_F} \phi(x,y,0)\left[\varphi_x(\varphi_x+2)\cos^2\theta + 2(\varphi_x+1)\varphi_y\cos\theta\sin\theta\right. \\ & \left. +\varphi_y^2\sin^2\theta\right] k^2 E(\theta;x,y,0)dxdy \end{aligned} \tag{9}$$

$$E(\theta;x,y,z) = \exp\{ik(x\cos\theta + y\sin\theta) + zk\}, \quad k = \frac{K_0}{\cos^2\theta}, \quad K_0 = \frac{g}{U^2}$$

where S_H means the hull surface and S_F the free-surface(still water surface). φ is perturbation potential of the double-body flow. Then, wave resistance R_w is represented as:

$$R_w = \frac{\rho K_0^2}{2\pi}\int_{-\pi/2}^{\pi/2} |H_T(\theta)|^2 \frac{d\theta}{\cos^3\theta} \tag{10}$$

3. Hull Form Modification Function f

For convenience of the treatment, the modification quantity from the original form $f(x,z)$ is defined as the following simple formula (Suzuki 1998):

$$f(x,z) = f_0(x,z) \times w(x,z) \tag{11}$$

$$w(x,z) = \sum_{i=1}^{M}\sum_{j=1}^{N} A_{ij} \sin\left\{\pi\left(\frac{x_0 - x}{x_0 - t}\right)^{i+2}\right\} \sin\left\{\pi\left(\frac{z_0 - z}{z_0 - \ell}\right)^{j+2}\right\} \tag{12}$$

A_{ij}, x_0, z_0, t and ℓ are parameter for the hull form modification and become the design variables in the optimization procedure. Stem and stern profiles can't be modified for the hull form improvement so far as use of this formula.

4. Minimization of Series 60($C_b = 0.6$) Hull Form

A package routine of the optimization technique with External Penalty Method is employed to treat the design constraints and Hooke-Jeeves' pattern search method is adopted for local search of the solution (Parsons 1954). The solution algorithm in this method is quite simple because the derivatives of the objective function with respect to the design variables are not necessary.

Optimizations are carried out for Series 60 (C_b=0.6) hull. As design constraints, we employ constant displacement volume, constant length perpendicular, constant breadth and constant draft.

Fig.1 shows 2 fore body plans with minimum wave resistance at 0.2 and 0.3 in design F_n where F_n is Froude number based on ship length. In case of $F_n = 0.2$, the optimum form is almost the same as the original form. The original hull form may be close to the optimum hull form in case without protruded bulb in fore hull form. In case of $F_n = 0.3$, the hull form where the sectional area increases near S.S.9 and decreases near S.S.7 1/2 was obtained as the optimum hull form. Fig.2 shows the comparison of sectional area ratio curves. The sectional area curve of so-called high speed type is obtained as the optimum form.

Fig.3 shows the history of wave resistance coefficient based on ship length C_{WL} through the optimization calculation at $F_n = 0.3$. The converged solution is obtained about 350 step. The reduction ratio of the wave resistance is about 11%. This computational time was about 5 hours for work station with 10.50 in SPECfp95.

At the workshop, I should be able to present further applications of this approach to more realistic hull forms.

5. References

Baba, E. (1976): *Wave Resistance of Ships in Low Speed*, Mitsubishi Technical Bulletin No.109, Mitsubishi Heavy Industries, Ltd.

Dawson, C. W. (1977): *A Practical Computer Method for Solving Ship-wave Problems*, 2nd International Conference on Numerical Ship Hydrodynamics, Berkeley.

Janson, C. E., et al.(1994): *Optimization of the Series 60 Hull from a Resistance Point of View*, SRI-CFD Workshop, Ship Research Institute, Tokyo.

Kim, K. J. (1989): *Ship Flow Calculations and Resistance Minimization*, Chalmers Univ. of Technology, Division of Marine Hydrodynamics, Sweden.

Mifune, M., et al.(1995): *An Approach of Hull Form Optimization Oriented to the Wave Resistance*, 6th Int. Symp. on Practical Design of Ships and Mobile Units, Seoul.

Parsons, M. G. (1975): *Optimization Method for Use in Computer Aided Ship Design*, First Ship Technology and Research Symposium.

Suzuki, K. (1998): private communication

Yasukawa, H. (1995): *Minimization of Ship Wave Resistance using Rankine Source Method*, Trans. of the West-Japan Society of Naval Architects, No.89.(in Japanese)

Yasukawa, H. (1998): *A Rankine Source Kochin-Function Method to Remove the Negative Wave Resistance*, Ship Technology Research, Vol.45, No.2, pp.47-53.

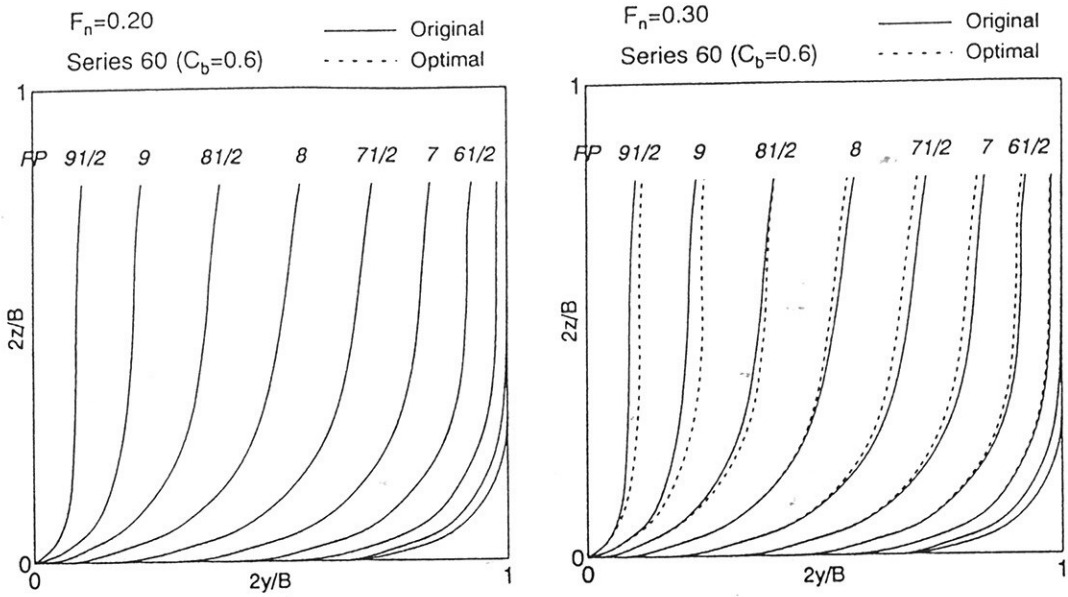

Fig.1: Fore body plans with minimum wave resistance at 0.2 and 0.3 in design F_n

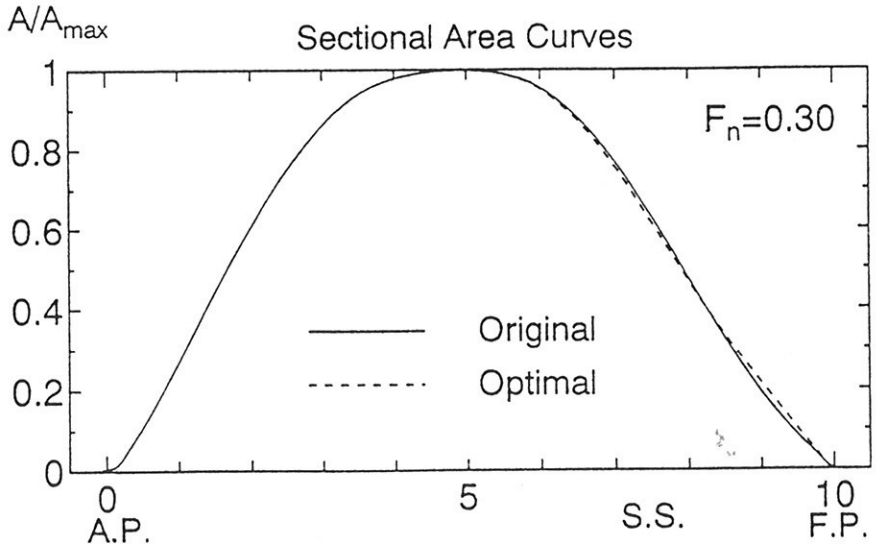

Fig.2: Comparison of sectional area ratio curves

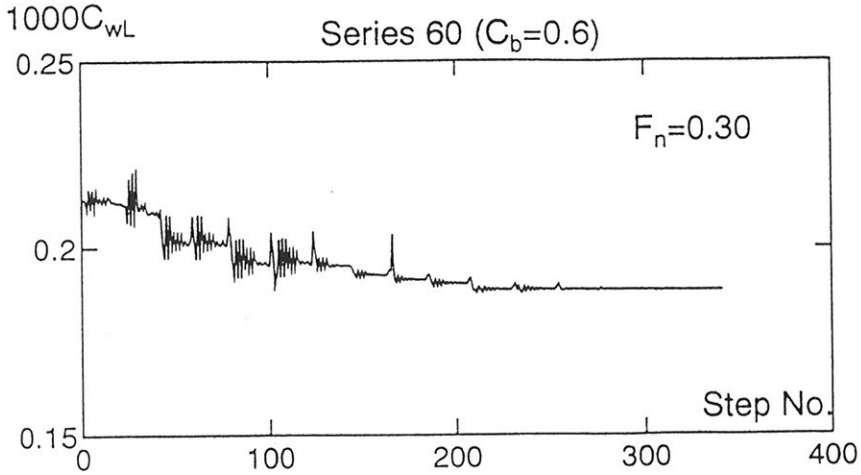

Fig.3: History of wave resistance coefficient through optimization calculation

Nonlinear Wave Resistance Calculations Using a Finite Difference Euler Method

by Daohua Zhang and Allen T. Chwang

ABSTRACT An inviscid flow with a free surface around a Wigley hull is studied numerically. The Euler equations and the continuity equation are solved with fully nonlinear free-surface boundary conditions. A moving grid system is used to fit the deforming free surface at each time step. Time integration is made by a time-splitting fractional-step method while the convection terms are discretized by the QUICK scheme. Computations are performed at six Froude numbers. As a result, calculated hull-side wave profiles and drag coefficients show very good agreement with the experimental data. The entire wave system agrees well with the Kelvin wave pattern.

1. INTRODUCTION

Wave resistance is the largest component of the total resistance of a ship at high speed, and this has attracted a lot of theoretical and experimental research over the years. The nonlinearity of the problem and the associated free-surface boundary conditions make it difficult to predict the free surface flows around a ship accurately and efficiently. With rapid growth in computer capacity, numerical methods are becoming more popular for analyzing flow problems in hydrodynamics and ship design. The methods are split into two main categories: potential-flow and viscous-flow methods. Traditionally, free-surface flow problems have been solved by the potential-flow theory, since in many practical applications the wave pattern and wave resistance are the only information needed. So far, most of popular computer codes in ship design are all potential-flow methods [1]. The modern methods based on Navier-Stokes equations with a free surface are being developed and are just making their way into ship wave problems [2, 3]. The frictional resistance can be obtained by the Navier-Stokes methods at a cost of significant computational resources.

The inviscid flow methods based on the Euler equations have played an important role in aerodynamics, but they never become popular in hydrodynamics. Hino [4] computed a free surface flow around a submerged hydrofoil by both Euler and Navier-Stokes equations, and Farmer *et al.* [1] developed efficient methods to compute Euler and Navier-Stokes solutions for nonlinear ship wave problems. They found that the Euler solution with proper boundary conditions was reasonable in comparison with experiments and other potential calculations. This is encouraging since the Euler method requires significantly less computational resources than the Navier-Stokes method.

Based on the authors' previous two-dimensional Navier-Stokes method with a free surface [5], the objective of the present work is to develop an efficient three-dimensional Euler method for the free surface wave problem. Comparisons of numerical predictions with experimental data for the Wigley hull show encouraging results for wave profiles and resistance coefficients.

2. OUTLINE OF THE COMPUTATIONAL METHOD

A Cartesian coordinate system (x, y, z) is established as the reference frame in the physical domain with the origin fixed at mid-ship on the mean free surface and the x-, y-, and z-axes in the aft direction, towards the starboard, and upwards respectively. The unsteady Euler and continuity equations with a free surface are solved for the mean-velocity components (u, v, w) and the piezometric pressure $\phi = p + z/F_n^2$, where $F_n = u_0/\sqrt{gL}$ is the Froude number, u_0 the free stream velocity, L the ship length and g the gravitational constant. The governing equations in conservative form for (u, v, w) and ϕ are partially transformed into numerically generated boundary-fitted, non-orthogonal, curvilinear coordinate system (ξ, η, ζ). Variables

are non-dimensionlized using the ship length L, free stream velocity u_0 and density ρ. The transformed equations are solved using a regular grid and the finite difference discretization. Spatial differentials are discretized using the second-order central differences and the QUICK scheme is used for convection terms. Although the present solutions are for steady flows, the equations are solved in unsteady form with time serving as a convergence parameter. Time marching is carried out using a time splitting fractional step. A Poisson equation for the pressure increment between two time steps is solved to enforce the mass conservation at each time step.

One of the difficulties in solving free-surface flow problems is that the location of the free surface is not know *a priori* and is part of the solution in the problem. On the instantaneous free surface, both the kinematic and dynamic conditions must be satisfied. The kinematic condition, implemented by the Euler method, is used to determine the free surface location and the dynamic condition is to impose atmospheric pressure on the free surface. The grid system is regenerated at each time step to fit with the new location of the free surface.

The impermeability condition is applied on the hull surface. On the symmetry plane ($y = 0$), derivatives in the y direction as well as the v component of velocity are set to zero. At the far upstream, flow is uniform and free surface is undisturbed. The downstream plane is taken sufficiently far from the ship and a dissipation zone with coarse grid is added there to prevent the reflection of waves into the solution domain. Detailed equations and the solution procedure were given by Zhang & Chwang [5].

3. RESULTS AND DISCUSSION

Calculations are made on a Wigley hull with fixed sink and trim. The calculation domain is taken as x (-1.0, 3.0), y (0.0, 1.0), and z (h, -0.7). An H-type mesh of 181x40x35 grid points with 95x19 on the hull is used to perform simulations at six Froude numbers. The time step is set to be Δt=0.001.

The computed wave profiles along the hull, compared with experimental data of the University of Tokyo are shown in Fig. 1. The agreement with the experiment is very good on the whole. Some discrepancies are noted near the stern for smaller Froude numbers, where separation and eddy losses may be present in the experiments. Bow waves are under-predicted and phase lagged. The whole wave systems are also in excellent agreement with the well known Kelvin ship wave pattern (Fig. 2).

In fact, most solutions presented at the CFD Workshop Tokyo 1994 showed an under-prediction of the bow wave in comparison with data due to the inability of the numerical methods to simulate a thin film (about 1.5 mm) and beads of fluid present near the bow region. It was also observed at the workshop that most of the wave patterns showed rather poor results in spite of the good prediction of hull-side wave profiles. Strangely enough, the pressure drag is rather well calculated although the wave patterns are not acceptable [3].

The wave resistance is obtained easily by integrating hull surface pressure in the present calculation (Fig. 3). Fig. 4 shows a comparison between the computed and experimentally determined resistance coefficients, both derived from integrating the hull surface pressure. The computed resistance coefficient shows a favorable agreement with the experimentally determined value.

Many attempts to evaluate wave resistance at medium and high speeds are found in the literature and most of them show a reasonable correspondence between measurements and calculations. However, the interpretations of the results are not obvious. In fact, the actual wave resistance is rarely measured but derived from the experiments, including some form-factor effect of viscous resistance. In the present study, although both computed and experimentally determined coefficients shown in Fig. 4 are derived by the same way, they are different in the physical sense. The computed resistance by the Euler method under the assumption of an inviscid fluid is the wave-making resistance, while the experimentally determined one consists of wave-making resistance and viscous pressure drag because the

surface pressure measured in the experiments is under the effect of viscosity. For a thin and streamlined body like a Wigley hull, the viscous pressure drag is usually very small compared with the wave-making resistance at medium and high speeds. Therefore, the computed wave drag over-predicts the experimentally determined drag by a small amount. This can be seen clearly in Fig. 5 where the resistance coefficient versus the Froude number is presented. It is also seen from this figure that the experimental data show some oscillation with Froude number due to the interaction between the bow and stern wave systems, while the numerical predicted resistance curve does not have humps and hollows distinctly as the experimental data do and it also mismatches the phase with the experimental data. However, the resistance computed by the present method seems quite promising compared with the results presented at the CFD Workshop Tokyo 1994, which presented the state of the art of CFD in ship hydrodynamics. At present, the capability of predicting the wave resistance numerically is not fully validated even for ranking purposes. Therefore, the predicted wave resistance should not be used for absolute power predictions.

ACKNOWLEDGMENTS This research was jointly sponsored by the Hong Kong Research Grants Council under Grant No. HKU 304/95E and by the University of Hong Kong under CRCG Grant Nos. 337/064/0025 and 337/064/0032.

REFERENCES

[1] Larsson, L. (1996), "CFD in Ship Design-Prospects and Limitations," The 18th Georg Weinblum Memorial Lecture.

[2] Patel, V.C. and Stern, F. (1993), Proc. 6th Int. Conf. Numer. Ship Hyd., Iowa City, USA.

[3] Mori, K. (1994), Proceedings of CFD Workshop Tokyo 1994, Tokyo, Japan.

[4] Hino, T. (1988), "Numerical Computation of a Free Surface Flow around a Submerged Hydrofoil by the Euler/Navier-Stokes Equations," The Autumn Meeting of the Society of Naval Architects of Japan, 9-17.

[5] Zhang, D.H. and Chwang, A.T. (1996), "Numerical study of nonlinear shallow water waves produced by a submerged moving disturbance in viscous flow," Phys. Fluids 8 (1), 147-155.

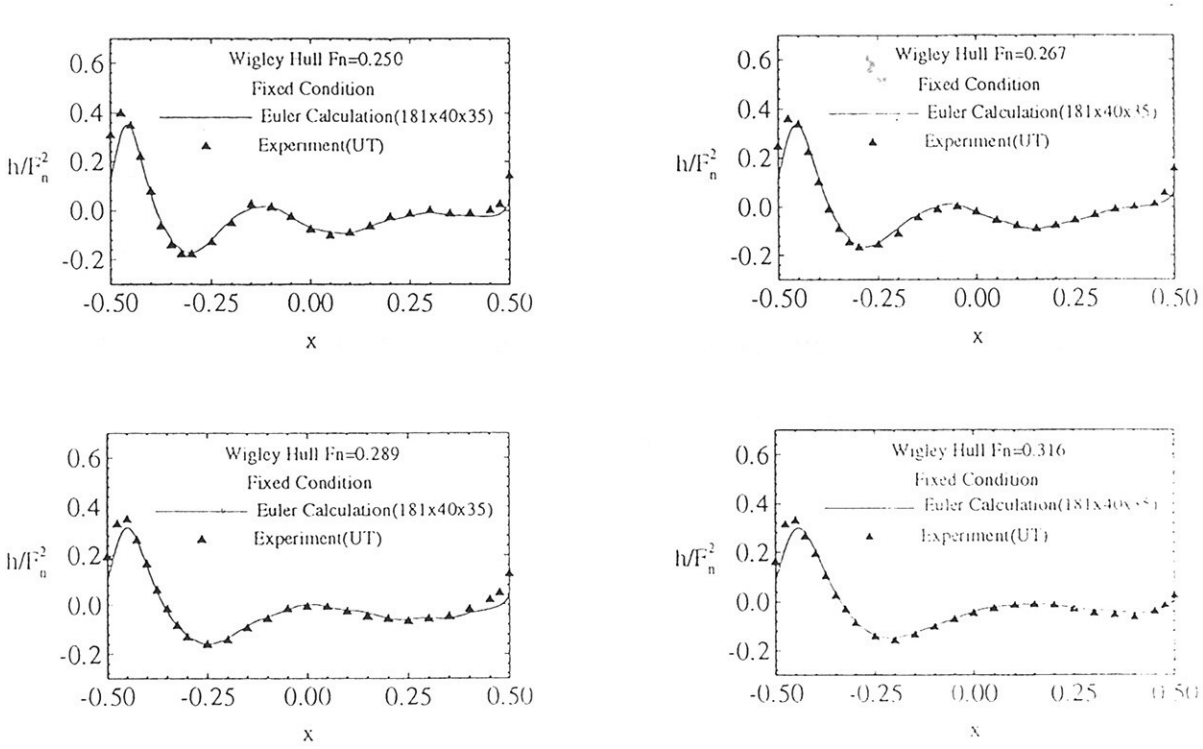

Figure 1. Wave profiles along the hull-side.

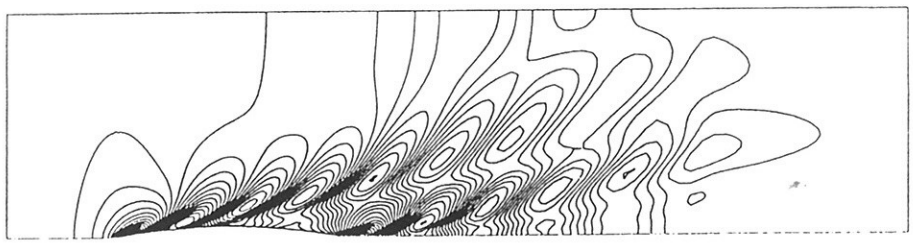

Figure 2. Overhead view of wave elevation (or pressure) contours for F_n=0.289.

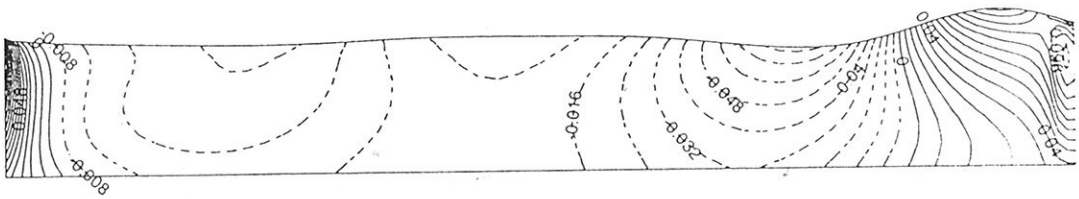

Figure 3. Pressure distribution on the hull surface for F_n=0.289.

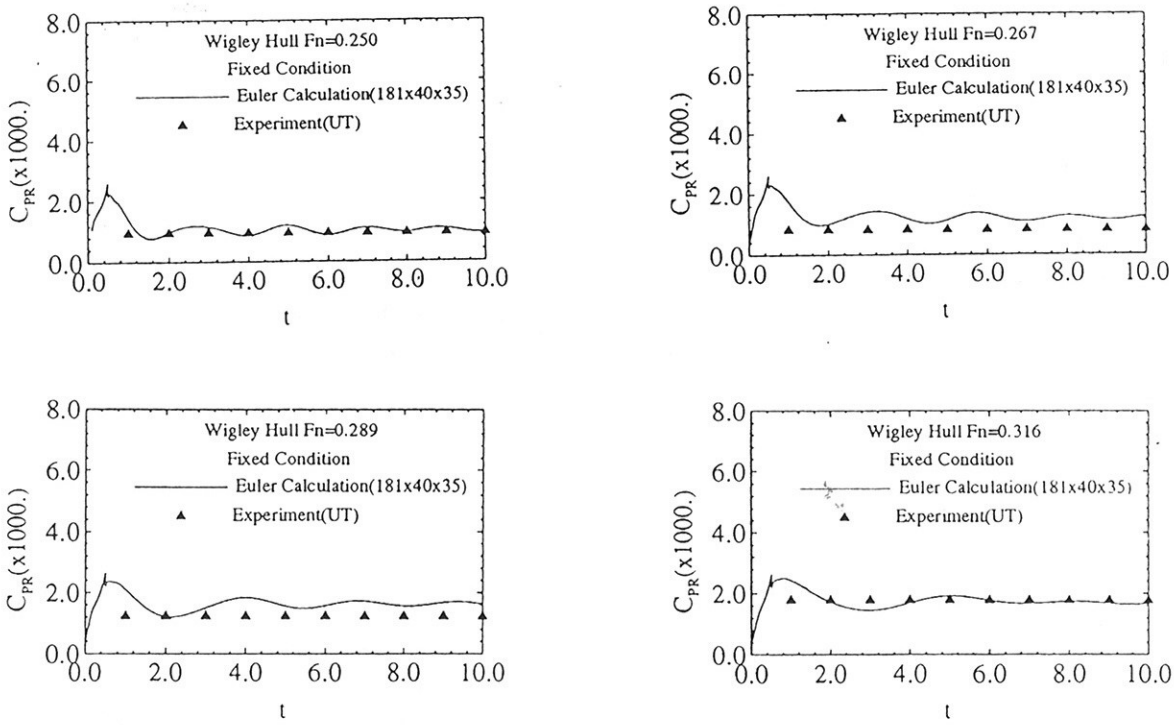

Figure 4. Resistance coefficient derived from integrating the hull surface pressure.

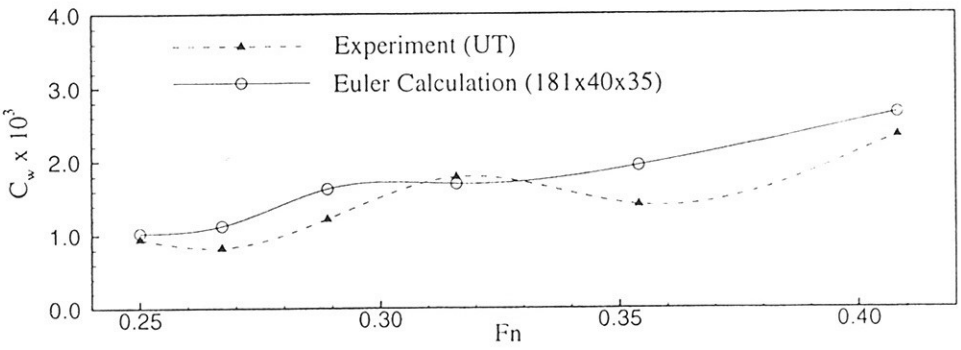

Figure 5. Pressure resistance coefficient versus the Froude number.

Call for Papers

2nd NUMERICAL TOWING TANK SYMPOSIUM (NuTTS'99)

2-4 August 1999

INSEAN, Rome, Italy

Dear Colleague,

You are invited to participate in the above event, to be held at INSEAN in Rome on 2-4 August 1999. The objective of the event is to provide a forum for informal discussions among experts in the field and to disseminate latest results. In addition to established experts in the field, younger workers and Ph.D. students are especially encouraged to participate. We also would like to encourage female colleagues to take an active role in the symposium.

The abstracts of the proposed talk will be directly reproduced in the proceedings. The first page should be headed with the title and authors' names in a compact form to economise on space. A list of authors and addresses will included in the proceedings by the host. Extended abstracts should be limited to 4 pages in a field 17cm by 25cm per page. Copies of the extended abstract should be sent in good quality (fax is not acceptable) to the host and a copy (fax acceptable) to the organizer.

The technical program will be based upon concise talks which should be similar in style to seminars and colloquia, except that background information well known by specialists in the same field should be omitted. Work in progress, even if at the time of submission still incomplete, is very welcome and problems encountered may be addressed. The event will be held in a modern lecture hall and transport in the morning and afternoon will be provided to a hotel where all participants stay and have meals together to maximize interaction and discussion between participants.

Prospective participants should fill in the attached form and return it to the organizer. An early reply will help us in organising the event better. For the early feedback, a tentative title or topic will suffice.

Please pass this call for paper on to colleagues who should be interested or inform us of their address and email address, so that we can inform them directly.

Yours sincerely

Maurizio Landrini (host)
INSEAN
Via di Vallerano 139
I-00128 Roma
Italy
fax: +39-6-5070619
tel: +39-6-50299274
m.landrini@mail.insean.it

Volker Bertram (organizer)
TUHH
Lämmersieth 90
D-22305 Hamburg
Germany
fax: +49-40-29843199
tel: +49-40-29843171
bertram@ifspc228.schiffbau.uni-hamburg.de

Topics:
- Nonlinear flows around marine structures
  (Navier-Stokes, RANSE, Euler with or without free surface)
- Free-surface flows around marine structures
  (3-d seakeeping with forward speed, nonlinear wave resistance, etc)
- Related topics
  (validation experiments, numerical techniques, etc)

Registration fee: 600,000 Lira per person, 400,000 Lira for students
The registration fee includes accomodation, food (3 meals/day) and conference proceedings

The accomodation will be single room with private bath for the regular fee, double room with private bath for the reduced fee for students.

Deadlines:

Early feedback:	30 April 1999
Abstracts received:	30 May 1999
Notification of acceptance:	7 June 1999

Deadlines will be strictly enforced!

Please return this reply card by 30 April 1999, but latest by 30 May 1999

EARLY FEEDBACK FORM NuTTS'99

I intend to attend the event (y/n) ...

I will present a paper (y/n) ...

Title/Topic of paper:

Author(s):

Affiliation:

Address:

Tel:

Fax:

email: